Mechanical and structural studies of internal lipid-containing bacteriophage PRD1

by Stavros Azinas

Bilbao, 2018

Universidad del País Vasco
Euskal Herriko Unibertsitatea

Thesis supervisors:

Dr. Nicola G.A. Abrescia & Dr. Ralf P. Richter

Structural Virology Lab, Bilbao

CIC bioGUNE
Biozientzietako Ikerkuntza Kooperatiboko Zentroa
Centro de Investigación Cooperativa en Biociencias

Biosurfaces, San Sebastian

CIC biomaGUNE
Biomaterialetako Ikerkuntza Kooperatiboko Zentroa
Centro de Investigación Cooperativa en Biomateriales

PHD DEGREE CERTIFICATE

DOCTORAL THESIS VIVA CERTIFICATE

PhD STUDENT MR/MS. _____

TITLE OF THE THESIS: _____

_____

_____

After having witnessed the completion of the viva by the author and their response to any objections and/or suggestions made, the Panel appointed by the Postgraduate Commission of the University of the Basque Country to examine the Doctoral Thesis indicated above, meeting on the indicated date, agreed _____ to award the following grade:
unanimously or by majority vote

DISTINCTION / MERIT / PASS / FAIL

Viva language(s) (in the event of there being more than one language, please specify the percentage of the thesis defended in each):

Spanish _____

Basque _____

Others (specify which and the corresponding percentage) _____

In _____on _____of _____, _____

CHAIRPERSON, SECRETARY,

Signed: Signed:

Dr. _____ Dr: _____

MEMBER 1, MEMBER 2, MEMBER 3,

Signed: Signed: Signed:

Dr. _____Dr._____Dr._____

PHD STUDENT

Signed_____

ACKNOWLEDGEMENTS

This thesis is dedicated *entirely* to my parents. I know that you regretted the distance which has separated us for so long, but you have endured and supported me for these many years. I'm sorry for not being there for you during your hard times.

While writing the thesis itself is a difficult feat on its own, acknowledging and expressing gratitude to all the people that have been part of my doctoral life is itself a very complicated matter. Primarily, I would like to thank both of my supervisors, Ralf and Nicola, for giving me the opportunity to work on this project. During the last 4 and a half years, they have not only helped me become a more independent researcher, but also a stronger person. Initially at Ralf's group, where he introduced me into the world of AFM, and using his passion and diligence at work, but also his patience and guidance, has helped me appreciate and understand how the manipulation of miniature changes could lead to a stable and consistent result. Following that, Nicola's meticulousness, and detailed methodology, helped me understand and visualize these changes from a structural standpoint, and allowed me to combine the two parts into a unique expertise.

The friends and colleagues that have been part of the first ~2.5 years in Donosti, will always be part of my memories. Leo, Nikos, Eleutheria, Maria, Carolina, Leire, Angel, Luismi, Etxebe, Richard, and many more that we have passed so much time during work, but also during those pintxo-pote in Gros, the txuletas at the sidreria, and the (Ralf-inspired) occasional tequilas with orange. An important mention here is of course Fouzia, friend, post-doc and co-director of the first part of the project. Her experience and patience, but also her colourful and friendly character helped me become an experienced AFM user. I wish you all the best for your future and hope our paths coincide again!

As hard it was leaving San Sebastian, transitioning to Nicola's lab in Bilbao was made much easier by finding a solid, friendly, and accepting group there. Isaac, Diego, Hani, thank you for all the support and familiarizing me in the wonderful world of structural biology. For all the

times during lunch and my “enormous” lunch-boxes, I’d also like to thank Miguel, Melissa, Jorge, Rebecca, Idoia, and all the people at the 800 building. A special mention goes to my friends, housemates, and colleagues, Ilaria and Laura! Thanks for sustaining my moods, and being an important step and support in my life.

Asier, Iñaki, Jon, y Giovanni, gracias por ser un importante parte de mi vida aquí en Bilbao.

Finally, the support of my closest Friends, even from far, has always being a crucial part of my life. Without them, and their restless ears, it would have been very difficult to accomplish so much. Γιάννη, Κατερίνα, Στέλιο, Πέτρο, Δέσπω, Μαρίσια, Φωτεινή, Νεόφυτε, Μαρία: Ευχαριστώ για όλα όσα έχετε κάνει για μένα κ πάντα θα εκτιμώ όλες τις στιγμές που περάσαμε μαζί (κ χώρια π λαλεί κ ο Καρράς :).

“I see now that the circumstances of one's birth are irrelevant. It is what you do with the gift of life that determines who you are.”

— **Takeshi Shudo**

RESUMEN

La protección del genoma viral durante el viaje extracelular es un requisito absoluto para la supervivencia y replicación del virus. Una vez que la partícula viral se une a la célula huésped, puede comenzar la eyección del material genómico. Además de las cápsides proteicas casi universales, ciertos virus poseen una capa de membrana que encierra su genoma de ADN bicatenario (ds) dentro de la cubierta proteica. Aunque las propiedades mecánicas de otros virus se han estudiado anteriormente, esta tesis investiga un virus con una membrana bajo su cápside proteica. Usando el virus enterobacterial PRD1 como prototipo de virus sin cola que contienen membrana, y una combinación de ensayos de nanoindentación mediante la microscopía de fuerza atómica y modelado de elementos finitos, mostramos que la arquitectura jerárquica de PRD1 (cubierta de proteína, vesícula proteolipidica, ds ADN) proporciona una mayor estabilidad contra el estrés mecánico que la lograda por otros virus icosaédricos ds ADN que carecen de una membrana. La combinación de un caparazón proteínico rígido y quebradizo junto con una vesícula de membrana blanda y dócil produce un nanomaterial compuesto resistente adecuado para proteger el ADN viral durante el transporte extracelular. Además, observamos la estructura y las propiedades mecánicas que implican el ensamblaje del tubo de eyección de ADN de dicho virus. Si bien los estudios han resuelto la estructura de varios virus en tubos, aquí investigamos un fago que forma el tubo de eyección de ADN al unirse. Empleamos la reconstrucción con crio-microscopía electrónica (cryo-EM) para mostrar que esta partícula viral está produciendo un tubo estructurado, no helicoidal, con una simetría axial de siete veces, que se forma utilizando la membrana proteolípica. En combinación con ensayos de nanoindentación de microscopía de fuerza atómica (AFM), visualizamos partículas individuales que producen tubos y mostramos que el tubo de PRD1 tiene una rigidez comparable a estructuras tubulares similares, como túbulos lipídicos gruesos o virus del mosaico del tabaco (TMV). Hay sugerencias sobre la capacidad del tubo de autocurarse, cuando se libera presión mecánica externa después de la compresión más allá del punto de

fluencia. Estos resultados proporcionan la primera comprensión de la relación entre la estructura, las propiedades mecánicas y la función de los virus que contienen membrana. Podrían beneficiar a los nanoingenieros que podrían incorporar el diseño compuesto de PRD1 en su búsqueda de nanopartículas más estables, pero también la búsqueda de nuevas soluciones farmacéuticas que se ocupen de la resistencia antibacteriana y las infecciones bacterianas en general, ya que este nanotubo proteolipídico puede perforar agujeros en la pared celular bacteriana.

El trabajo presentado en esta tesis implica el bacteriófago sin tubo PRD1, un virus con una membrana lipídica debajo de su capa proteica. Aquí se abordan cuestiones relacionadas con la estabilidad mecánica de la partícula, junto con las contribuciones de cada uno de sus componentes arquitectónicos. También arrojamos luz sobre el ensamblaje, la estructura y las características del tubo de eyección de ADN proteolipídico; esta información sin precedentes podría proporcionar nuevas estrategias sobre el diseño de nuevos antimicrobianos y nanopartículas.

Esta tesis tiene los siguientes objetivos generales:

• La investigación mecánica mediante microscopía de fuerza atómica (AFM) del bacteriófago PRD1 que contiene lípidos mediante el análisis de cada componente arquitectónico utilizando partículas derivadas de PRD1.

• La investigación mecánica y estructural del tubo de eyección de ADN de PRD1, utilizado para la infección de células bacterianas, mediante microscopía crioelectrónica (cryo-EM) y AFM.

La tesis se estructura de la siguiente manera:

El Capítulo 1 es el capítulo introductorio y cubre una descripción general de virus y bacteriófagos, con un enfoque específico en PRD1; así como una descripción general de las dos principales técnicas utilizadas durante el lapso de la tesis: AFM y cryo-EM.

El Capítulo 2 cubre los objetivos de este estudio.

El Capítulo 3 describe la investigación nanomecánica de los componentes arquitectónicos individuales de PRD1, y dilucida cómo estos contribuyen a la rigidez y la estabilidad mecánica del virión PRD1.

El Capítulo 4 estudia la investigación estructural y nanomecánica del tubo de eyección de la cola de PRD1. El Capítulo 5 es el capítulo final que fusiona las principales conclusiones de cada capítulo y brinda una breve perspectiva de lo que esta investigación puede proporcionar a los futuros investigadores.

El Capítulo 6 contiene la bibliografía para la tesis completa.

El apéndice tiene una lista de todas las abreviaturas presentes en este trabajo, así como una colección de artículos publicados del trabajo que se han realizado en los últimos 4 años.

CONCLUSIONES

• Los virus se pueden ver como entidades biológicas compuestas donde los ácidos nucleicos, las proteínas y los lípidos se ensamblan para producir partículas funcionales para la infección. Esta tesis ha proporcionado una primera comprensión de las propiedades nanomecánicas de los virus con una membrana interna. Se puede esperar que se convierta en una referencia para el trabajo futuro con esta clase de virus.

• Las propiedades nanomecánicas de PRD1 muestran que el genoma presurizado proporciona rigidez, pero no mejora la estabilidad, ya que los mutantes sin genoma ceden bajo la misma fuerza, incluso si son menos rígidos.

• Las cápsidas de proteínas Penton-less rinden 3 veces antes que los mutantes libres de genoma, pero que contienen vesículas.

• La vesícula proteolípica es de un orden de magnitud menos rígida que cualquier partícula PRD1 investigada, pero se comporta de manera similar a otras vesículas lipídicas.

• Proponemos que, como en un material sándwich compuesto, una matriz proteínica / polipéptido interfacial en PRD1 genera una conexión estrecha que acopla mecánicamente la cápside y la membrana. Será interesante ver si el principio de diseño de mejorar la estabilidad

mecánica mediante la formación de una doble capa compuesta de cápside-membrana es exclusivo de PRD1 o generalmente empleado para esta clase de virus.

• El tubo de eyección de ADN de PRD1 está compuesto de material proteolípido. La polimerización de la proteína formadora de tubos conduce a una serie de discos apilados, cada uno compuesto de siete subunidades, y que tiene una simetría de siete veces, pero no una helicoidal.

• Estudios previos de mutación del fago PRD1, junto con nuestros resultados actuales, sugieren que la proteína transmembrana P32 es la proteína polimerizante.

• Este enriquecimiento de proteínas durante la remodelación de la membrana conduce a una bicapa de lípidos más delgada y colapsada durante la polimerización del tubo.

• Las características nanomecánicas del tubo, además de la presencia de una estructura definida, insinúan la presencia de material proteico, ya que exhibe un carácter más rígido en comparación con la vesícula lipídica sola.

PERSPECTIVAS

Cuando respondimos algunas preguntas sobre la estructura mecánica y el ensamblaje de la cápside y el tubo de PRD1, también surgen preguntas adicionales.

1. Se debe realizar un trabajo final sobre la estructura del tubo.

2. Queda por validar si otros virus que contienen membrana muestran un comportamiento similar al que muestra PRD1. Esto podría generalizar nuestro modelo propuesto de que la arquitectura multicapa proporciona una mayor estabilidad de partículas.

3. La investigación de mutante P32, que producen tubos más cortos proporcionaría una mayor comprensión en el montaje del nanotubo.

En una perspectiva amplia, nuestros resultados pueden ayudar a los nanoingenieros en su búsqueda de nanopartículas más estables, ya que la naturaleza compuesta de PRD1 puede ser una inspiración para el diseño de nanopartículas. Además, la búsqueda de nuevos antimicrobianos podría ser asistida por el uso de máquinas de nanodrilling, como el tubo de eyección del bacteriófago PRD1.

ABSTRACT

Protection of the viral genome during extracellular travel is an absolute requirement for virus survival and replication. Once the viral particle attaches to the host cell, the ejection of the genomic material can begin. In addition to the almost universal proteinaceous capsids, certain viruses possess a membrane layer that encloses their double-stranded (ds) DNA genome within the protein shell. While the mechanical properties of other viruses have been studied before, this thesis investigates a virus with a membrane under its protein capsid. Using enterobacterial virus PRD1 as a prototype of tail-less, membrane-containing viruses, and a combination of nanoindentation assays by atomic force microscopy and finite element modelling we show that the hierarchical architecture of PRD1 (protein shell, proteo-lipidic vesicle, dsDNA) provides greater stability against mechanical stress than achieved by other dsDNA icosahedral viruses that lack a membrane. The combination of a stiff and brittle proteinaceous shell coupled with a soft and compliant membrane vesicle yields a tough composite nanomaterial well-suited to protect the viral DNA during extracellular transport. Furthermore, we look at the structure and mechanical properties involving the assembly of the DNA ejection tube of such a virus. While studies have solved the structure of various tailed viruses, here we investigate a phage that forms the DNA ejection tube upon attachment. We employed cryo electron microscopy (cryo-EM) reconstruction to show that this viral particle is producing a structured, non-helical tube, with a seven-fold axial symmetry, that is formed using the proteo-lipidic membrane. In combination with atomic force microscopy (AFM) nanoindentation assays, we visualize individual tube producing particles, and showed that the PRD1's tube has a stiffness comparable to similar tubular structures, such as thick lipid tubules, or tubular-shaped tobacco mosaic virus (TMV). Hints regarding the tube's ability to self-heal are present, when external mechanical pressure is released after compression beyond the yield point. These results provide the first insight into the relationship between structure, mechanical properties and function of membrane-containing viruses. They could benefit nanoengineers that could incorporate the

composite design of PRD1 in their quest for more stable nanoparticles, but also the quest for novel pharmaceutical solutions that deal with anti-bacterial resistance, and bacterial infections in general, as this proteo-lipidic nanotube can drill holes into the bacterial envelope.

TABLE OF CONTENTS

AIMS AND OUTLINE OF THE THESIS

The work presented in this thesis involves tail-less bacteriophage PRD1, a virus with a lipid membrane under its proteinaceous shell. Questions regarding the mechanical stability of the particle, along with the contributions of each of its architectural constituents are being addressed here. We also shed light on the assembly, structure, and characteristics of the proteo-lipidic DNA ejection tube; this unprecedented information could provide new strategies insights into the design of new antimicrobials, and nanoparticles.

This thesis has the following ***general aims*** and *i*s structured as follows:

- The mechanical investigation via atomic force microscopy (AFM) of lipid-containing bacteriophage PRD1 by analysis of each architectural component using PRD1-derived particles.
- The mechanical and structural investigation of PRD1's DNA ejection tube, used for bacterial cell infection, by cryo-electron microscopy (cryo-EM) and AFM.

Chapter 1 is the introductory chapter and covers a general overview of viruses and bacteriophages, with a specific focus on PRD1; as well as an overview on the two major techniques used during the span of the thesis: AFM and cryo-EM.

Chapter 2 covers the objectives of this study.

Chapter 3 describes the nanomechanical investigation of the individual architectural constituents of PRD1, and elucidates how these contribute to the stiffness and mechanical stability of the PRD1 virion.

Chapter 4 studies the structural and nanomechanical investigation of PRD1's ejection tail tube.

Chapter 5 is the concluding chapter which merges the main conclusions from each chapter and provides brief perspectives on what this investigation can provide to future researchers.

Chapter 6 contains the bibliography for the full thesis.

Appendix has a list of all abbreviations present in this work, as well a collection of published articles from work that has been performed that past 4 years.

Chapter 1: Introduction

1. INTRODUCTION

1.1. VIRUSES

Viruses are found infecting all living organisms, ranging from bacteria, yeast, plants to animals. The life cycle of a virus is relatively simple: the only mission in its life is to replicate itself. Viruses cannot do this on their own, as compared to organisms; they need the aid of the host-cells. Viruses use different strategies to shuttle their genome into the cell, where thousands of copies are synthesized for the new virus progeny that finally leave the host cell ready to infect other cells. The infection usually leads to an inflammatory response by the host-cell with consequent infection signs, and possibly to cell apoptosis.

Viruses are also masterpieces of nano-bioengineering. They use their shells (a protein capsid, or a lipid envelope fenestrated by glycoproteins in the case of enveloped viruses) to protect the genome from being damaged during their extracellular travel. For some viruses, their proteinaceous capsids reveal minimalistic and highly symmetric architecture. Icosahedral particles with a 5-, 3-, and 2-fold rotational symmetry allow placement of 60 identical units with equivalent contacts between them. Despite this simplicity, this design allows for genome protection, viral infection and replication. The shell must fulfil “contradictory” roles: it shall be strong and flexible enough against internal and/or external pressure, mechanical deformation and certain environmental changes, such as temperature and pH. As an example of the mechanical strain the capsid suffers, the internal genome pressure of bacteriophages and many other double-stranded (ds) DNA viruses reaches tens of atmospheres: so that their genome can be ejected into the cell after attaching to the cell surface; yet the pressure has to be sustained by the shells before infection (Ivanovska et al., 2004, Santos-Perez et al., 2017). These properties, as well as their bio-compatible nature, render these structures efficient nano-containers for potential biomedical uses.

In addition to the structural studies, which reveal the molecular organization of viruses, nanomechanical studies of viruses have recently gained much attention. Such mechanical

studies can clarify the organization of the viral shells and how the molecular structure relates to mechanical properties, their responses to environmental changes (pH, temperature, osmotic effects), and the correlation between the viral mechanics and viral functions in their life cycle. Viruses during their evolution, have developed different techniques for efficiently delivering their genomic material in the infected cell. The most studied and best described systems are those devised by the tailed dsDNA bacteriophages, which generally package their genome at very high densities within a rigid proteinaceous capsid shell. The elastic, electrostatic, entropic, osmotic, and hydration energetic costs incurred by constraining the dsDNA at very high densities within the fixed volume of these phage capsids generate a significant internal pressure (Kindt et al., 2001, Ghosal, 2012, Purohit et al., 2005, Panja and Molineux, 2010, Evilevitch et al., 2003, Gelbart and Knobler, 2009). This pressure is thought to provide the initial force driving genome ejection into the cell, while DNA-binding proteins, DNA condensation or enzymes may help during the final stages of the transfer (Molineux, 2001, Jeembaeva et al., 2010, Inamdar et al., 2006, Purohit et al., 2005, Zandi et al., 2003).

A common trait for all tailed dsDNA phages, e.g. *Myoviridae*, *Podoviridae*, and *Siphoviridae*, is that their proteinaceous DNA injecting machineries are always assembled or completed prior to the time of infection. Likewise, for this group the DNA exits the capsid through the tail. For members of the *Myoviridae* family, energy stored in the conformation of the proteins of their long contractile phage tails, is critical for the penetration of the outer membrane and the peptidoglycan cell wall, and thus to reach the inner cell membrane (Leiman et al., 2004). For bacteriophages with non-contractile tails, neither the short (*Podoviridae* family, Figure 1.1A, left) nor the long non-contractile tail (*Siphoviridae* family, Figure 1.1A, right) are known to provide energy for the infection process.

In contrast to the wealth of experimental and theoretical information that has been acquired about the genome entry of tailed dsDNA bacteriophages (Figure 1.1A), very little is known

about this process for viruses with an internal membrane vesicle such as bacteriophage PRD1 (Figure 1.1B).

Investigating the structural and material properties of proteins, complexes, and viruses, via different methodologies, we can explain the correlation between the molecular structure and its biological function. As such, structural virology can provide high-resolution molecular structures (Rossmann, 2013): capsid-protein arrangements such as inter-subunit and intra-subunit organization, as well as genome–capsid interactions that are established during or after the assembly process are revealed. Meanwhile, multidisciplinary studies via mechanical virology, can quantify capsid mechanical and material properties and investigate their relation to structural changes and the virus self-assembly process (Roos et al., 2010, Mateu, 2012).

These two physical virology branches, together with biological, biochemical and chemical approaches, create a deeper understanding of how viral proteins and capsomers self-assemble into highly ordered shells, and how conformational changes inside the capsid relate to genome packaging or release (Mateu, 2012). These key insights not only elucidate the biology of viruses pivotal for harnessing viral pathologies, but also allow to manipulate viruses and to create virus-like particles with numerous applications in nanomedicine and nanotechnology (Singh et al., 2006, Wen et al., 2013).

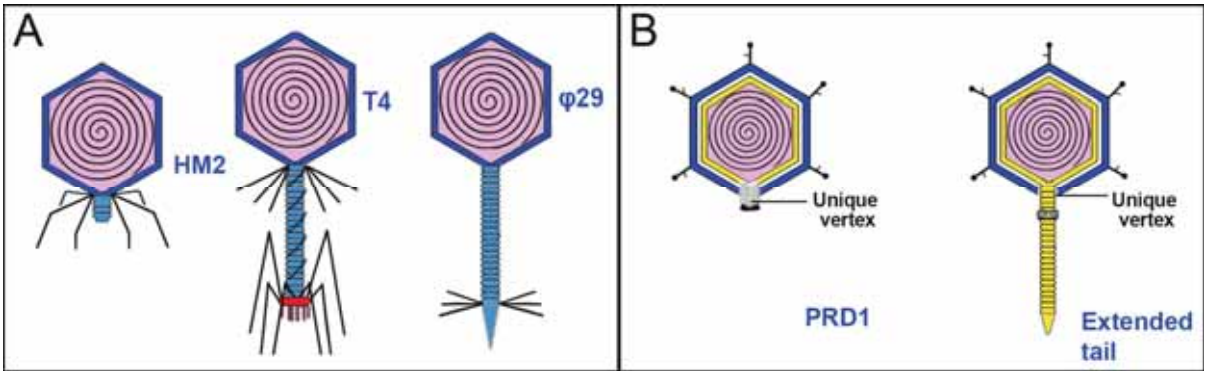

Figure 1.1: Morphology comparison between (A) various tailed phage types (podovirus HM2, myovirus T4, syphovirus φ29) and (B) a tail-less phage with an internal vesicle that forms a tube upon infection (PRD1).

This thesis targets bacteriophage PRD1, a prototype for membrane-containing viruses (Abrescia et al., 2004, Bamford and Mindich, 1982, Bamford and Bamford, 1990, Butcher et al., 2012, Cockburn et al., 2004, Grahn et al., 2002b, Hong et al., 2014, Huiskonen et al., 2007, Martin et al., 2001, Mindich et al., 1982, San Martin et al., 2002, Santos-Perez et al., 2017, Stromsten et al., 2003). The thesis investigates the mechanical properties of PRD1 and provides novel insights into such a type of viral particles. Then, as PRD1 and other recently discovered bacteriophages infect the host-cell via the formation of a nanotube (Scholl, 2017, Nilsson, 2014, Parisien et al., 2008, Qadir, 2015, Waters et al., 2017), we determined the structure and mechanical properties of the PRD1 DNA ejection tube by high-resolution (HR) cryo-EM and AFM.

In conclusion, this thesis is the result of an integrative structural approach that finally allows (*i*) to understand the nanomechanical properties of membrane-containing viruses and (*ii*) to propose a mechanism of the tube self-assembly and correlate its mechanical properties with its DNA shuttling function at infection.

1.1.1. Bacteriophage PRD1

PRD1 is a tailless, icosahedral virus that contains an internal lipid membrane underneath its protein capsid. The virus is roughly 65 nm in diameter, and extensive efforts have been made into solving the atomic structure of this system (Abrescia et al., 2004, Cockburn et al., 2004, Huiskonen et al., 2007, Mindich et al., 1982, Bamford and Mindich, 1982, San Martin et al., 2002). It is a member of the *Tectiviridae* family which typically infects gram-negative or gram-positive bacteria, with their spike-decorated capsid. The virion contains about 18 distinct protein species, and is roughly 66 MDa in mass (Figure 1.2). Within 60 minutes between infection and cell lysis the virion is able to replicate itself (Figure 1.3). The linear dsDNA genome and covalently attached terminal proteins are delivered, via formation of a proteo-lipidic tube, into the cell where replication occurs via a protein-primed mechanism.

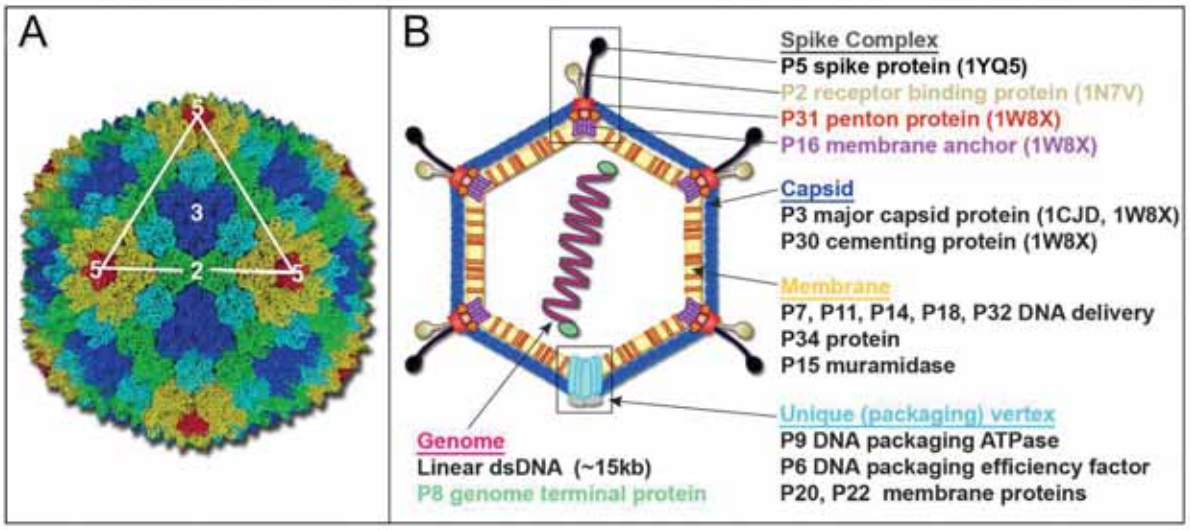

Figure 1.2: (A) PRD1 capsid organization represented as in (Abrescia et al., 2004) with each of the 4 P3 MCPs trimers composing the asymmetric unit coloured in green, cyan, blue, and yellow; in red is the vertex penton protein P31. The white triangle marks a virus facet, and 2, 3, and 5, respectively, the 2-, 3-, and 5-fold icosahedral symmetry axes. (B) Schematic presentation of wt PRD1 architecture according to the current knowledge (numbers in parentheses identify the corresponding protein structures in the Protein Data Bank).

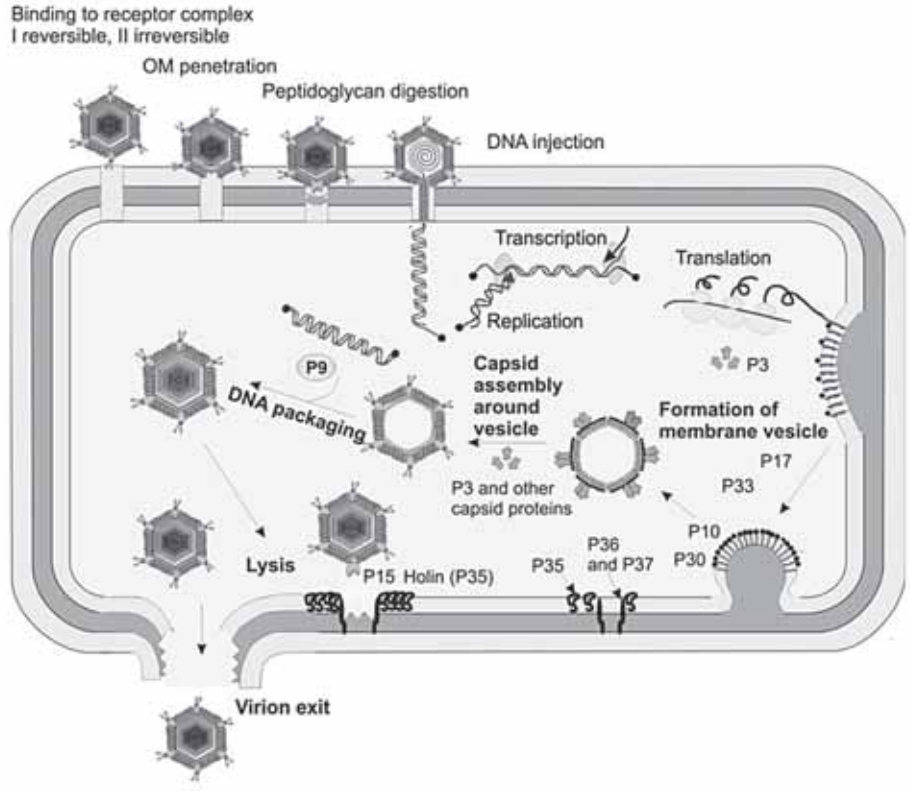

Figure 1.3: Life-cycle of bacteriophage PRD1. Adapted from (Butcher et al., 2012).

Little is known regarding the structural role of the inner-membrane in the assembly of PRD1. While there is evidence to support that it serves as an assembly platform, by close interaction with the dsDNA and the major capsid protein (MCP) P3 (Cockburn et al., 2004, San Martin et al., 2002), in this thesis we investigate whether the membrane vesicle also offers a mechanical advantage, *e.g.* a mechanical contribution to the stability of the virion. Furthermore, the membrane is used during the formation of the ejection tail tube, independently of the presence or absence of the packaged DNA (Peralta et al., 2013, Santos-Perez et al., 2017). It is proposed that the deflation of the internal vesicle, as well as loss of unique-vertex proteins can initiate the self-assembly of the tube. In **Chapter 3** of this study, we investigate both structurally, and mechanically, the mechanism behind the formation of the PRD1 DNA ejection tube.

1.2. METHODS TO STUDY VIRUS MECHANICAL PROPERTIES

There are multiple ways to study the mechanics of viruses and nanomaterials. One example is the osmotic shock method, by which bacteriophages were first incubated in high salt solutions and quickly diluted. Upon dilution, phages with capsids which are more permeable to water than to metal ions will burst. The T2, T4 and T6 phages were found to be easier to break, whereas T1, T3, T5 and T7 phages remained intact when exposed to the same treatment (Roos et al., 2007), revealing that osmotic shock method applies pressure isotropically. The aforementioned method was performed on samples with a large number of particles and provided information on the collective behaviour of virions, but the individual mechanical information is lost.

Other mechanical methods used for single particle analysis are optical tweezers. This single-molecule manipulation studies have a wide range of applications (Ashkin and Dziedzic, 1987, Heller et al., 2014, Moffitt et al., 2008, Neuman and Block, 2004, Wuite et al., 2000), and work by “trapping” the biomolecules via optically trapped microbeads that act as handles. In a study by (Moffitt et al., 2009), one bead bound to a DNA molecule and another bead to a

bacteriophage Φ29 prohead were trapped by two laser beams. By approaching the beads, the packing motion and force of DNA by the viral motor was recorded by the optical tweezers. The motor can work against a force of up to 57 pN on average, with a step size of 10 bp, which is one of the strongest molecular motors reported (Smith et al., 2001). One of the drawbacks, however, of this technique is the limited resolution of the optical microscopy, making optical trapping difficult, even when the forces and displacements can be deduced from the light diffracted by the trapped beads (Gittes and Schmidt, 1998).

Around the same period that optical tweezers were evolving, atomic force microscopy jumped from providing topographical and mechanical information of large conductive material, to providing a direct way to image and probe biological material, like individual virus particles (and other biological macromolecules), as further described in detail in the following section.

1.2.1. Introduction to atomic force microscopy (AFM)

The AFM was first described in 1986 (Binnig et al., 1986). The AFM is based on a previous technique, called scanning probe microscopy, which originally allowed imaging of solid surfaces with subnanometer resolution, and the measurement of forces as low as a few tens of pN. This ability to investigate surfaces at nanometre resolution triggered the development of a range of AFM-related techniques, which used a variety of probes to locally sense interactions and manipulate matter (Binnig and Rohrer, 1999). Imaging viruses (or any other microscopic or nanoscopic object) by AFM is often compared to the procedure a blind person may use to feel the shape of an object, by touching it with his/her fingertips. The ability to “see” depends on many factors, including proper immobilization of the sample, the sample properties (softness, adhesiveness, fragility), and the sensitivity and properties of the instrument itself. The atomic force microscope works under the following principle: a nanometer-sharp AFM tip is suspended over a sample. The primary mode of collecting topographic data was using “contact mode” by which the selected probe would scan the sample surface very closely. By

collecting the reflection of a focused laser beam, we can "feel" our sample, and by measuring the deflection of said laser, we can reconstruct a 3D topographic image of our sample (Figure 1.4A).

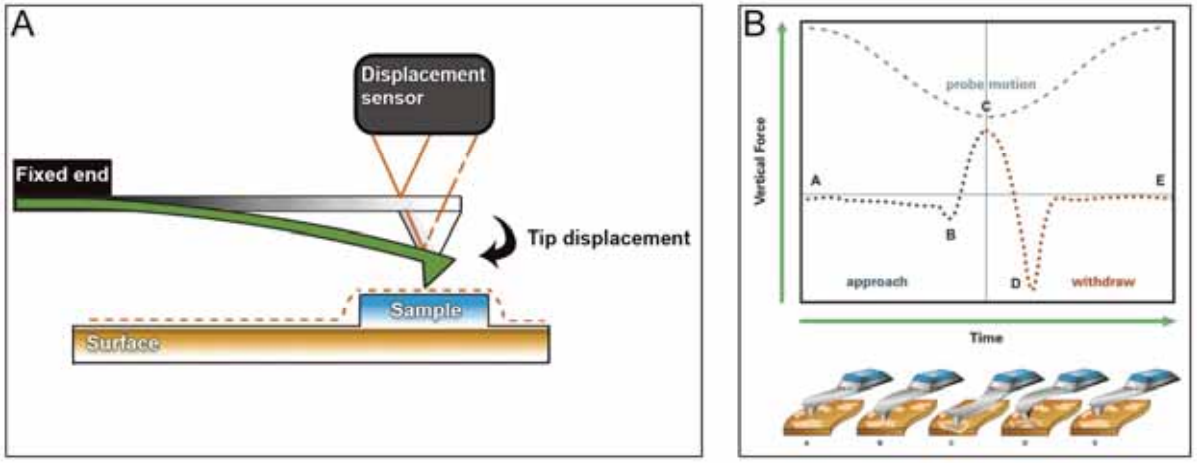

*Figure 1.4: (A) Diagram of the basic AFM components and working principle. Whilst scanning a defined area of our sample, the tip (green) displacement can be measured within nanometer precision, allowing for reconstruction of sample topography (red dashed line) based on a combination of tip and sample properties and interactions. (B) Knowing the material properties of our tip, we can also extract the mechanical and/or electrochemical information of a sample. In Peakforce tapping, the oscillation of the cantilever (with the tip) is driven by a sinusoidal wave and a force curve is simultaneously collected and displayed here as force versus time graph. The idealized sample would exhibit the indicated characteristics when approaching the surface (*A-B*), during compression/force loading* (B-C*), unloading (*C-D*), and retracting from the sample (*D-E*). Deviations from the ideal curve reveal properties of the investigated sample. Image adapted from (Kaemmer, 2011).*

1.2.2. The development of complementary imaging modes

Likewise, AFM can be used in probing the mechanical features of viruses (or any other object) since we can fine-tune force parameters and probing materials. In one particular imaging technique called "Peakforce tapping" (JPK Instruments manual. 2011. Nanowizard 4 – the next benchmark for BioAFM, Berlin), "Jumping mode" or "Quantitative imaging", force curves are collected across each pixel (Kaemmer, 2011, De Pablo et al., 1998). In Peakforce tapping, technique used in this thesis, the tip moves laterally at a constant rate irrespective of the tip being in contact with the sample or not. Then the tip moves laterally when it is not in contact with the sample. The unique versatility of AFM to image, probe and manipulate materials makes it attractive to use in nanoscience and nanotechnology. Furthermore, the possibility to

operate in liquid environments and at ambient temperature moved AFM towards biology, and led to the analysis of biomolecules and cells at (sub-) nanometre resolution. To address the wide complexity of biological systems, which can range from nucleic acids and proteins to cells and tissues, a variety of AFM modes have been developed over the years (Figure 1.5) to avoid issues with "contact mode" (CM). One of the main issues with CM are the occurrence of shear forces. These forces are present due to the friction between AFM tip and sample, potentially deforming or modifying the sample surface. Additionally, the AFM tip can be modified by adhering particulates, or damaged by these interactions, therefore affecting the measurements. Thus, new ways to minimize imaging forces were investigated, in particular when imaging soft biological material in liquid medium.

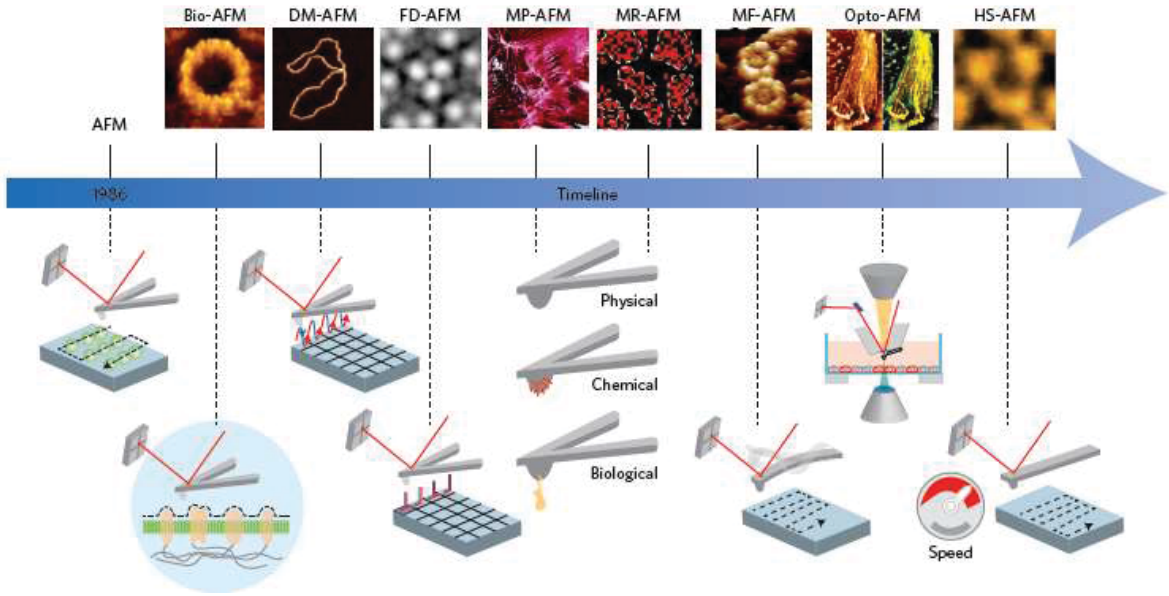

Figure 1.5: Timeline image of major developments in AFM modes for imaging biological material since the development of contact mode AFM in 1986. These include: bio-AFM that allowed operation in aqueous solutions; dynamic mode (DM-AFM) which allowed tip oscillation, reducing friction effects on the sample; force-distance AFM (FD-AFM) which records a pixel-by-pixel full distance curve while providing with a surface contour; up to high-speed AFM (HS-AFM) which increased imaging acquisition times up to a factor of 1000, allowing for investigation of dynamic biological processes. Other imaging modes include multiparametric AFM (MP-AFM), which contours the sample while mapping multiple physical or chemical properties; molecular recognition AFM (MR-AFM), which images and maps specific interactions of biological samples; multifrequency AFM (MF-AFM), which contours the sample while oscillating the cantilever tip at multiple frequencies, thus mapping various physical parameters; correlating advanced optical imaging and AFM (Opto-AFM) for the imaging of complex biological systems (Image from Dufrêne et al, 2017).

Major advances in high-resolution imaging have also been achieved in complementary methods, including super-resolution optical microscopy and cryo-electron microscopy, which enrich the imaging toolbox now available to molecular and cell biologists. DNA helices, proteins, and capsomer organization on the surface of the virus can be visualized by AFM, as was shown on brome mosaic virus crystals, mimivirus, and minute virus of mice among numerous others, including work presented in this thesis (Figure 1.6) (Carrasco et al., 2006, Kuznetsov et al., 2010, Lucas et al., 2001).

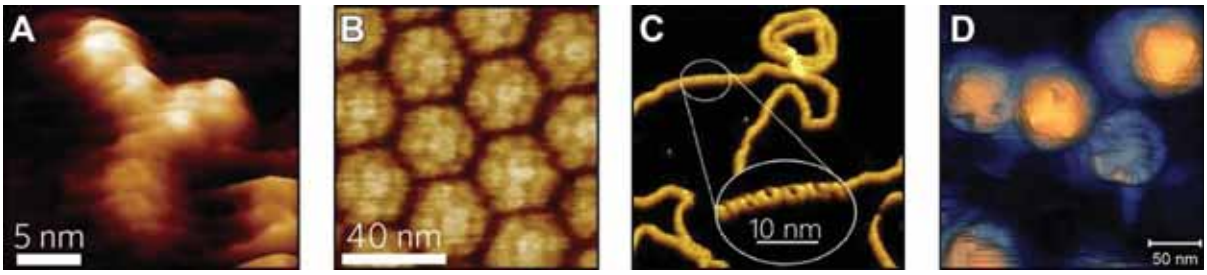

Figure 1.6: AFM images showcasing the resolution thresholds of the technique. (A) An IgG antibody visualized via FM-AFM in aqueous solution adsorbed on a mica surface. Image from (Ido et al., 2014). (B) Capsomer organization on individual brome mosaic viruses (BMV) visualized by tapping mode on BMV crystal. Image from (Lucas et al., 2001). (C) AFM topography of plasmid DNA showing major and minor grooves, obtained via PeakForce tapping. Image from (Pyne et al., 2014). (D) wt PRD1 particles showing protein organization on full and damaged particles, missing peripentonal vertices among other features (as discussed later in this thesis).

1.2.3. AFM nano-manipulation

AFM is not only capable of imaging, but also of nano-manipulating viruses. The first viral mechanical investigation with AFM appeared in 1997, when Falvo *et al.* manipulated tomato mosaic virus (TMV), a virus that is ~300 nm in length with an AFM (Falvo et al., 1997). The TMV was rotated, moved and dissected by an AFM tip. A few years later, the mechanical properties of viruses were determined by performing force nanoindentation on the bacteriophage Φ29 using an AFM tip (Ivanovska et al., 2004). By nanoindentation on virus particles, several direct mechanical properties can be extracted: (a) stiffness, which examines the elastic deformability of a particle; (b) yield force point, which examines the forces required to mechanically destroy or damage a particle; (c) resistance to mechanical fatigue, which

examines the durability of a particle when subjected to continuous forces. Since then, the method has been applied to study different viruses, including herpes simplex virus (HSV), various bacteriophages, cowpea chlorotic mottle virus, influenza virus, Norovirus, and human immunodeficiency virus, among others (Roos et al., 2009, Kol et al., 2007, Cuellar et al., 2010, Eghiaian et al., 2009, Schaap et al., 2012, Roos et al., 2012, Ivanovska et al., 2004, Carrasco et al., 2011, Michel et al., 2006). The stiffness can be directly measured from nanoindentation force curves, and represents the property of the virus particle as a whole. The majority of viruses, enveloped or not, were found to be as stiff as 0.2-1 N/m (Mateu, 2012). It is determined by the properties of the various shells (geometry and mechanical properties) from which the virus is made. Using appropriate models (analytical or finite element) and structural information, it is possible to determine the mechanical properties of individual shells (e.g. the Young's modulus of the proteinaceous capsid). The Young's moduli of most virus capsids were found to be around 1 GPa (Mateu, 2012), comparable to that of polypropylene (soft plastic material), or about 14 times less compared to that of a bone (Rho et al., 1993).

1.2.4. Understanding mechanical properties of nano-materials

AFM studies on viral mechanics help to investigate and understand the material properties of the viral particles and to unravel how it achieves the protection of the viral genome against mechanical stress. For example, one the first of such studies measured the distribution of the elastic constant over a bacteriophage Φ29 capsid. This was correlated with the protein distribution on the surface, and by intentionally rupturing the capsid, the limits of the genome protection were determined (Ivanovska et al., 2004). In other studies, the viral stiffness was measured at different physiochemical conditions correlated to viral activities. For example, stiffnening of HIV when it develops from the immature to the mature state was related to a major conformational change (the thinning of the inner protein shell) (Kol et al., 2007). Following a similar approach, we can deconstruct the mechanical contributions of the various

viral components (such as capsid, internal vesicle, and genome) to the mechanical stability of the PRD1 particle.

1.2.5. Introduction to transmission electron microscopy (TEM)

More than 100,000 proteins deposited in the Protein Data Bank have been solved using X-ray crystallography, a technique that allowed solving the atomic structure of many small and large molecules, including the atomic structure of the B-DNA back in 1953 (Watson and Crick, 1953). However, its versatility is limited by sample preparation methods and requirements, as crystals of the target nanomolecule are then blasted with X-rays and the diffraction data allow for the 3D structure determination.

Recent developments in transmission electron microscopy (TEM) has opened the way for the investigation of more complicated and biologically challenging systems that are impossible to tackle using crystallography [Figure 1.7, (Callaway, 2015, Blow, 2002)].

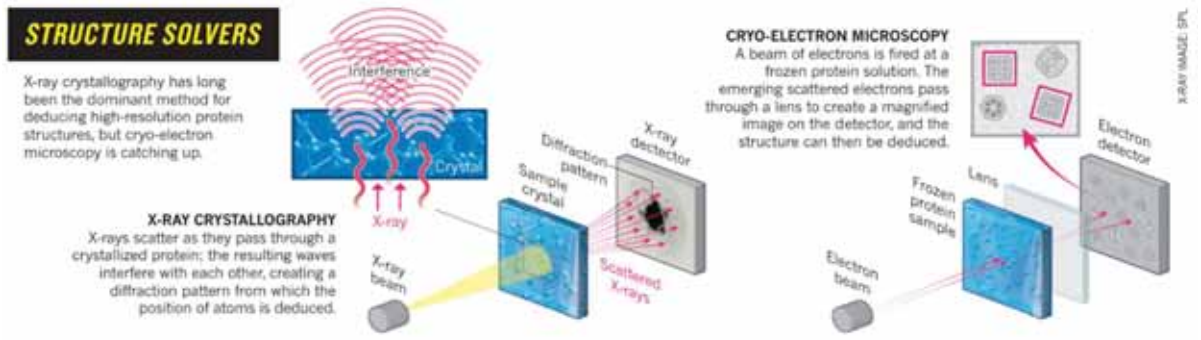

Figure 1.7: Comparison of the two major techniques used for structure solving of proteins, viruses, and other biological molecules. Image taken from Callaway, 2015.

Transmission electron microscopes were developed in the 1930's, as a consequence of the limitations that light microscopy (LM) posed. In fact, the resolution of LM has been limited by the wavelength of the light being used to form the image. Conventional light microscopes are unable to achieve better than 200 nm resolution or about half the wavelength of visible light, although in the past ten years, advances in super-resolution LM have changed this paradigm.

TEM can achieve superior resolution, due to the smaller wavelength of the electron relative to the photons from visible light. 3D structure reconstruction of viruses by TEM started via simple negative staining imaging, a technique that uses a heavy atom solution (uranyl acetate) to stain the sample (Crowther et al., 1970). At the time, resolution was limited by sample preparation methodology, radiation damage, and optical distortions. On of the cryo-EM revolution milestones was when flash-freezing the samples was introduced, enabling "close-to-native" imaging of viruses back in 1984 (Adrian et al., 1984). Since then, by implementation of automation systems (Gatan Cryoplunge, FEI Vitrobot), that helped improve the sample preparation methodology, as well as the more recent development of direct-detection cameras that allowed fast and highly-sensitive data collection, there are plenty more viruses and biological molecules structures determined using this technique.

Briefly, in cryo-EM, specimens are preserved in thin layers of vitrified ice, which eliminates the need for negative staining, reduces radiation damage and allows them to be imaged much closer to their native state, albeit at very low contrast. However, biological samples vitrified without any staining have very little contrast and can be difficult to see. Additionally, high energy electron beam can damage samples frozen in vitreous ice and result in more pronounced beam induced sample drifting (Henderson, 2015). Thus, although the 3D structure of biological macromolecules can now be solved at high resolution (3-4 Å) by cryo-EM, the low-dose data collection procedure always requires thousands of images with randomly oriented two-dimensional (2D) projections of the target molecule to be collected. Nowadays, state-of-the-art microscopes with autoloader and advanced software allow to perform data collection in automatic mode.

Advances in vitrification, in detection cameras, and implementation of Bayesian-Dyer algorithms have led to the so-called "cryo-EM resolution revolution" which has finally being recognised with the Nobel prize in Chemistry in 2017 to Richard Anderson, Joaquin Frank and Francois Dubuchet (Cressey and Callaway, 2017).

1.2.6. cryo-EM: brief overview

After sample preparation and data collection, individually selected particles are used to create a 3D structure of the desired molecule, derived from randomly oriented 2D particle projections. The single particle reconstruction is achieved by taking images of several thousand particles. Ideally, these particles will be random in orientation and the data set will contain two dimensional projections of every view of the sample. Using the central projection theorem, which states that, for a 3D object, the Fourier transform of each 2D projection is a central slice through the 3D Fourier transform of the object. The relative orientation is assigned (Euler angles) across all prior projections of the object and, by direct Fourier inversion, the 3D volume is reconstructed (Milne et al., 2013).

The Fourier transforms of the two-dimensional particles are combined computationally in three-dimensional Fourier space. The combined Fourier transform data is then inversely Fourier transformed back into real space in three dimensions to produce an electron density map of the target particles that was imaged. In general, the workflow for single particle cryo electron microscopy is as follows: sample optimization and freezing, data collection, motion correction, CTF correction, two-dimensional class averaging, three-dimensional class averaging, refinement, postprocessing of the final electron density map, and building an atomic model and model refinement [Figure 1.8, (Doerr, 2016)].

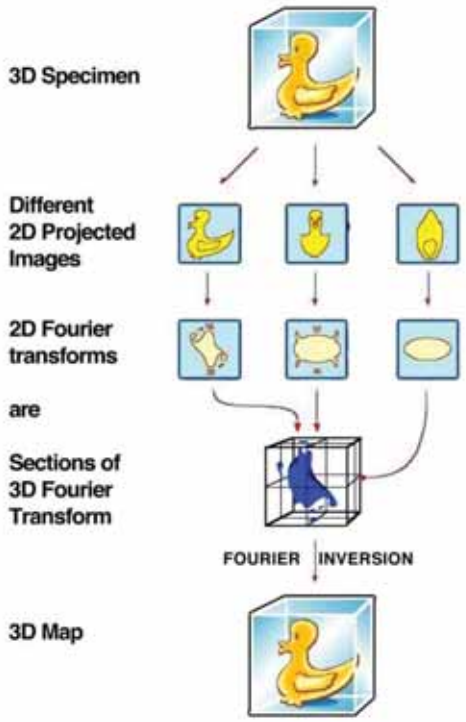

Figure 1.8: Fourier duck represents the principles of 3D structure reconstruction by Fourier inversion. The schematic illustrates that projection images of the object, each with a different orientation, have 2D Fourier transforms that correspond to sections (indicated by red arrows) through the 3D Fourier transform of the original object. Thus, once the 3D Fourier transform is built up from a collection of 2D images spanning a complete range of orientations, Fourier inversion enables recovery of the 3D structure. Adapted from (Milne et al., 2013).

1.2.7. Single-particle reconstruction methods

The most commonly used cryo-EM technique for the 3D structure determination of macromolecules, is the single-particle method. In this technique, data from a large number of 2D projection images, featuring identical copies of a protein or of a viral particle in random orientations, are processed to generate a 3D reconstruction of the macromolecule. Starting with images of fields containing many molecular complexes, individual particles are selected by hand or by automated algorithms. Once selected, a number of computer programs such as EMAN (Ludtke et al., 1999), SPIDER (Shaikh et al., 2008) and recently RELION (He and Scheres, 2017), which stood out by introducing the Bayesian maximum likelihood algorithm can be used for image processing. The degree of relatedness, whether using cross-correlation or likelihood criteria, between individual "particle" images is used to identify clusters of

similar images within the data set. Related images are then averaged to obtain characteristic projection views of the complex at much higher signal-to-noise ratios than in the original images. Iteration of this classification process, using characteristic views of the newly generated class averages as alignment references, improves the accuracy of alignment and permits visualization of finer structural features.

Statistical methods, such as principal component analysis, multivariate analysis or covariance analysis, can be used to sort images based on variations in their structural features. There are two main routes to determine the 3D structure of the target macromolecule:

1) "*Ab initio"* reconstruction assumes no prior knowledge of the structure and by applying the central projection theorem, the initial 3D structure is reconstructed.

2) Projection matching technique is used when a 3D model of a similar molecule or structure already exists (or the initial model from *ab initio* reconstruction can be used). By comparison with the 2D re-projections of the initial model, Euler angles are assigned to the raw 2D images. The raw data, with the assigned Euler angles, are then back projected to generate the 3D structure.

When X-ray atomic models are available for some or all of the sub-components of the complex, they can be placed or fitted into the density map to provide pseudo-atomic models, considerably extending the information obtained by electron microscopy (Orlova and Saibil, 2011). However, nowadays the achieved high-resolution cryo-EM maps allow modelling from scratch, of the corresponding atomic models (eg. by using COOT) and their structure refinement via Phenix software and/or Rosetta (Emsley et al., 2010, DiMaio et al., 2013).

1.2.8. Single-particle icosahedral reconstruction methods

Icosahedral viruses have been used in the past to push the limits of cryo-EM (Jiang et al., 2008). Two factors account for this:

(1) The presence of high symmetry (eg. 60-fold) confers a powerful advantage for averaging the icosahedral asymmetric unit within each virion, and

(2) The large size of the virions (tens of megadaltons in most instances) provides good contrast, in principle, for accurately determining particle orientations in projection images.

The ordered packing arrangement also lowers conformational heterogeneity of viral protein components. Icosahedral EM processing uses the same work-flow as single-particle methodology, but it imposes the icosahedral symmetry during classification and 3D particles refinement (Scheres, 2016). Because of the above characteristics, structures of numerous icosahedral viruses have been determined to resolutions better than 4 Å (Grigorieff and Harrison, 2011). An important step in the field was when the cryo-EM structure of adenovirus was solved at 3.8 Å, matching the simultaneously solved X-ray resolution (Reddy et al., 2010, Liu et al., 2010).

1.2.9. Helical reconstruction methods

Helical reconstruction has been used to determine the 3D structure of a variety of bacterial and archaeal pili, bacteriophage tubes among other systems (Craig et al., 2006, Trachtenberg et al., 2005, Leiman et al., 2010, Kahn et al., 1991). The ability of cryo-EM to deterimene helical structures was proven when the tube of the T4 bacteriophage (Leiman et al., 2010, Leiman et al., 2004) was solved. The overall workflow is similar to that of single particle reconstruction, with the additional and important step of determining the helical parameters (pitch, rise, number of subunits). These parameters are usually extracted by calculating the Fourier transform of the best 2D class averages (red star on Figure 1.9). Briefly, after obtaining the desired 2D class, the fourier transform is calculated, leading to an optical diffraction pattern. The spots and layer lines of this pattern can be interpreted in terms of a Bessel function.

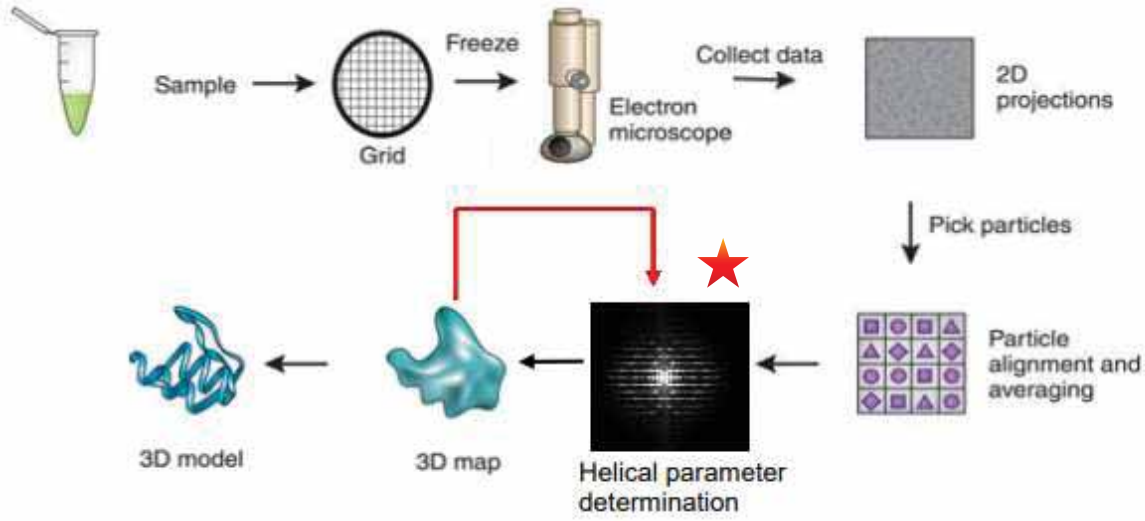

Figure 1.9: An overview of the workflow for helical data processing. While it is very similar to single particle reconstruction workflow, there is an extra and crucial helical parameter determination step (red arrow). Figure adapted from (Doerr, 2016).

A Bessel function is a cylindrical harmonic function where the Bessel order (n) is an integer value. When the solutions to a cylindrical harmonic function are plotted in three dimensions, the result is a wave. The arrangement of subunits in a helical polymer can be described by a series of characteristic cylindrical harmonic functions which are unique to that tube or complex. This allows extraction of the preliminary helical parameters that can be applied to the first round of processing and 3D reconstruction.

Molecular complexes with helical symmetry are a unique challenge for cryo-EM reconstructions. We can reconstruct correctly the corresponding 3D structure by imposing the existence of a helical symmetry via the assignment of estimated rise and pitch values during 3D model refinement (Egelman, 2000). There is usually a limited amount of views due to the nature of the complexes; for example, top views of the complex are mostly missing. Yet applying incorrect helical parameters to the reconstruction will result in model bias, just like imposing an erroneous symmetry for single particle reconstruction, and an incorrect structure. Software like RELION recently implemented calculations that allow embedding helical symmetry operators in Fourier-space, allowing for helical structure 3D reconstructions (He and Scheres, 2017).

Chapter 2: Objectives

2. OBJECTIVES

The objectives of this doctoral research are:

1. **Investigation of the role of the architectural constituents in the mechanical stability of PRD1 via atomic force microscopy, to address the following questions:**

   a. What is the role of the outer protein capsid?

   b. Does the role of the inner proteo-lipidic membrane contribute to the stability?

   c. Does the dsDNA have a role in particle stability?

   d. How the conjunction of these constituents contributes to the overall virus stability and life-cycle?

2. **Investigation of PRD1's proteo-lipidic tube via atomic force microscopy and cryo-electron microscopy, to address the following questions:**

   a. Is the PRD1's tail tube structured?

   b. What are the mechanical properties of PRD1's tube?

   c. What does the combination of this information reveal about the assembly of the tube?

Chapter 3: PRD1 virion exhibits mechanics of a composite material for genome protection

3. PRD1 VIRION EXHIBITS MECHANICS OF A COMPOSITE MATERIAL FOR GENOME PROTECTION

The multidisciplinary work presented in this chapter is currently in press in Nanoscale, and it is attached on the end of this thesis.

Stavros Azinas,[a,b] *Fouzia Bano,* [b] *Ireneo Torca,* [c] *Dennis H. Bamford,*[d] *Gustavo A. Schwartz,* [e] *Jon Ander A. Esnaola,* [c] *Hanna M. Oksanen,* [d] *Ralf P. Richter,*[b,f,g] *Nicola G. A. Abrescia* [a,h]

[a]CIC bioGUNE, Spain; [b]CIC biomaGUNE; San Sebastian, Spain; [c]Mondragon University; Arrasate-Mondragón, Spain; [d]University of Helsinki, Finland; [e]Centro de Física de Materiales, (CSIC-UPV/EHU); San Sebastian, Spain; [f]University of Leeds; Leeds United Kingdom; [g]University Grenoble; St. Martin d'Hères, France; [h]IKERBASQUE, Basque Foundation for Science; Bilbao, Spain

My contribution: After receiving the purified PRD1 particles, I performed all atomic force microscopy experiments and data analysis. I also contributed to data interpretation, and figure preparation. Furthermore, I wrote the first draft of the article and helped to complete the article for publication.

3.1. INTRODUCTION

Virions (infectious virus particles) are nano-sized carriers of information whose objective is to infect a host cell and generate progeny that can, in turn, repeat the infection cycle. When traveling outside of the host cell, virions may encounter harsh environmental conditions. Knowledge of the deformability (stiffness, *k*), the energy required for mechanical failure (toughness, *T*), and the limits to fatigue for virions has been acquired through studies using atomic force microscopy (AFM), but mainly for viruses that do not have an internal membrane (Hernando-Perez et al., 2014, Llauro et al., 2016, Carrasco et al., 2006, Michel et al., 2006). The mechanical properties of these virions ultimately recapitulate the molecular interactions across the viral icosahedral shell (Carrasco et al., 2011, Dimitriadis et al., 2002). There is no comparable information available for icosahedral virions in which an internal membrane vesicle surrounds the densely packaged DNA and, to our knowledge, such viruses with RNA genome have yet to be identified. Defining how membrane and capsid provide protection to the genome within will provide new insights into the function and properties of biological materials, thereby inspiring the design of novel nanostructures.

PRD1, the prototype for icosahedral dsDNA viruses with an internal membrane, is a large and complex enterobacterial virus (family Tectiviridae; ~65 nm mean diameter, Figure 3.1B, left). Its crystal structure revealed the molecular interactions across the major capsid proteins (MCPs) P3 and with the membrane (Abrescia et al., 2004, Cockburn et al., 2004). P3 trimers (capsomers) are arranged in the group of nine (GON) layout in the virion facets (Figure 3.1). Minor capsid protein P30 cements the edges of the icosahedron. Eleven of the twelve vertices are capped by peripentonal P3 trimers and by spike complexes (Abrescia et al., 2004, Cockburn et al., 2004, Huiskonen et al., 2007, Jaatinen et al., 2004, Xu et al., 2003) (Figure 3.1). The internal membrane enclosing the densely packaged dsDNA is composed of a roughly equal mass of lipids and membrane proteins (Cockburn et al., 2004). The twelfth vertex is the unique,

membrane-embedded portal used for DNA packaging into the procapsid and later for DNA ejection via the formation of a proteo-lipidic tube (Hong et al., 2014, Peralta et al., 2013).

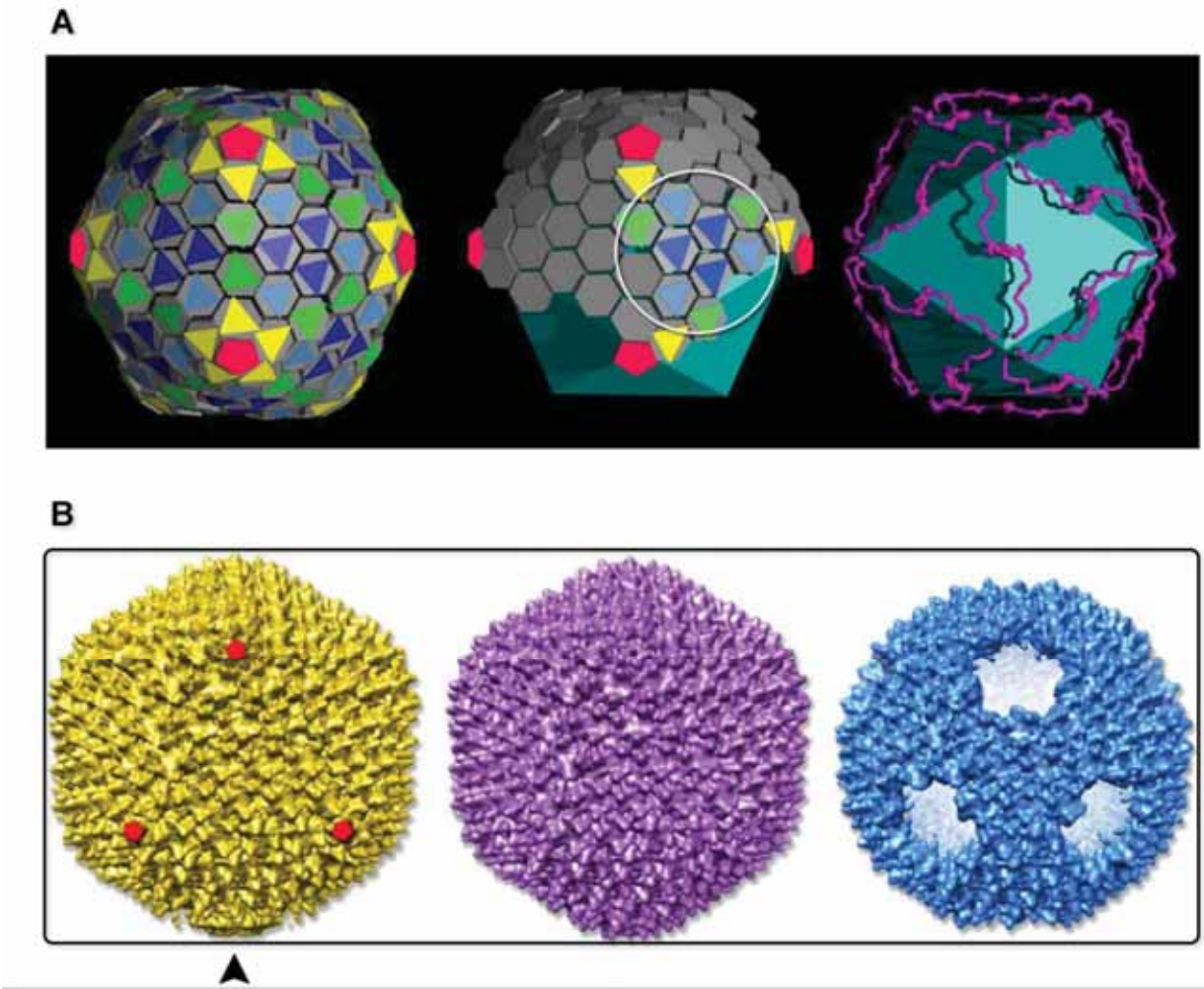

Figure 3.1: (A) Left: schematic representation of PRD1 where the P3 major capsid protein with a double β-barrel fold forms trimers (colored triangles) with the morphological appearance of pseudo-hexagons (grey). The yellow (peripentonal), green, light-blue and blue triangles indicate the independent capsomers within the icosahedral asymmetric unit; red corresponds to the penton protein composed of P31 protein. P31 is part of the spike complex that also contains membrane protein P16, spike protein P5, and receptor binding protein P2 (not shown). Centre: as in left, but with lower capsomers removed to reveal the underlying membrane vesicle (cyan). The white circle marks capsomers forming the group of nine (GON; green, light-blue, and blue triangles) that constitutes the central part of a virus facet. Right: schematic PRD1 with all capsomers S3 removed to show the presence of the cementing protein P30 (magenta) running along the facets of the virus; (B), Left: cryo-EM map (C1 symmetry) of PRD1 (EMDB: 5984) at 12 Å resolution (contoured at 0.5 threshold-level in Chimera) showing the spiky appearance of the particle due to the β-barrels of the P3 major capsid proteins. Red pentagons mark the five-fold vertices of a triangular virus facet and the black arrow-head indicates the unique vertex. Centre: cryo-EM map of Sus1 procapsid at 14 Å resolution (EMDB: 1013), contoured at 2.3 threshold-level. A unique vertex is not visible because the map is 60-fold averaged. Right: cryo-EM icosahedral map of P3-shell particle at 12 Å resolution (EMDB: 1014) contoured at 3.0 threshold-level.

3.2. MATERIALS AND METHODS

3.2.1. PRD1 virion production

Wild type (wt) PRD1 (Olsen et al., 1974) and mutant sus1 [amber mutation in gene IX] were propagated on *Salmonella enterica* serovar Typhimurium strain DS88 or on suppressor strains PSA(pLM2) or DB7156(pLM2) (Mindich et al., 1982, Mindich et al., 1976, Bamford and Bamford, 1990, Winston et al., 1979). Cells were grown in Luria-Bertani (LB) medium at 37 °C. For production of wt and mutant phage particles, DS88 cells were infected using a multiplicity of infection of 8–10. For mutant particle production, infected cells were collected 15 min after infection (Sorvall rotor F12, 5000 rpm, 10 min, 22 °C) and transferred to fresh pre-warmed medium. Virus particles were purified by polyethylene glycol-NaCl precipitation and rate zonal ultracentrifugation in sucrose (Sorvall rotor AH629), as previously described (Bamford and Bamford, 1991). For AFM, wt PRD1 and Sus1 procapsids were further purified by equilibrium ultracentrifugation in sucrose (Sorvall rotor AH629). Particles were concentrated by differential centrifugation (Sorvall rotor T647.5, 32,000 rpm, 2 h, 5 °C). A buffer containing 20 mM potassium phosphate pH 7.2, 1 mM MgCl2 was used for purification and resuspension. For P3-shell preparation, the rate zonal purified Sus1 mutant particles (2 mg/ml in 20 mM Tris-HCl, pH 7.2, 1 mM $MgCl_2$) were treated with 1% (w/v) sodium dodecyl sulfate (SDS) for 15 min at 25 °C (Luo et al., 1993). P3 shells were isolated by rate zonal centrifugation in a linear 5–20% (w/v) sucrose gradient using the Tris buffer (Sorvall rotor AH629, 24,000 rpm, 1 h 45 min, 20 °C). The particles were concentrated by centrifugation (Sorvall rotor T865, 34,000 rpm, 4 h, 5 °C) and resuspended in Tris buffer.

For membrane vesicle preparation, the rate zonal purified Sus607 particles devoid of major membrane protein P11 (1 mg/ml in 20 mM Tris-HCl, pH 7.2) were treated with 2.5 M GuHCl (Bamford and Mindich, 1982) and membrane vesicles were purified by equilibrium centrifugation in a linear 20–70% (w/v) sucrose gradient (Sorvall rotor TH641, 22,000 rpm, 16–18 h, 20 °C). Protein concentrations were determined by Bradford assay (Bradford, 1976).

Particles were analyzed using sodium dodecyl sulfate polyacrylamide gel electrophoresis (SDS-PAGE; 16% acrylamide; Figure 3.2A) (Olkkonen and Bamford, 1989). Gels were stained with Coomassie Brilliant Blue R 250 (Serva) for proteins, Sudan Black B (Sigma Aldrich) for lipids, and EtBr for nucleic acids.

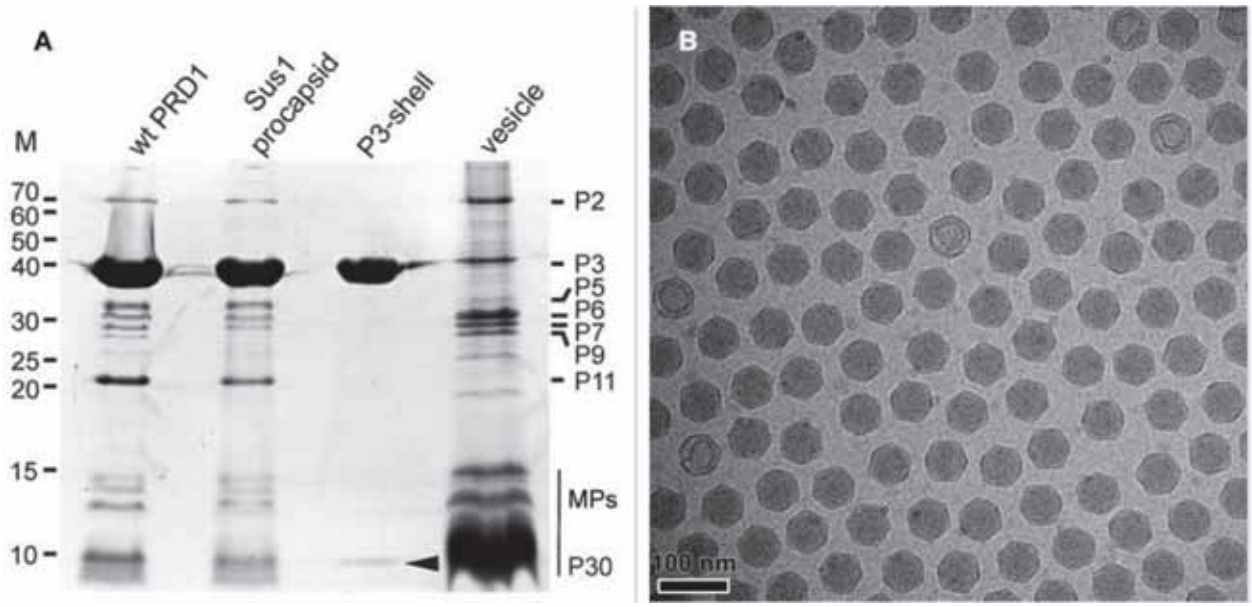

Figure 3.2: Gel (A) Cryo-EM image (B) of wt PRD1 sample after being stored for 2 weeks at 4 ºC.

Virus particles were stored at 4 °C for no more than 2 weeks. During this time, more than 95% of the wt PRD1 particles remained intact and without loss of their genome (Figure 3.2B). Sus1 procapsid, P3-shell particles and vesicles were similarly stored and also used within this timeframe.

3.2.2. Protein identification by mass spectrometry

Silver stained protein bands were cut out of the polyacrylamide gel and "in-gel" digested. Cysteine bonds were reduced with 0.045 M dithiothreitol (#D0632 Sigma-Aldrich, USA) for 20 min at 37 °C and alkylated with 0.1M iodoacetamide (#57670 Fluka, Sigma-Aldrich, USA) at room temperature. Samples were digested by adding 0.75 µg trypsin (Sequencing Grade Modified Trypsin, V5111, Promega) for overnight at 37 °C. After digestion peptides were purified with C18 microspin columns (Harvard Apparatus) according to the manufacturer's

protocol. The dried peptides were reconstituted in 30 µl of buffer A [0.1% trifluoroacetic acid (TFA) in 1% acetonitrile (ACN)].

Liquid chromatography coupled to tandem mass spectrometry (LC-MS/MS) analysis was carried out on an EASY-nLC1000 (Thermo Fisher Scientific, Germany) connected to a Velos Pro-Orbitrap Elite hybrid mass spectrometer (Thermo Fisher Scientific) with nano electrospray ion source (Thermo Fisher Scientific). The LC-MS/MS samples were separated using a two-column setup consisting of a 2 cm C18-Pepmap trap column (Thermo Fisher Scientific), followed by 15 cm C18-Pepmap analytical column (Thermo Fisher Scientific). The linear separation gradient consisted of 5% buffer B in 5 min, 35% buffer B in 60 min, 80% buffer B in 5 min and 100% buffer B in 10 min at a flow rate of 0.3 µl/min (buffer B: 0.1% TFA acid in 98% acetonitrile). Six microliter sample was injected per LC-MS/MS run and analyzed. Full MS scan was acquired with a resolution of 60 000 at normal mass range in the orbitrap analyzer and followed with CID –MS2 top 20 most intense precursor ions with in ion trap (energy 35). Data was acquired using LTQ Tune software.

Acquired MS2 scans were searched against the enterobacteria phage PRD1 (NCBI) protein data-base using the Sequest search algorithms in Thermo Proteome Discoverer. Allowed mass error for the precursor ions was 15 ppm and for the fragment 0.8 Da. A static residue modification parameter was set for carbamidomethyl +57,021 Da (C) of cysteine residue. Methionine oxidation was set as dynamic modification +15,995 Da (M). Only full-tryptic peptides were allowed for maximum of one missed cleavage.

3.2.3. Surface preparation and immobilization of PRD1 particles

Freshly cleaved surfaces (~1 cm^2) of mica (Ted-Pella Inc., CA, USA) were functionalized with 3-(2,2-aminoethylamino)-ethylaminopropyltrimethoxysilane (APTES; Sigma-Aldrich) by adapting a previously described procedure (Crampton et al., 2005). Briefly, mica was left to incubate with 30 µL of APTES in a 4 L gas incubator for 2 h. A small amount of water (10 µl) was deliberately added to generate a root-mean-square surface roughness of 1.7 to 2 nm which proved beneficial to particle attachment. Following APTES functionalization, surfaces were covered with 100 µl Hepes buffer (10 mM HEPES, pH 7.4, 150 mM NaCl, 2 mM $MgCl_2$) containing 10 µg virus particles (wt PRD1, Sus1 procapsid, or P3-shell). PRD1 vesicles were attached to freshly cleaved mica instead of APTES-coated mica. Virus particles were allowed to adhere for 30 min, and excess particles were removed by washing with buffer.

3.2.4. AFM imaging and nano-indentation

All PRD1 particles were found to attach as a monolayer to the prepared mica surfaces that could be readily visualized by AFM. Imaging and nanoindentation measurements were carried out using a MultiMode 8 AFM with a Nanoscope V controller (Bruker, CA, USA) at room temperature in Hepes buffer. Wt PRD1, Sus1 procapsids, and P3-shells were analysed with sharpened triangular Si_3N_4 cantilevers with a nominal spring constant of 0.7 N/m (ScanAsyst-Liquid; Bruker). For PRD1 vesicles, Si_3N_4 cantilevers with a nominal spring constant of 0.1 N/m (AC40; Bruker) were used. The real spring constants of the cantilevers were measured using the thermal noise method (Butt and Jaschke, 1995) as implemented in the NanoScope software and were found to be close to the nominal values. Imaging was performed in Peak Force Tapping mode, with a typical tapping amplitude of 40 nm. For wt PRD1, Sus1 procapsids, and vesicles, the peak force was usually 100 pN; for P3-shells, it was 80 pN. Under these conditions, the image quality was sufficient to reliably identify the orientation of virus particles, and in general intact PRD1 particles did not degrade or break upon repeated imaging. On already degraded particles, gradual further deterioration was observed, and particles were also

found to detach from the surface. Images were plane fitted when required, using Gwyddion software (http://gwyddion.net/) without application of noise filtering or sharpening.

Nano-indentation measurements were performed at individually selected particles using the 'point-and-shoot' function within the NanoScope software. Briefly, the area of interest was first imaged to localize the virus particle; the 'point-and-shoot' function was then activated and force curves were taken at the particle centre; subsequently, the area was imaged once more to verify successful nano-indentation. The accuracy of localization of the particle centre was found to be limited by piezo drifts and estimated to be within 5 nm. Force vs. distance (F/z) curves were acquired at a constant approach velocity of 200 nm/s. The approach and retract distances were 100 nm, corresponding to a total time of 1 s per complete approach and retract cycle. The maximal load was 4 nN, except for P3-shells were the maximal load was lowered to 2 nN. F/z curves were analysed using the NanoScope software.

3.2.5. Force curve analysis: Selection of force curves

At maximal loads of 4 nN, the AFM tip typically reached the underlying support following indentation and/or fracture of all PRD1 derived particles. We used the z distance travelled between the onset of a repulsive force and the closest approach as an indicator for successful indentation at a central particle position. The closest approach typically corresponded to hard-wall contact, though in some cases it was short of hard-wall contact by a few nm as estimated from force curves with hard wall contact acquired shortly before/after on a nearby mica area and taking advantage of the AFM's closed loop z scanner. Force curves showing distances of 60 ± 10 nm were retained for further analysis for wt PRD1, Sus1 procapsids, and P3-shells; and distances of 28 ± 5 nm were considered acceptable for DNA-filled vesicles. When imaging vesicles, we found a second class of objects with a height of 12 ± 7 nm and lateral dimensions comparable to the DNA-filled vesicles. Because cryo-electron microscopy [JEM-2200FS (JEOL) transmission electron microscope equipped with an UltraScan 4000 SP 4k x 4k camera (GATAN)] showed that the majority of prepared vesicles had contained their DNA, most likely

these are vesicles that lost their DNA upon immobilization and had flattened on the surface. These flatter objects were not further analysed.

To avoid including particles that might have been displaced or changed orientation upon indentation, force curves where force levels dropped and remained below 500 pN over distances of 20 nm and more before hard-wall contact were also discarded from analysis.

3.2.6. Determination of yield point and stiffness

After first contact between the AFM probe and a PRD1 particle at the contact point z_c, the initial monotonous force (compression) was followed by an extended and steep drop (fracture), with subsequent, typically minor, compression and fracture phases (Figure 3.3). The onset of the first drop, defined as the yield point z_y, is determined by the yield force $F_y = F(z_y)$ and the yield strain $\varepsilon_y = (z_c - z_y) / h$, where h is the mean particle height (Figure 3.4, top row panels). Neglecting the lowest forces ($F < 200$ pN), the initial part of the first compression phase for wt PRD1, the Sus1 procapsid, and the P3-shell could, in general, be approximated well by a straight line – with the exception of short stochastic slips that we interpret as micro-fractures (Figure 3.4, marked as arrows in the force curves). The particle stiffness k was determined from the slope in the initial compression phase, i.e., the slope up to the force at which the first slip or the fracture occurred. In any case, linear fits were not extended beyond 1500 pN (or strains above 10%) to avoid bias by non-linearity at larger compressions. Likewise, the stiffness was not quantified if the first slip occurred below 500 pN to avoid the large uncertainties associated with fitting a line to a small data set. Stiffness values for vesicles were extracted from linear fits to the compression curves that did not extend beyond 600 pN, but typically up to a maximum of 50% strain, as strains below 15-20 % fell within the noise limit of the measurements.

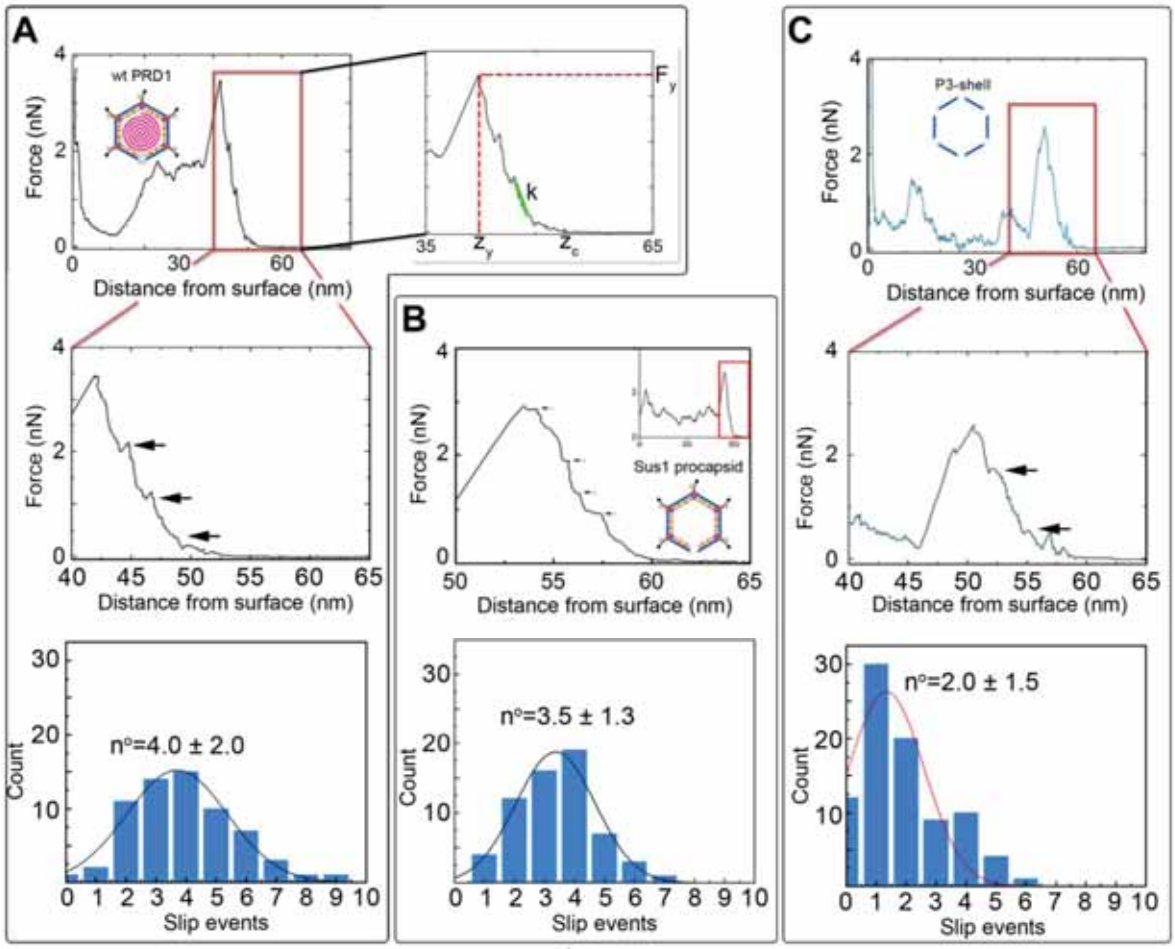

Figure 3.3: Representative force vs. distance curve of (A) wt PRD1, (B) Sus1 procapsid, and (C) P3 shell. (A; Top panels) Sample force curve with extracted parameters indicated: yield force, Fy, stiffness, k (equivalent to the negative slope of the linear fit in green), and yield strain, $\varepsilon_y = (z_c - z_y) / h$, where h is the particle height (Figure 3.4). (A-C; Middle panels) Insets highlighting stochastic slip events during loading (black arrows indicate micro-fractures). We defined a slip event as a 0.4 nm to 1.5 nm decrease in probe-sample distance that is associated with a decreasing or constant force and occurs before the particle yields. Smaller distances were discarded to avoid noise interference and larger distances were classified as yield. (A-C; Bottom panels) Histograms with Gaussian fit (mean ± s.d.) of the number of slip events (n^o) before yielding for (c) wt PRD1 and (d) P3-shells. Comparison of the mean values with the yield forces for wt PRD1 (3.0 nN), Sus1 procapsid (2.7 nN) and P3-shell (0.9 nN; Figure 3.9A) reveals similar micro-fracture rates of 1.3, 1.3 and 1.4 per nN of applied force, respectively.

3.2.7. Estimation of particle toughness

Toughness T was defined as the amount of energy E_y per volume V that the PRD1 particles can withstand before breaking. Approximating the virus as a sphere of radius R, and with $T = E_y / V$, $E_y \approx F_y (z_c - z_y) = F_y \varepsilon_y h$ and $V = 4\pi/3 R^3 \approx \pi/6 h^3$, we obtain $T \approx 6/\pi F_y \varepsilon_y / h^2$.

3.2.8. Statistical analysis

Origin data analysis and graphing software was used for statistical analysis of results (OriginLab, Northampton, MA). Gaussians were fitted to the histograms to extract the means and standard deviations (s.d.). One-way ANOVA tests were performed to determine statistical significance of differences of yield force and stiffness across the PRD1-derived particle populations. The stiffness of wt PRD1 against Sus1 procapsid yielded a P-value ≤ 0.001 (**), while the stiffness, yield force and yield strain of both PRD1 and Sus1 procapsid against P3-shell showed a P-value ≤ 0.0001 (***).

3.3. RESULTS AND DISCUSSION

3.3.1. AFM imaging of PRD1 particles

When immobilized, the wt particles oriented with a 3-fold, 2-fold, or 5-fold symmetry axis normal to the supporting surface (Figure 3.4, top row panels). The preferred orientation (> 67% of the particles) was with a facet down (i.e., a 3-fold axis normal to the surface). The average height was 67.8 ± 2.5 nm (mean ± s.d.) for wt PRD1, 66.9 ± 2.7 nm for the Sus1 procapsid, and 62.8 ± 3.5 nm for the P3-shell (n = 75 each; Figure 3.4), in good agreement with electron-microscopy and X-ray data (Abrescia et al., 2004, San Martin et al., 2002, Martin et al., 2001) (Figure 3.1B). Strikingly, we observed on the Sus1 procapsid a mild circular depression, ~13 nm in diameter at ~8% of the visualized vertices (n = 103) (Figure 3.4B; bottom row, arrowheads). This percentage, combined with the estimated dimensions, defines at the single-molecule level that this feature is the unique vertex that lacks the external part of the packaging portal (Hong et al., 2014). This, however, was not detected on wt PRD1. Indeed, the structural difference in the capsid context between the 'wild type' unique vertex and the remaining 11 vertices is much smaller than that between the unique vertex and the other 11 vertices in the procapsid (Hong et al., 2014), and apparently is too small to be resolved with our AFM set-up.

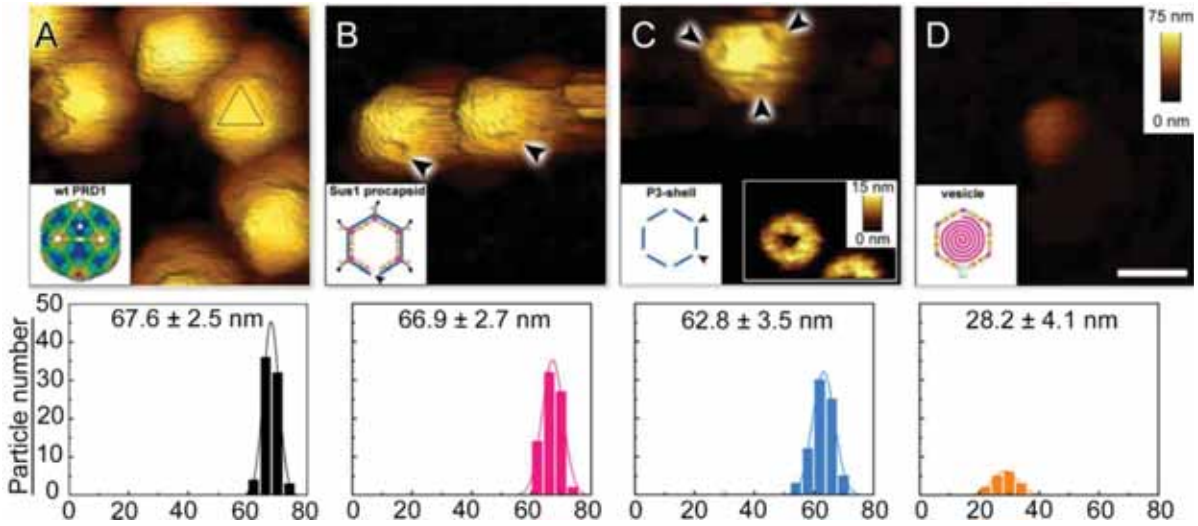

Figure 3.4: AFM images for the four populations of PRD1-derived particles (A) wt PRD1 deposited at different orientations, triangular facet marked with black triangle; (B) Sus1 procapsid with arrowheads indicating the visible depression due to the missing packaging portal in the unique vertex, (C) P3 shell with arrowheads highlight the depressions visible at all vertices due to the absence of the peripentonal capsomers and vertex complexes [Right inset: the star-shaped vertex depression at higher resolution (z range: 15 nm)], and (D) vesicle (Scale bar: 100 nm; z range: 75 nm, as indicated in D top row). Bottom row shows height histograms corresponding to each particle population.

P3-shells showed holes, ~25 nm wide, at each vertex (Figure 3.4C; bottom row, arrowheads) consistent with the missing peripentonal P3 capsomers, spike complexes, and internal vesicle (Martin et al., 2001, San Martin et al., 2002) (Figure 3.1B). The forces were lowered from ~100 to ~80 pN to enable imaging of P3-shells indicating that these particles are more sensitive to breakage compared to wt PRD1. By contrast, vesicles displayed a featureless surface and a height of 28.2 ± 4.1 nm (Figure 3.4D). This height is less than the diameter of DNA-containing vesicles (~35 nm) (Cockburn et al., 2004) indicating that vesicles readily deform when immobilized.

3.3.2. Mechanical properties of PRD1 particles

To investigate the different response and nanomechanical properties of wt PRD1, Sus1 procapsid, P3-shell, and genome-containing lipid vesicle populations, individual indentations were performed using AFM in PeakForce mode (see Methods). The mechanical properties of interest are: stiffness (*k,* at <10% strain), defined as the rigidity of the particle or the extent to

which the particle resists deformation; the yield force (F_y), and yield strain (ε_y) defined as the force and strain at the point of mechanical failure of the particle. All these properties were extracted from the AFM force vs. distance (*F/z)* curves (for more detubes see methods and Figure 3.3A). A representative force curve for each PRD1 particle type with AFM micrographs before and after indentation is shown in Figure 3.5.

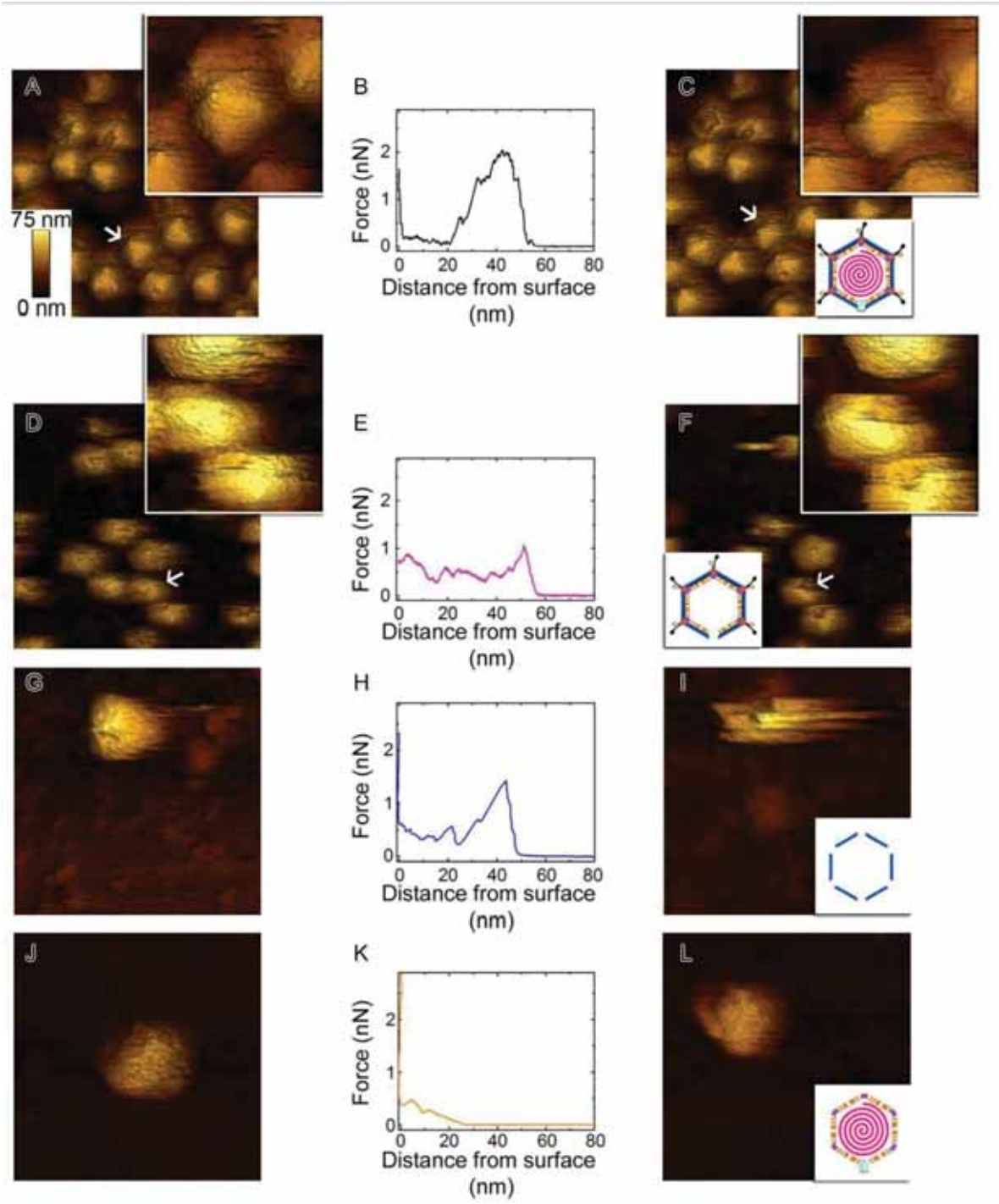

Figure 3.5: Consecutive images of PRD1 particles before [A, D, G and J] and after [C, F, I and L] nanoindentation; schematics identify the corresponding particle types, from top to bottom: wt PRD1, Sus1 procapsid, P3-shell, and vesicle. B, E, H and K represent a single mechanical indentation, with

the corresponding force curve obtained for each particle type. Image size: 500 nm; z range: 75 nm (see color key in A). The indented particle is marked with an arrow in A, C, D, and F; insets show enlarged images (image size: 160 nm) of the indented particle - from A and C insets at least twelve capsomers appear to be displaced. Upon acquisition of the force curve shown in E, the z travel was set slightly too short to capture the hard wall contact. The indicated distance, therefore, should be considered as being marginally smaller than the real distance from the surface.

3.3.3. Stiffness

The F/z curves typically exhibited a relatively small non-linear regime at the smallest indentation forces (F < 200 pN) which is likely to represent the Hertzian deformation of the capsid shell. This was followed by an extended linear regime, justifying quantification of elastic properties in terms of the stiffness k. For quantitative stiffness analysis, we considered this linear regime for strains up to 10 % which was well below the yield point. For quasi-spherical shells such as the Sus1 procapsid and the P3-shell, this linear regime can be associated with shell bending (Kononova et al., 2016).

wt PRD1 possessed the greatest stiffness (0.57 ± 0.03 N/m, mean ± s.e.m.), followed by the Sus1 procapsid (0.39 ± 0.02 N/m) and the P3-shell (0.22 ± 0.01 N/m; Figure 3.6). Most likely, the enhanced resistance of wt PRD1 to elastic deformation arises from pressure exerted by the DNA (Cockburn et al., 2004, Santos-Perez et al., 2017). PRD1 genome packaging produces a radial expansion of the internal membrane (*e.g.* the radius of the outer leaflet increases by ~ 6%), which presses the vesicle closer to the capsid (Santos-Perez et al., 2017, San Martin et al., 2002, Hong et al., 2014).

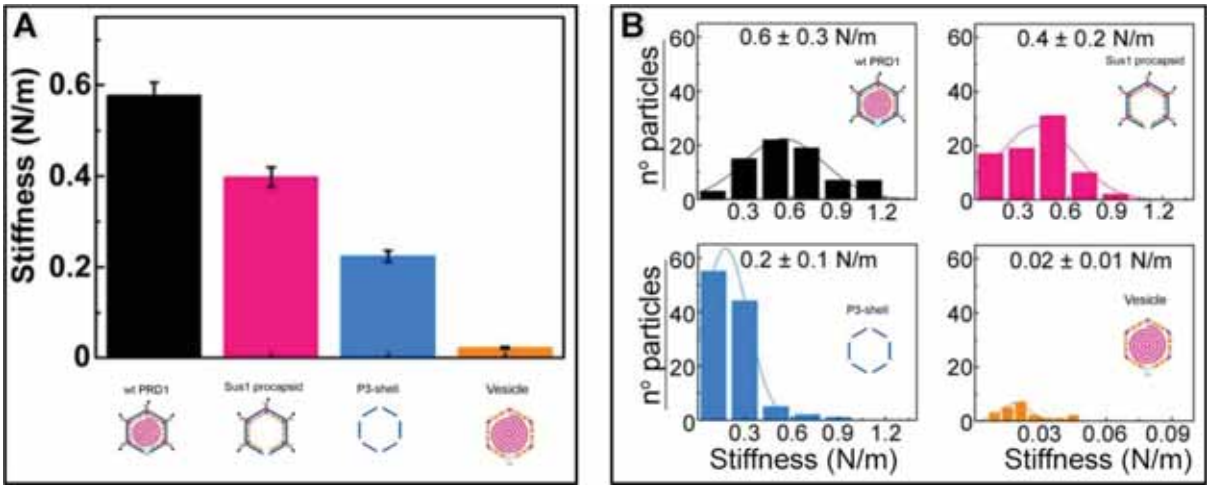

Figure 3.6: (A) Comparison of the stiffness data for each of the four PRD1-derived particles, reporting mean values and standard error. These values were derived from (B) stiffness histograms of the four viral particle types, reporting mean values and standard deviations for each. (y-axis: number of particles. x-axis: stiffness value).

The DNA-filled vesicle displayed the least stiffness (0.022 ± 0.002 N/m; Figure 3.6A), indicating that its direct effect on virion stiffness is marginal but that it contributes to virion stiffness by transmitting pressure from the DNA to the capsid. The volume inside the rigid capsid is reduced upon indentation accentuating the effect of DNA pressure on the stiffness of wt PRD1. In contrast, the soft membrane can stretch upon indentation thus reducing any effect of DNA pressure on vesicle stiffness. To confirm this, we confronted the experimental data with continuum-mechanics finite-element computational modelling (detailed in the next section) in which the proteinaceous capsid and the proteo-lipidic vesicle were represented as mechanically isotropic and linearly elastic spherical shells. This model neglects the structural detubes of each shell but can effectively deal with the architectural complexity introduced by the presence of the vesicle. The model also provides an estimate for the Young's modulus of the PRD1 proteinaceous shell of E = 0.22 GPa, a value comparable to that for some non-

enveloped and enveloped viral capsids (Mateu, 2012). The reduced stiffness of the P3-shell (E = 0.13 GPa) is likely due to the absence of the stabilizing pentons and peripentonal capsomers.

3.3.4. Modelling of PRD1's elastic properties through finite-element analyses

To test how the membrane vesicle affects stiffness in a composite system of a proteinaceous capsid shell with an underneath membrane vesicle, modelling of the mechanical response of PRD1 was performed using a continuum-mechanics finite-element analysis (FEA) with the software ABAQUS 6.14 (ABAQUS, Fremont, CA) (Figure 3.7 and Figure 3.8). In this approach the proteinaceous capsid and the proteo-lipidic vesicle were represented as mechanically isotropic spherical shells, i.e., neglecting the structural detubes of each shell (Figure 3.7A). This method can effectively deal with the architectural complexity introduced by the presence of the vesicle whilst the number of adjustable parameters is kept small.

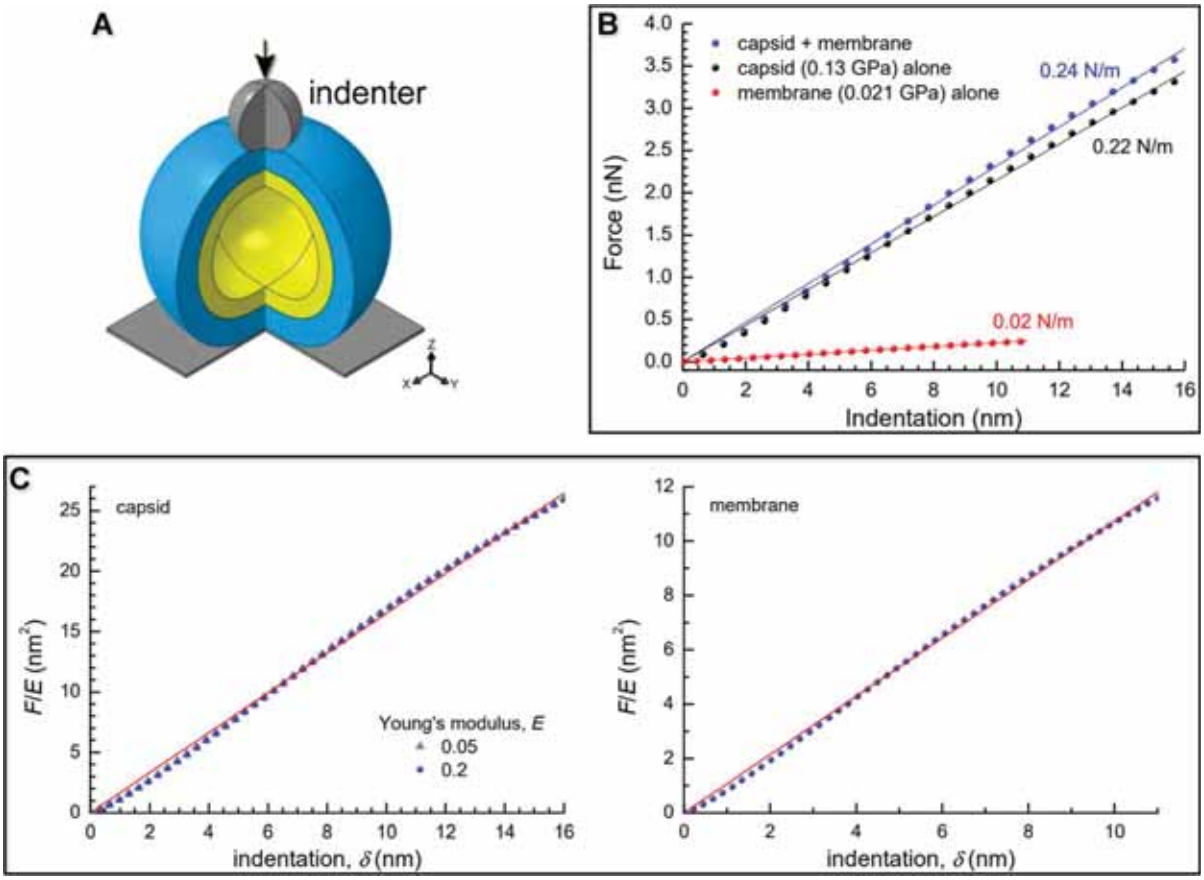

Figure 3.7: (A), Schematic of the spherical two-shell model (outer protein shell in blue, inner vesicle shell in yellow) for the finite-element modelling; three-quarters of the spheres are shown with the indenter apex represented as a grey sphere with the direction of the applied force as indicated by the black arrow; in the bottom right corner the Cartesian coordinate system; (B), Predicted curves of force vs. indentation for a protein shell (with E = 0.13 GPa, representing the P3-shell; black dots), a vesicle shell (with E = 0.021 GPa, representing the proteo-lipidic vesicle; red dots) and a composite of these protein and vesicle shells (blue dots). In matching colours: lines are linear fits through the origin, and texts the stiffness values corresponding to the slopes. The stiffness values of protein and vesicle shells match the experimental data for P3-shell and vesicle (Figure 3.6), respectively, confirming the correct choice of Young's modulus values; the stiffness of the composite is well approximated by the sum of the stiffness values of the constituent shells and thus only marginally larger than the stiffness of the protein shell alone. (C) Simulations with finite-element analysis. (left panel), Elastic shell (capsid): force scaled with Young's modulus F/E vs. indentation δ for a single spherical shell with a size representing the PRD1 capsid (outer radius R = 33.2 nm, thickness d = 8 nm). Data for E = 0.05 GPa and 0.2 GPa are shown (grey triangles and blue dots, respectively); these overlap fully, demonstrating that the Young's modulus is a simple scaling parameter and does not affect the curve shape. The red line is a linear fit through the origin (slope α = 1.65 nm); (right panel), Elastic shell (membrane): F/E vs. δ for a single spherical shell with a size representing the membrane (R = 25.2 nm, thickness d = 5.5 nm). The red line is a linear fit through the origin (slope α = 1.07 nm). All data shown here were computed with a Poisson ratio of 0.4.

In the FEA simulation the particle was placed between a rigid plane and a rigid indenter. Displacement of the rigid plane was constrained, and the indenter apex was modelled as a sphere of 10 nm radius positioned coaxially with the virus-derived particle in the direction normal to the plane (Figure 3.7A). For indentation, the indenter applied a force in the direction normal to the plane. Contact between all bodies was assumed to be hard in the direction normal to the contact (i.e., interpenetration was not allowed) and frictionless in the tangential direction (i.e., relative displacement and rotation were allowed with no constraint).

To extract material elasticity from the experimental data, we first considered the proteinaceous capsid individually. For the capsid, we estimated an outer radius R = 33.2 nm and a thickness d = 8 nm from rotationally averaged electron density maps of the PRD1 virion (San Martin et al., 2002, Santos-Perez et al., 2017). Treating the capsid as isotropic and linearly elastic, its properties can be described by two independent parameters: Young's modulus E and the Poisson ratio ν. Neglecting a non-linear regime at very small strains (< 3 %), the predicted relation between force and particle indentation δ was approximately linear and scaled with the Young's modulus E for indentations up to 2d (ε up to 24 %; Figure 3.7C). Our results were rather insensitive to the Poisson ratio (Figure 3.8A-C), and we thus fixed ν = 0.4. These features are consistent with previous computations by others (Ivanovska et al., 2004, Pauchard and Rica, 1998, Michel et al., 2006) and with the predictions of thin-shell theory (Michel et al., 2006), and thus validate the numerical model. The linear relationship between force and indentation is also consistent with our experimental data (Figure 3.5) where we note that the strain regime of □ < 10% used for the analysis of experimental data lies well within the range over which theory predicts a linear response. This implies that stiffness analysis is far away from any buckling transition. It justifies the use of linear elasticity in our simple theoretical model, and also the use of stiffness $k = F/\delta$ to characterize the shell's elastic properties. With $F/E \sim \delta$ and $k = F/\delta$, it is also clear that $k \sim E$, and a linear fit to the data in Figure 3.7B gives $k \approx 1.65$ nm

× E. With this equation, we estimate E = 0.13 GPa for the P3-shell from the experimentally determined mean stiffness value for this particle (k = 0.22 N/m; Figure 3.6B).

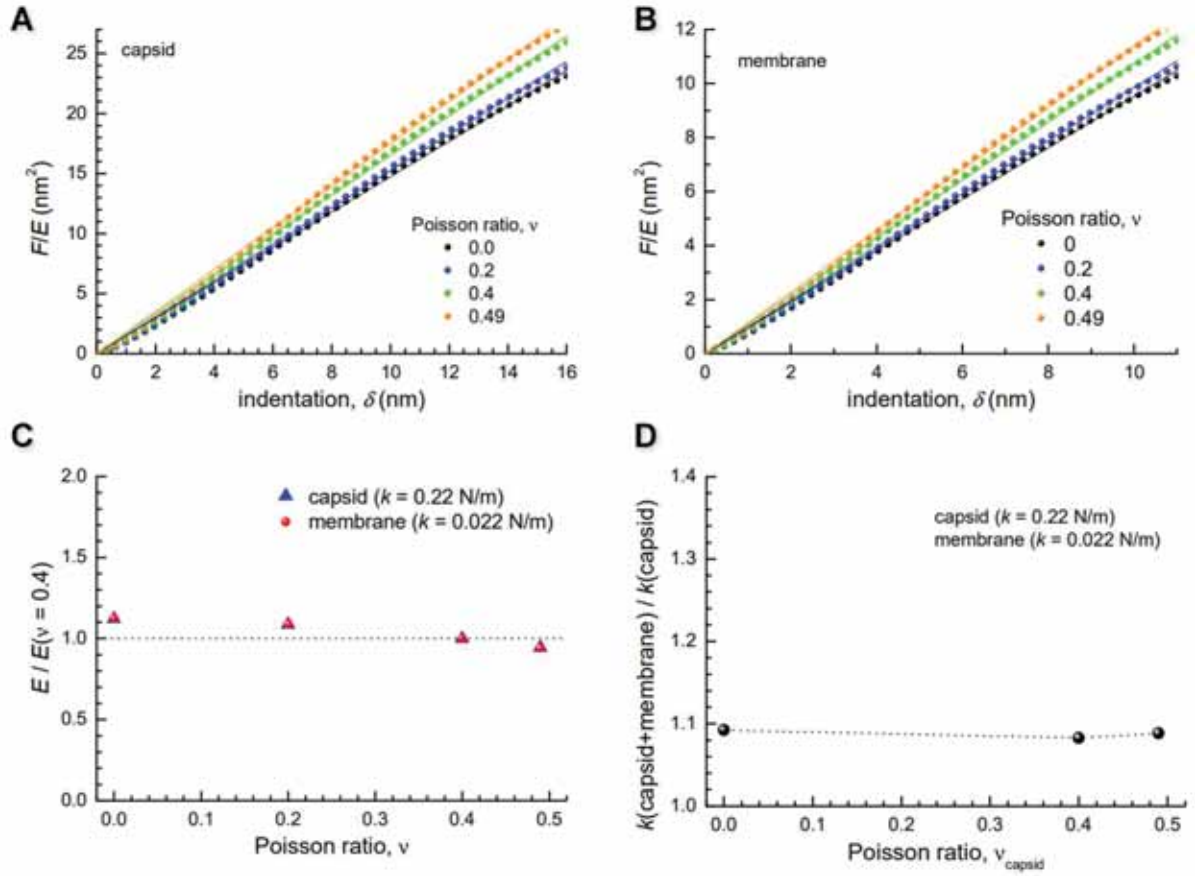

Figure 3.8: Test of sensitivity to Poisson ratios. All data shown are from simulations with finite element analysis, analogous to Figure 3.7. (A)-(B), Force scaled with Young's modulus F/E vs. indentation δ for single elastic spherical shells with a size representing the PRD1 capsid (outer radius R = 33.2 nm, thickness d = 8 nm; (A)), and the membrane (R = 25.2 nm, thickness d = 5.5 nm; (B)). Data for selected Poisson ratios ν ranging between 0 and 0.49 (as indicated in the panels) are shown as symbols. The lines in matching colors are linear fits through the origin, and reproduce the data equally well for all ν. (C), Young's modulus E vs. Poisson ratio ν for a capsid with stiffness k = 0.22 N/m and a membrane with stiffness k = 0.022 N/m (i.e. values close to those observed experimentally for the P3-shell and the vesicle, respectively, cf. Figure 3.6). E is normalized by the Young's modulus value obtained at a Poisson ratio ν = 0.4, and the data show that variations relative to this reference are generally small (from -6% to 12%). (D), Enhancement in stiffness k predicted for the capsid-membrane composite compared to the capsid alone as a function of the capsid's Poisson ratio. The relative enhancement is virtually independent of the capsid's Poisson ratio. The membrane's Poisson ratio did not affect k of the capsid-membrane composite appreciably (not shown).

A recent computational modelling study on a smaller non-membrane containing virus has shown that capsid proteins can dynamically re-structure upon capsid indentation with appreciable effects on capsid elasticity compared to an idealized homogeneous shell. Our experimental data do not allow deconvoluting these effects (Kononova et al., 2018). However,

the extended linear regime in the F/z curves observed experimentally for the P3-shell and the Sus1 procapsid indicates that the bending elasticity of the PRD1 capsid shell remains appropriately described by a Young's modulus (where this would effectively include the possible re-structuration effects). To predict the mechanical behaviour of the composite capsid-membrane system, we modelled a system of two concentric shells with the inner shell adopting the geometry and Young's modulus of the membrane and the outer the geometry and Young's modulus of the P3-shell (Figure 3.7A). The stiffness of this composite system was k = 0.24 N/m, that is, the presence of the vesicle enhanced the stiffness only marginally, by less than 10 %, compared to the P3-shell alone (k = 0.22 N/m; Figure 3.6). More generally, the stiffness values shown in Figure 3.6 exemplify that the stiffness of the composite (0.24 N/m) is well approximated by the sum of the stiffness values of the constituent shells (0.22 N/m + 0.02 N/m). The small enhancement in stiffness was virtually independent of the Poisson ratios of both capsid and membrane (Figure 3.8).

The above modelling exercise provides reasonable predictions about the trends that can be expected based on the experimental AFM shell elastic derived mechanical properties. We have here operated with the P3-shell as a reference system because experimental data for this single-shell system was readily available. Using the above identified stiffness relation, we can now also estimate the Young's modulus of the complete capsid shell from the experimentally determined stiffness values of the Sus1 procapsid and the membrane. The closure of 11 of 12 vertices by additional proteins enhances the elasticity of the Sus1 procapsid shell compared to the P3-shell, whilst a further enhancement of the capsid elasticity by the unique vertex – missing in the Sus1 procapsid – is likely to be marginal. (Figure 3.6: $k_{\text{capsid}} \approx k_{\text{capsid+membrane}} - k_{\text{membrane}}$ = 0.39 N/m – 0.02 N/m = 0.37 N/m. Finally, we arrive at the Young's modulus of the complete capsid shell using $E \approx k$ / 1.65 nm (Figure 3.7C), which gives $E \approx$ 0.22 GPa.

3.3.5. Yield

The presence of the genome and the ensuing particle stiffening had no appreciable effect on the mechanical stability of the virion: yield force and yield strain of wt PRD1 (F_y = 3.0 ± 0.1 nN, ε_y = 17.5 ± 0.8 %; mean ± s.e.m.) and the Sus1 procapsid (F_y = 2.7 ± 0.1 nN, ε_y = 18.1 ± 1.4 %) were similar (Figure 3.9). This is in contrast to other phages, such as phage λ, where the DNA augments both stiffness and mechanical stability (Ivanovska et al., 2007). As for the P3-shell, it was much more sensitive to breakage than wt PRD1 or the Sus1 procapsid (F_y = 0.9 ± 0.1 nN, ε_y = 12.3 ± 0.7 %; Figure 3.9).

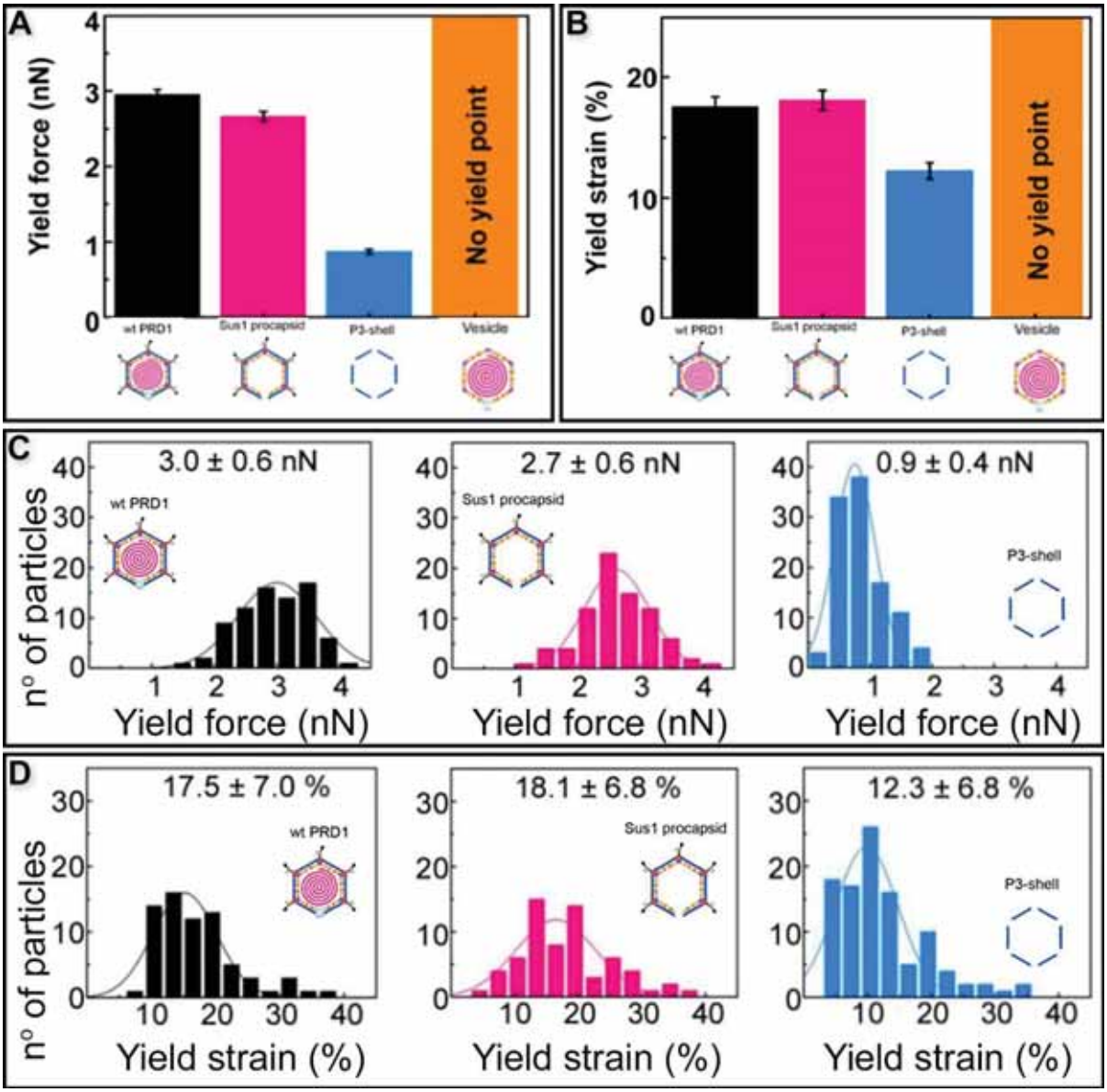

Figure 3.9: Comparison of the yield force (A) and yield strain (B) data for each of the four PRD1-derived particles, reporting mean values and standard error. These values were derived from C and D respectively which shows yield force histograms of the four viral particle types, reporting mean values and standard deviations for each type. (y-axis: number of particles. x-axis: yield force value). For the vesicle, calculation of toughness is not possible because there is no defined yield point.

3.3.6. Toughness

The resistance to material fracture is typically expressed as toughness *T*, here defined as the amount of energy per unit volume that can be absorbed before mechanical failure. To explore how PRD1 vesicle and capsid together influence toughness, we compared the toughness of the PRD1-derived particles: the wt PRD1 particle, the Sus1 procapsid, the P3-shell, and the vesicle. The toughness of PRD1 was estimated to be 2.2×10^5 J/m^3, while the P3-shell ($T = 0.54 \times 10^5$ J/m^3) was more susceptible to mechanical failure than the Sus1 procapsid ($T = 2.1 \times 10^5$ J/m^3; Figure 3.10). That the P3-shell's toughness was ~4-fold less but its stiffness only 2-fold less revealed its rather stiff, brittle nature (Figure 3.10). The P3-shell lattice is held together by the (C-I type and C-II type) interactions established by the GON within each facet and along the facets via the MCPs C-termini and by the P30 proteins (Abrescia et al., 2004) (Figure 3.1). The relative ease of breakage of this lattice might facilitate morphological corrections as the capsomers assemble on the vesicle mould during the procapsid formation. Closing of the icosahedral vertices with the peripentonal capsomers and penton proteins (Figure 3.1) and plugging the unique vertex with the portal complex produces a stable procapsid that can withstand dsDNA translocation powered by the packaging ATPase P9 (Hong et al., 2014).

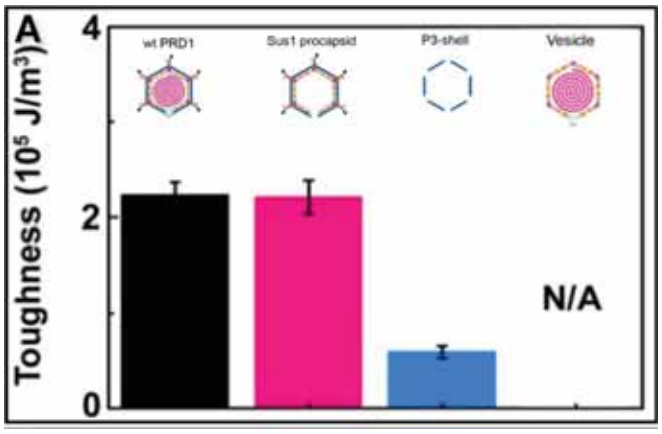

Figure 3.10: Comparison of the calculated toughness value for each of the four PRD1-derived particles, reporting mean values and standard error. These values were calculated using the height and yield force data from Figure 3.9)

Mechanical failure of the PRD1 particles upon indentation was frequently accompanied by the loss of capsomers from the capsid shell (Figure 3.5, insets). In addition, *F*/*z* curves of wt PRD1,

the Sus1 procapsid, and the P3-shell revealed slip events coincident with the occurrence of micro-fractures during force loading likely reflecting local displacements of MCPs (Figure 3.3). While all three particle populations presented a similar density of micro-fractures (average 1.3 per nN of applied compressive force), wt PRD1 and the procapsid withstood more of these fractures before yielding. More generally, the brittle nature of the capsid is not only manifested in the small yield force of the P3-shell but also in the above-mentioned microfractures. The DNA-filled vesicles, on the other hand, did not show a clear yield point and typically recovered their original shape even after strains exceeding 60 %, which indicated they were ductile and very soft (Figure 3.6).

3.3.7. Comparison with studies on other viruses

Comparative analysis with other dsDNA viruses indicates that the toughness of PRD1 is superior to most other dsDNA viruses with comparable capsid organization but lacking the internal membrane, and rivals only adenovirus – a non-membrane-containing virus - which is exceptionally rich in cementing proteins stabilizing the capsid (see Figure 3.11 and Table 1). The toughness of PRD1, 2.2×10^5 J/m^3, is relatively high compared to that reported for other icosahedral dsDNA viruses (see Figure 3.10A, Figure 3.11, and Table 1). Among studied icosahedral dsDNA viruses (Abrescia et al., 2004, Liu et al., 2010, Ortega-Esteban et al., 2013, Reddy et al., 2010) PRD1, together with human adenovirus, is one of the toughest. This analysis also highlights that the PRD1 layered complex of capsid and vesicle relieves the genome from a stabilizing role.

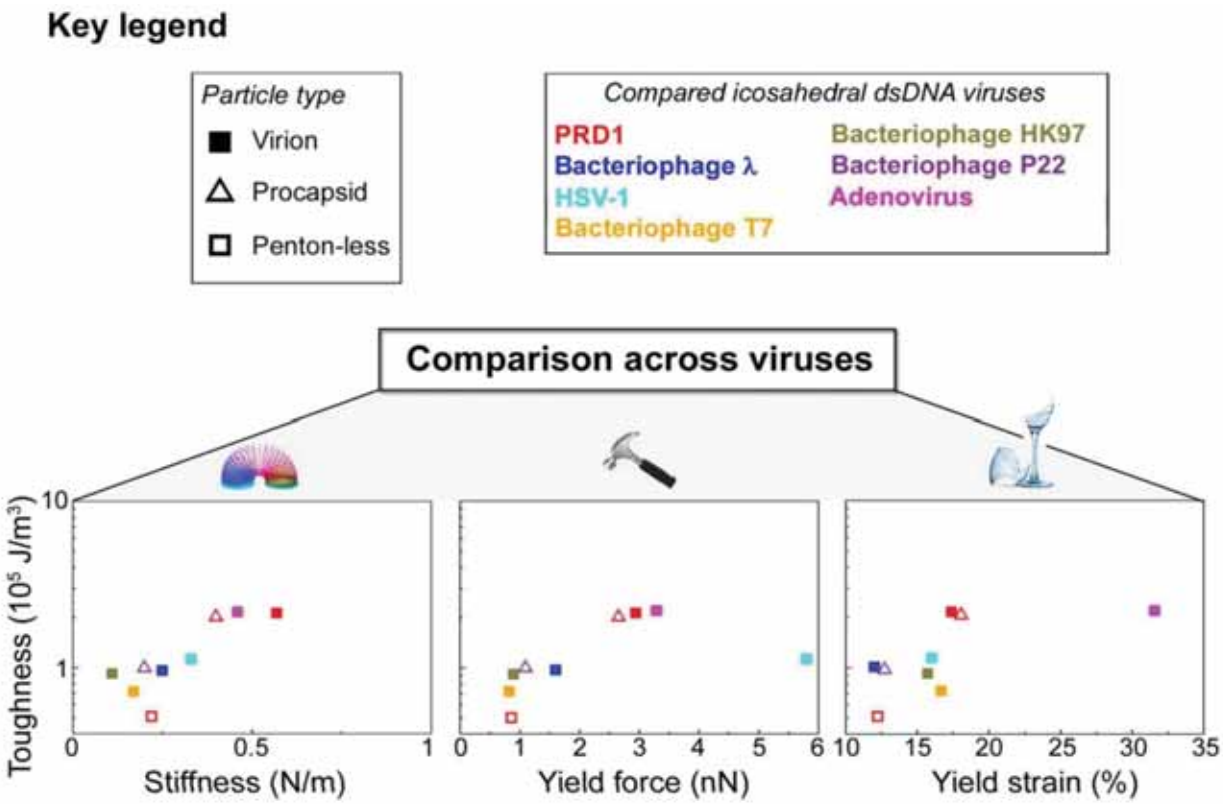

Figure 3.11: PRD1's mechanical properties compared to other dsDNA viruses. Key for the viruses and particle types shown in the other panels (in the case of HSV-1 virion we refer to its nucleocapsid). Comparison across viruses via Ashby plots of toughness (y-axis in log scale) vs. stiffness, yield force and yield strain (x-axis), respectively (see Table 1 for references).

Adenovirus shares a common MCP fold and assembly mechanism with PRD1; however, whilst it lacks a membrane it possesses a complex set of cementing proteins stabilizing the structure - about 300 in total (composed of sixty copies of each of the proteins IIIa, V, VI, VIII and IX) instead of the mere 60 copies of the single protein species P30 guiding the assembly in PRD1 (Abrescia et al., 2004, Reddy and Nemerow, 2014). Taken together, these comparisons highlight that the layered complex of capsid and membrane vesicle relieves the genome from a stabilizing role, and endows PRD1 with remarkably high mechanical stability.

Table 1: Mechanical properties for PRD1 particles from this study and values for other dsDNA viruses taken from the literature. Symbols and colors on the left are described in the key legend in Figure 3.11.

	Virus	h (nm)	k (N/m)	F_y (nN)	ε_y (%)	T (10^5 J/m^3)	E (GPa)	Reference
■	PRD1	67.6	0.57	3	17.5	2.2	--	This study
△	Sus1 procapsid	66.9	0.39	2.7	18.1	2.1	0.24	This study
□	P3-shell	62.8	0.22	0.9	12.3	0.54	0.13	This study
■	HSV-1	125	0.52	5.8	16	1.1	1	(Roos et al., 2009, Sae-Ueng et al., 2014, Liashkovich et al., 2008)
△	Bacteriophage P22 capsid	50	0.19	1.1	12	1	0.2	(Llauro et al., 2016)
■	Bacteriophage λ	63	0.25	1.6	12.7	1	1	(Ivanovska et al., 2007)
■	Adenovirus	95	0.46	3.3	31.6	2.2	--	(Ortega-Esteban et al., 2013)
■	Bacteriophage T7	60	0.17	0.82	16.2	0.7	--	(Hernando-Perez et al., 2014)
■	Bacteriophage HK97	54	0.11	0.9	15.7	0.9	0.6	(Roos et al., 2012)

Previous studies on binary component viral systems – genome encapsulated by a protein shell – have highlighted the role of DNA or RNA in contributing to the capsid stiffness where the mechanical reinforcement is achieved by the genome anchoring the protein shell from the interior (Mateu, 2012). In other cases, such as the HSV-1 nucleocapsid, the stiffness and yield force remain practically the same whether the particle is full packaged or devoid of genome, and stabilizing viral proteins appear to be responsible for this assembly type (Roos et al., 2009, Sae-Ueng et al., 2014). In PRD1, the Sus1 procapsid and the mature particle display similar yield forces whereas the relative increase in stiffness of the wt PRD1 can be attributed to the presence of the DNA that upon genome packaging leads to an expansion of the membrane-vesicle thus increasing the membrane's interactions with the capsid proteins (Hong et al., 2014,

San Martin et al., 2002, Martin et al., 2001, Santos-Perez et al., 2017). The combination of tough, but fragile, protein capsid along with a flexible, inner membrane, helps stabilize the virus particle.

3.3.8. PRD1 as a composite material

Composites have evolved in nature driven by selection for efficient use of materials, adaptability, and multi-functionality. Viruses can be seen as composite biological entities where nucleic acids, proteins and lipids assemble to produce functional particles for infection. We propose that, as in a composite sandwich material (Figure 3.12C), an interfacial protein/polypeptide matrix in PRD1 generates a tight connection that mechanically couples capsid and membrane (Figure 3.12 B). The flexibility of this matrix and possibly also the fluidity of the membrane facilitate the displacement of the two shells relative to each other, and thus assists in maintaining the capsomers in place whilst allowing for the correction of small scale defects in the (re-)assembly process.

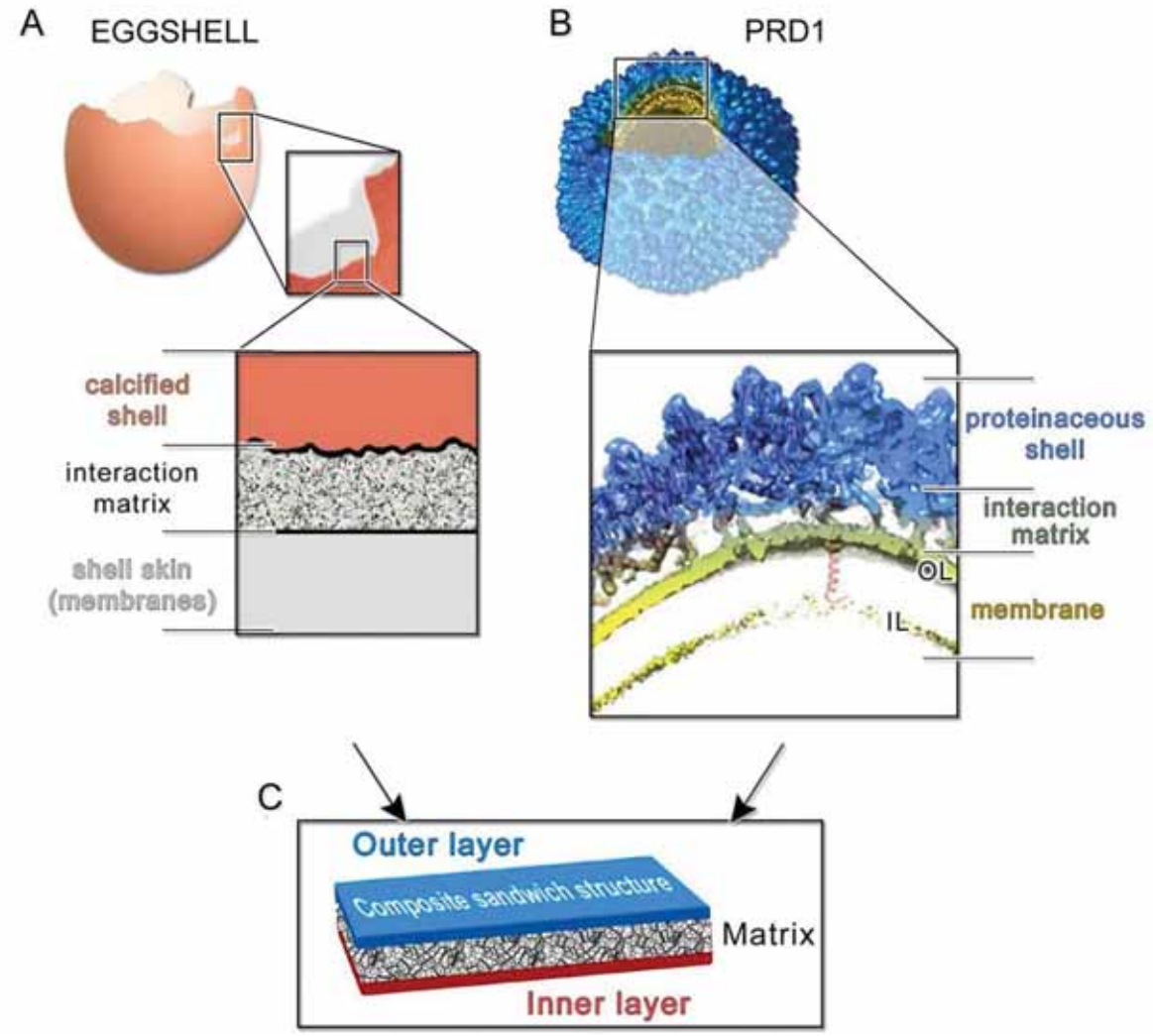

Figure 3.12: (A), Multilayered structure of an avian eggshell; (B), Cryo-electron density of wt PRD1 with an octant removed displayed in Chimera [42] to show the layered/composite structure of the virion with the proteinaceous shell in blue, the membrane-vesicle in yellow-lime (OL: outer leaflet; IL: inner leaflet) and with the horizontal black-lines marking the distinct layers and the interacting matrix region between the capsid and the membrane. As cartoon representation in red fitted in density the P3 MCPs with N-terminal α-helices interacting with the OL and the P16 transmembrane protein crossing the membrane vesicle. The dsDNA has been removed from within the membrane vesicle for clarity; (C), Schematic of a composite sandwich material to which A and B recapitulate.

3.4. CONCLUSIONS

In summary, we here presented the nanomechanical characterization of a proteotypic virus that features a membrane under its capsid. The combination of a stiff, yet brittle, proteinaceous capsid with a soft proteo-lipidic vesicle in PRD1 facilitates multiple stages of the virus life cycle, including virus assembly, mechanical protection for the extracellular virion, and the vesicle-to-tube transformation during DNA ejection (Peralta et al., 2013). From a broader perspective, it appears that the evolution of membrane-containing viruses has yielded, at the nanometer scale, composite properties comparable to those known for macroscopic natural materials, where capsid and vesicle are bonded into a tough composite that protects the integrity of the virus and its genome. Our findings provide both foundational quantitative information and inspiration that can encourage engineering of tough nanoscale devices and particles capable of protecting fragile cargos.

PRD1 virion exhibits mechanics of a composite material for genome protection

PRD1 virion exhibits mechanics of a composite material for genome protection

Chapter 4: Insights into the mechanics and structure of the PRD1 DNA ejection tail tube

PRD1 virion exhibits mechanics of a composite material for genome protection

4. INSIGHTS INTO THE STRUCTURE AND MECHANICS OF THE PRD1 DNA EJECTION TAIL TUBE

This study is still in progress.

Stavros Azinas,[a,b] *Fouzia Bano,* [b] *Dennis H. Bamford,*[c] *Bart Hoogenboom,* [d,e] *Hanna M. Oksanen,* [c] *Ralf P. Richter,*[b,f,g] *Nicola G. A. Abrescia* [a,h]

[a]CIC bioGUNE Derio, Spain; [b]CIC biomaGUNE; San Sebastian, Spain; [c]University of Helsinki, Finland; [d]London Centre for Nanotechnology, London, United Kingdom; [e]Department of Physics and Astronomy, University College London, Gower Street, London WC1E 6BT, United Kingdom; [f]University of Leeds, Leeds, United Kingdom; [g]University Grenoble Alpes-CNRS, France; [h]IKERBASQUE, Basque Foundation for Science, Bilbao, Spain

My contribution: After receiving the purified PRD1 particles, I optimised the PRD1 samples for maximal tube content. Following that, I performed the atomic force microscopy experiments at the London Centre for Nanotechnology, and subsequent AFM data analysis. I also performed sample preparation, data analysis for the cryo-EM data, and data interpretation.

4.1. INTRODUCTION

The vast majority of bacteriophages possess tail structures that serve as delivery systems of genomic material to host targets. These structures, particularly those of *Myoviridae* and *Siphoviridae* phages, have an evolutionary relationship with other cellular biological entities that share the common function of penetrating the bacterial envelope (Ackermann and Kropinski, 2007, Scholl, 2017). The structural similarities between the MCPs of phages and other viruses point to a common evolutionary origin for the proteinaceous heads of tailed dsDNA phages infecting bacteria and archaea, and eukaryotic viruses of the Herpes family (Fokine et al., 2005, Abrescia et al., 2012, Duda et al., 2006). Bacteriophage PRD1, the archetypal member of the *Tectiviridae* family, produces a tube structure after successful orientation and attachment onto the bacterial cell. In PRD1, the tube self-assembles from remodelling of the inner proteo-lipidic vesicle, and serves as pinching/drilling and ejection device respectively of the bacterial cell wall and of the viral genome (Figure 1.3). Due to the observed capability of the PRD1 tube to penetrate the cell wall, there was some evidence that it might possess an ordered structure with a mixed composition of lipids and proteins (Peralta et al., 2013).

Since PRD1 dsDNA must pass through a layer of cell-wall peptidoglycan (Figure 4.1), the PRD1 transglycosylase proteins P7/P14 and protein P32 which are known to be both involved in DNA entry (Figure 1.2, right), and exist in the membrane vesicle, most likely take active role in the formation of the DNA ejection tube (Grahn et al., 2002a, Grahn et al., 2002b). The ability of PRD1 tube to drill holes in the cell wall of *Salmonella enterica* and *E. coli* has led us to consider this tube as potentially an alternative nanotool for dealing with bacterial infections.

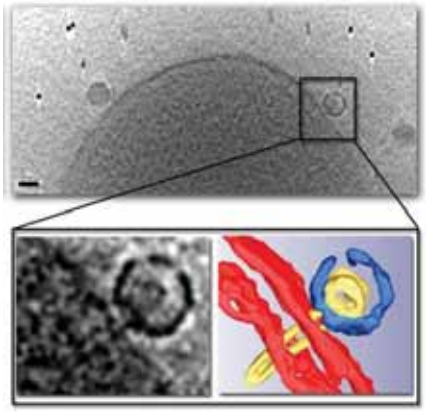

Figure 4.1: Tomographic slice of an E. coli cell infected by wt PRD1 (~30 min p.i.). Scale bar, 50 nm. (Top) Here, we can see an almost empty particle, outlined in a black line. (Bottom) Tomographic slice showing a particle with a "map-pin" shape vesicle and full-length tube penetrating the cell envelope (bottom-left) and corresponding segmentation (bottom-right). The tube is seen to be almost perpendicular, and density is seen drilling the cellular envelope.

Indeed, bacteriophages have been considered as natural weapons for combatting the spread of bacteria. Under the threat of pathogenic bacteria resistant to a variety of currently available antibiotics, a lot of effort has been put in place to find innovative ways to combat the spread of disease (Hammerum et al., 2010). The enormous demand has triggered worldwide efforts in developing novel bacteriocides. Bacteriophages, bacterial cell wall hydrolases (BCWH), and antimicrobial peptides (AMP) are among the most promising candidates (Parisien et al., 2008). Here, by determining the three-dimensional structure of the PRD1 genome ejection nanotube by cryo-EM and its mechanical properties (stiffness, resistance to nanoindentations) by AFM we unravel the self-assembly mechanism of the proteo-lipidic functional to bacterial infection.

4.2. MATERIALS AND METHODS

4.2.1. Virus production and purification

wt PRD1 virus particles were produced and purified as described in section 3.2.1.

4.2.2. Cryo-EM analysis

4.2.2.1. Tube formation and preliminary visualization by negative stain EM technique

wt PRD1 virus particles were kept at 4 °C for 4-6 weeks from the day of purification. This was established via negative staining (Figure 4.2) and verified by cryo-EM as the optimum period where sufficient amount of tubes was formed and the least amount of PRD1 particle degradation was observed.

For negative-stain imaging, the sample was stained using 0.75% uranyl formate solution in water using an adapted procedure (Gowen et al., 2003). Briefly, we applied 20 µl of sample (at ~1 mg/ml) to a 400 mesh R2/1 holey carbon copper grid (Quantifoil Micro Tools GmbH, Jena, Germany), and after washing 3 times using Hepes buffer (Section 3.2.3), the sample was stained for 1 minute in 30 µl of uranyl formate before removing the excess of liquid by blotting with filter paper. Images were then collected using a JEOL JEM-1230 transmission electron microscope operated at 120 kV under low-dose conditions at room temperature and at a nominal magnification of 25000 by direct recording on a Orius SC1000 CCD camera (Gatan Inc.).

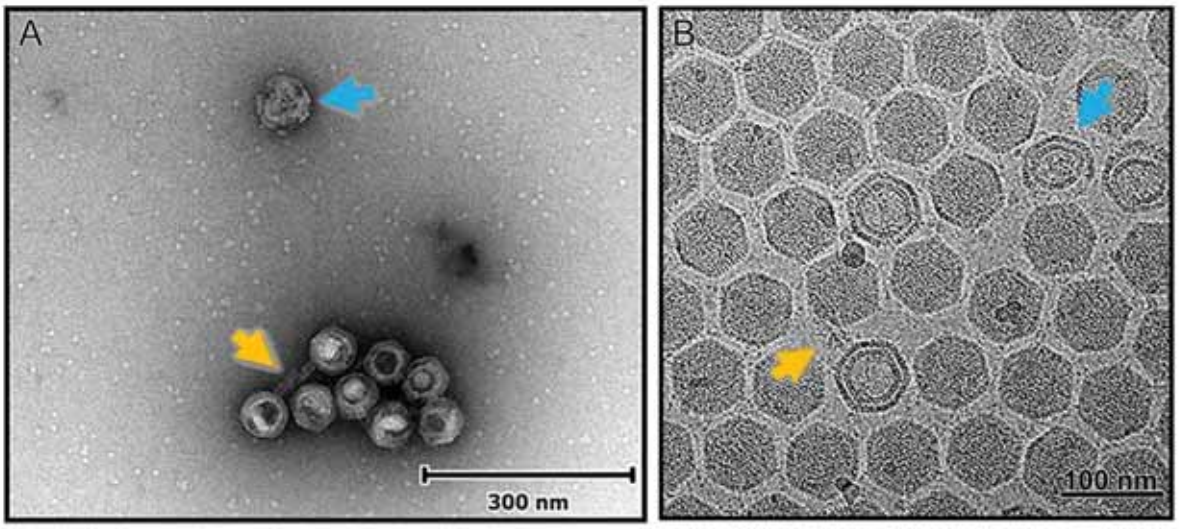

Figure 4.2: (A) Negative staining of a 5-week aged wt PRD1 sample, visualized using negative stain EM. PRD1 tubes are visible in the sample (orange arrow, bottom half of the image), as well as a particle starting to deteriorate (blue arrow, top half of the image). This can be observed by the fractured nature of the outer protein capsid, as well as the loss of the well-defined icosahedral seen on other particles. (B) Cryo-EM image of similarly aged PRD1 sample. A tube is also visible (orange arrow) as well as a particle starting to deteriorate (blue arrow). The rest of the particles seem to contain the genomic content..

4.2.2.2. Cryo-EM data acquisition and analysis

The wt virus PRD1 sample (3 µL, 0.5-1 µg/µL) was applied to Quantifoil R2/2 holey carbon grids (Quantifoil Micro Tools GmbH, Jena, Germany), which were previously plasma cleaned, and vitrified in a FEI vitrobot Mark III. Some of the vitrified grids were checked for quality control using the in-house JEOL 2200FS 200 kV electron microscope and triaged for shipping and data collection to large EM facilities in Europe equipped with Titan Krios 300 kV electron microscopes and direct detection cameras. Two different datasets were collected respectively at eBIC-Diamond (UK) and at CEITEC (Czech Republic). In the first data collection ~4200 movies were acquired using K2 direct electron detector, 18 frames per movie at 1.07 Å per pixel, with a range of defocuses of -4200 to -30500 Å. The second data set was collected at CEITEC using a Falcon II direct electron detector collecting ~8000 movies (at 16 frames per movie) at 1.07 Å per pixel, with a range of defocuses of -5500 to -29500 Å. The total electron dose suffered was 49 $e^{-}/Å^{2}$ per micrograph movie for the micrographs collected at CEITEC.

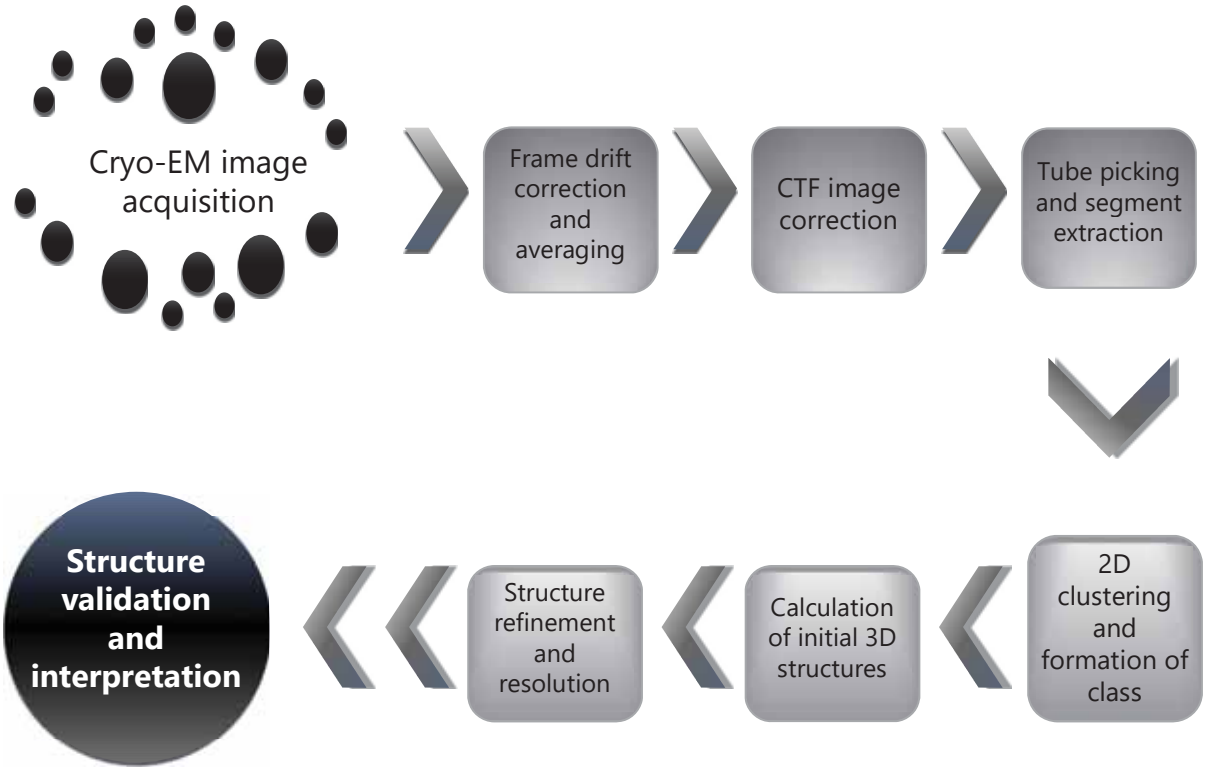

Figure 4.3: Diagram of the steps taken to determine the three-dimensional structure of PRD1 tube. From initial "raw" data to the final solved structure, each step plays a crucial role in acquiring an interpretable map of the PRD1 tube.

4.2.2.3. Image processing and 2D longitudinal view tube classification

Frames from each movie were aligned and summed to produce drift-corrected micrographs using MOTIONCORR1 software and the contrast transfer function estimated using CTFFIND3 software (Li et al., 2013, Mindell and Grigorieff, 2003). Micrographs showing signs of astigmatism or significant drift were discarded. A total number of 1850 lateral view tubes where manually selected using e2helixboxer program within EMAN2 software, from approximately 1500 micrographs (Tang et al., 2007). The relatively low number was due to a combination of low tube formation (similar to Figure 4.2B), overlapping tubes, and thick ice-covered micrographs which were not suitable for single particle analysis. Classifications and 3D reconstruction were determined with RELION 2.1 software, following the protocol procedure analytically described in the following sections (He and Scheres, 2017).

Due to the relatively low number and complexity of automatically picking the tubes formed by PRD1, we inspected the individual micrographs. We selected tubes that were not overlapping

other tubes or particles, and had no debris on, or very close, to them. Following selection, we performed a reference-free two-dimensional (2D) classification of the lateral view of the tube, in order to identify homogeneous subsets, and/or the presence of a regular pattern. A regularization value of $T = 2$ was used on segments that were extracted using varying inter-box distances; 250 Å (half the maximum tube length observed experimentally), 100 Å, 50 Å, 25 Å, 11 Å, and 5 Å. We also experimented with both lower and higher values of T which determines the relative weight between experimental data and priors, but no improvement was seen. 2D classifications with T values as high as 10 yielded 2D class averages with no further structural enhancement but rather, due possibly to overfitting, lower quality Fourier transforms. The final inter-box distance was selected after extracting same-sized boxes but with varying distances and examining whether the prominent repetitive unit distance remained the same or was due to segment bias.

Overlapping boxes, 300 pixels long with 11 Å shift (larger than the observed repetitive striation spacing, as observed in Figure 4.10) between adjacent boxes were extracted from these tubes, yielding a total of 34000 segments. In all cases, the repetitive pattern of 'striation' distance was conserved consistently (just like it appeared in various subclasses in Figure 4.7), and inter-box distance of 11 Å was selected in order to produce most segments as possible during extraction. The data were subjected to rounds of 2D classifications with 5 classes. The final obtained major 2D class was composed of a total of 23000 segments from 835 micrographs, which were further used to initialize the three-dimensional (3D) reconstruction of the tube.

4.2.2.4. 2D classification of orthogonal views of the PRD1 tube

In addition to the longitudinal view tube analysis, a total of 59 "top view" tubes appearing perpendicular to the surface were also identified during the data collection. These were extracted as boxes of 300 × 300 pixels, and then a reference-free, 6-class, 2D classification was performed. The regularization parameter T value of 2 was used. The two major classes were

selected, and another reference-free 2D classification was performed, further cleaning up our limited dataset. The final major class that emerged comprised of 32 views, and was examined both visually, as well as using rotational analysis software [SCIPION (de la Rosa-Trevin et al., 2016)] to determine the point symmetry of the tube.

4.2.2.5. Preliminary three-dimensional reconstruction

Using the best 2D class dataset, a rectangular mask was also applied, 130 Å outer width and 10 Å inner width. The mask diameter was defined based on the measured diameter of the tube, as established from 2D classification. Selected segments were then subjected to 3D classification in Relion. An initial model of a simple cylinder (Figure 4.4) was created using relion_reconstruct and used as a template for the initial 3D classification, after filtering it to 40 Å. To check variation between segments, a 3D classification into 2 classes was performed and provided class averages of 70% and 30%. To avoid biasing the classification due to the relatively weak signal in the segments, only information up to 8 Å resolution was included during the classification. Full-CTF correction was performed.

3D classification was repeated using the same set of data, and using the resulting model from the majority class of the initial classification, low-pass filtered at 40 Å (and later tasted also at 60 Å), to see whether we could improve the classes (Figure 4.5).

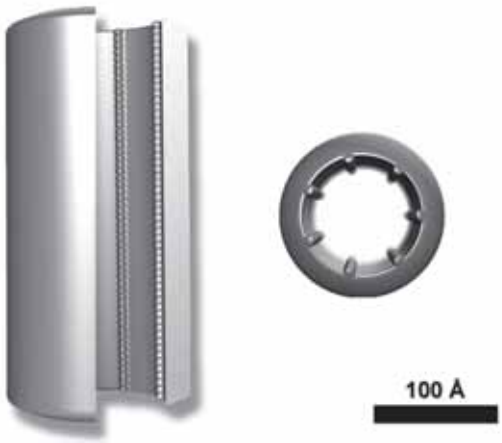

Figure 4.4: Side view of the featureless cylinder with a C7 inner symmetry of small (5 Å) balls repeating every 5 Å, alongside the top view.

In parallel, the same 2D classified segments were subjected to a 3D refinement, which generates two independent half-sets of the data. Like the 3D classification, the same featureless cylinder was used for the first refinement, then the process was repeated using the resulting converged model in another round of refinement. A diagram showing the methodology followed is shown in the figure below.

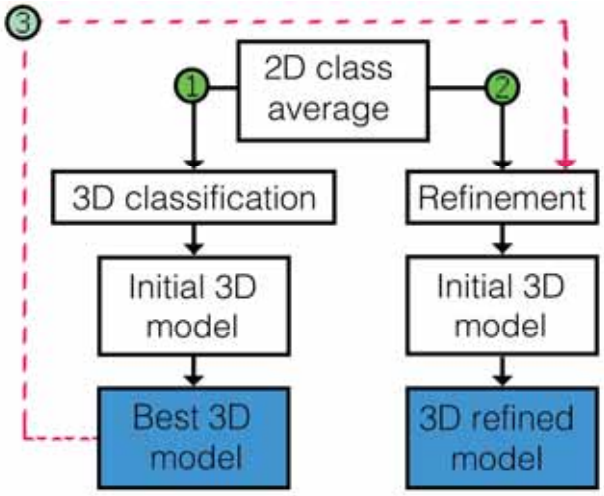

Figure 4.5: Workflow of methodological steps followed so far in the determination of the 3D structure of the tube. After obtaining the optimal 2D class average, the classified data were used in parallel runs of 3D classification ① and Refinement ② using the cylinder from Figure 4.4 as initial model. We obtained 3D models that were then used to re-run both 3D classification and Refinement, leading to two independent but comparable models. ③ Next, we will also submit to refinement the 3D classified map.

The refined model, was post-processed, using a B-factor of -100, as overfitting of high-frequency noise was observed at lower B-factors (>-200). The final resolution of the structure was assessed by Fourier shell correlation (threshold 0.143), and it was calculated at 7.2 Å. The resolution of the model obtained from 3D classification was not assessed.

4.2.3. AFM analysis

4.2.3.1. Surface preparation and immobilization of PRD1 tubes

The surface and immobilization technique used was previously described in section 3.2.3. Virus particles were allowed to adhere to APTES functionalized mica for 30 min, and excess particles were removed by washing with buffer.

4.2.3.2. AFM Imaging and nano-indentation

PRD1 particles and tubes were found to attach to the prepared mica surfaces and could be readily visualized by AFM. Imaging and nanoindentation measurements were carried out using a MultiMode 8 AFM with a Nanoscope V controller (Bruker, CA, USA) at room temperature in Hepes buffer (10 mM HEPES, pH 7.4, 150 mM NaCl, 2 mM $MgCl_2$). wt PRD1 particles were analysed with sharpened triangular Si_3N_4 cantilevers with a nominal spring constant of 0.7 N/m (ScanAsyst-Liquid; Bruker). The real spring constants of the cantilevers were measured using the thermal noise method as implemented in the NanoScope software and were found to be close to the nominal values. Imaging was performed in Peak Force Tapping mode, with a typical tapping amplitude of 40 nm. The peak force was usually 80 pN. Under these conditions, the image quality was sufficient to reliably identify the orientation of virus particles and visualize the tubes, and in general intact PRD1 particles did not degrade or break upon repeated imaging. Individual tubes lacking the protein capsid were also observed occasionally. Images were plane fitted when required, using Gwyddion software (http://gwyddion.net/) without application of noise filtering or sharpening.

Nano-indentation measurements were performed at individually selected tubes using the "point-and-shoot" function within the NanoScope software. Briefly, the area of interest was first imaged to localize eligible tubes; the "point-and-shoot" function was then activated and force curves were taken at the tube centre, but away from any visible "ring" structures (as seen later in Figure 4.17); subsequently, the area was imaged once more to verify successful nano-indentation, where possible.

The accuracy of localization of the tube centre was found to be limited by piezo drifts and estimated to be within 2-4 nm between image acquisition time and nano-indentation. This was determined by acquiring a series of force curves of the adjacent area to ensure nanoindentation. Force vs. distance (F/z) curves were acquired at a constant approach velocity of 200 nm/s. The approach and retract distances were 100 nm, corresponding to a total time of 1 s per complete approach and retract cycle. The maximal load was 0.75 nN. F/z curves were analysed using the NanoScope software.

4.2.4. Determination of yield point and stiffness

After first contact between the AFM probe and a PRD1 tube at the contact point z_c, the initial monotonous force (compression) was followed by either an extended and steep drop (fracture; arrow in Figure 4.6A), or by various typically minor, compression and fracture phases (arrows in Figure 4.6B).

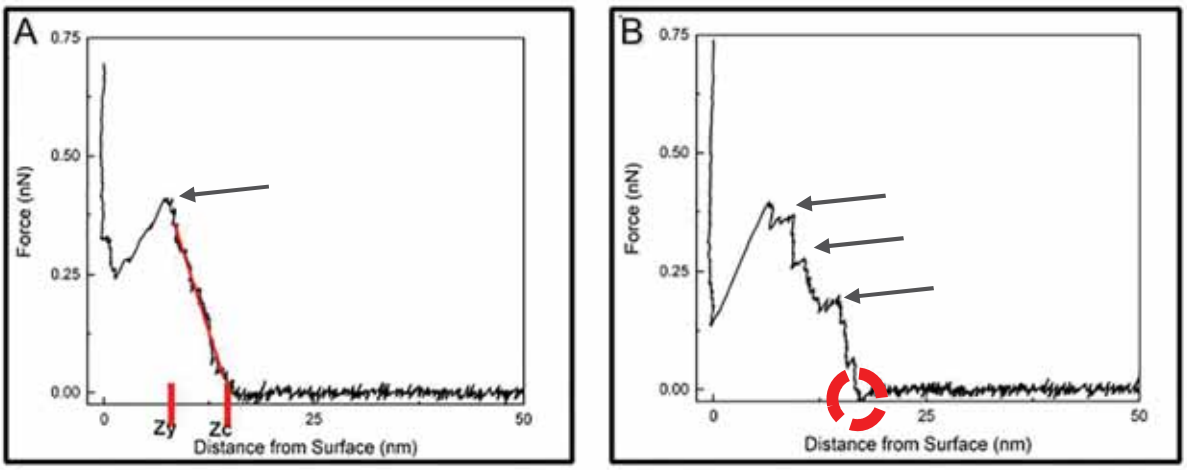

Figure 4.6: Typical force curve profiles obtained for tube analysis. Initial onset of forces was roughly 17 nm from hard-wall contact. Arrows mark fracture phases, while the red circle indicates a minor attractive force prior to indentation, as it was observed in some cases.

Neglecting the lowest forces ($F < 30$ pN), we found that the initial part of the first compression phase for wt PRD1 tube, in general, could be approximated by a straight line. The particle stiffness k was determined from the slope in the initial compression phase, i.e., the slope up to the force at which the first slip or the fracture occurred. The onset of the first drop, defined as

the yield point z_y, could correspond to the yield force (where $F_y = F(z_y)$, however as not all tubes exhibited the same behavior, as well as the fact that there was no visible tube damage between intentations in the majority of the cases (90%), we cannot confidently differentiate the nature of breakage based on nanoindentation characteristics alone.

In any case, linear fits were not taken in consideration if the onset of force did not start between around 15 ± 3 nm from hard-wall contact; the height range was selected based on the diameter of the PRD1 tube (as determined by cryo-EM, *vide infra*) and also considering that the roughness of the APTES modified mica may add a few nm to the effective height. The stiffness was not quantified if the first slip occurred below 100 pN to avoid the large uncertainties associated with fitting a line to a small data set.

To further establish the validity of our measurements, we performed a series of consecutive nanoindentations on tubes that were sufficiently solitary yet still attached on a PRD1 virion. Ten nanoindentations (across the line in Figure 4.20A) with 10 nm distance between them were performed, and a consecutive image was collected following the nanoindentations.

4.3. RESULTS

4.3.1. Cryo-EM characterization of the PRD1's DNA-ejection tube

4.3.1.1. PRD1's DNA-ejection tube is structured

By using cryo-EM we have structurally characterized the PRD1 proteo-lipidic tube used for cell infection and viral DNA ejection. As there is no in vitro triggering mechanism for synchronous formation of the tube, ageing of virions at 4 °C for about 4 weeks led to the appearance of particles with tube. Initial 2D classifications using extracted segments with an inter-box distance of 250 Å revealed a repetitive motif of ~10 Å. This helped us further reduce the inter-box distance, and therefore increase the number of segments obtained from the initially selected tubes. Segments extracted from boxes with an inter-box distance of 11 Å were aligned and classified in 2D (Figure 4.7) in RELION (He and Scheres, 2017). The Fourier transform for this major class was then obtained and was analysed further (discussed below).

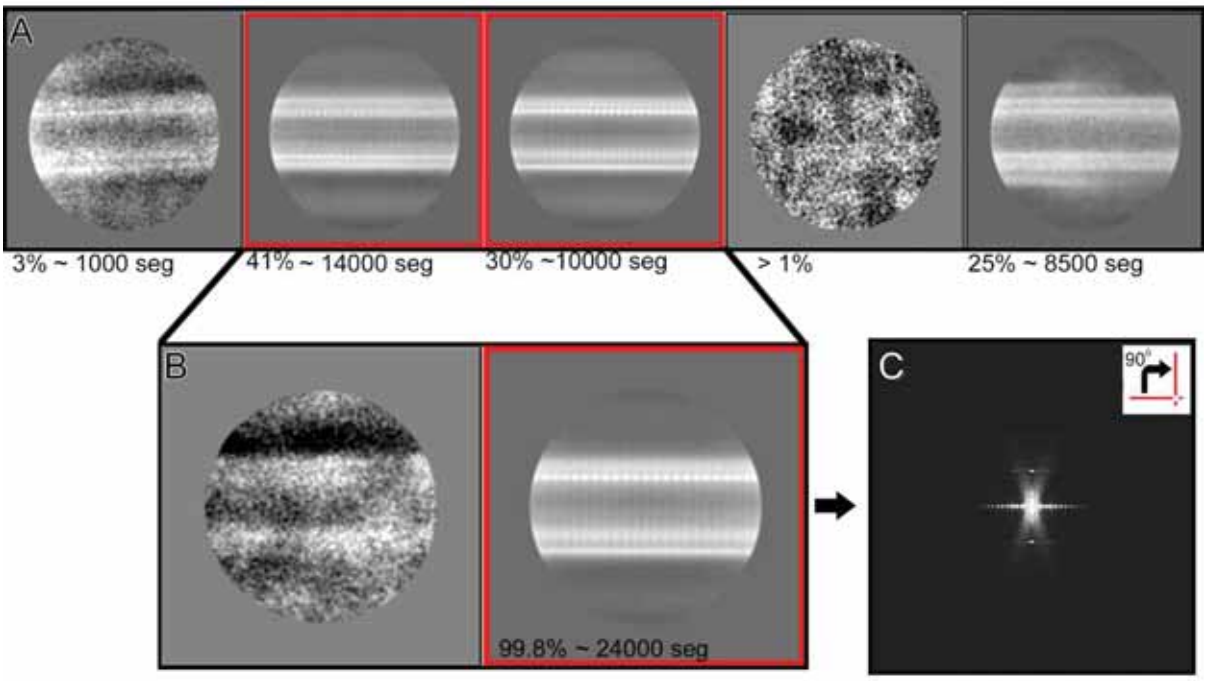

Figure 4.7: 2D classification of 34k segments. (A) When constrained to 5 possible classes, the classification resulted in 2 major classes (red square) (~70%) that were then joined together and reclassified using a constraint of 2 classes (B) resulting in one major class of 99.8% (red square). The rotated Fourier transform of the major class average (C) revealed information regarding possible symmetry of the tube as explained in Figure 4.11.

4.3.1.2. Top view analysis reveals 7-fold symmetry

In order to grasp further information regarding the structure of the tube, we classified the tubes with views perpendicular to the surface. This allowed us to identify the point-symmetry displayed by our system in this orientation. After two rounds of 2D classification, a major class suggested a 7-fold symmetry (Figure 4.8). Furthermore, we observed the presence of a double-layer that was in line with the side-view data. Rotational analysis on the resulting major class (84% - 38 views) was performed, and revealed a likely 7-point symmetry (Figure 4.9). In contrast 3-point and 6-point harmonics were not prominent, indicating that these symmetries are unlikely to characterize the PRD1 tube.

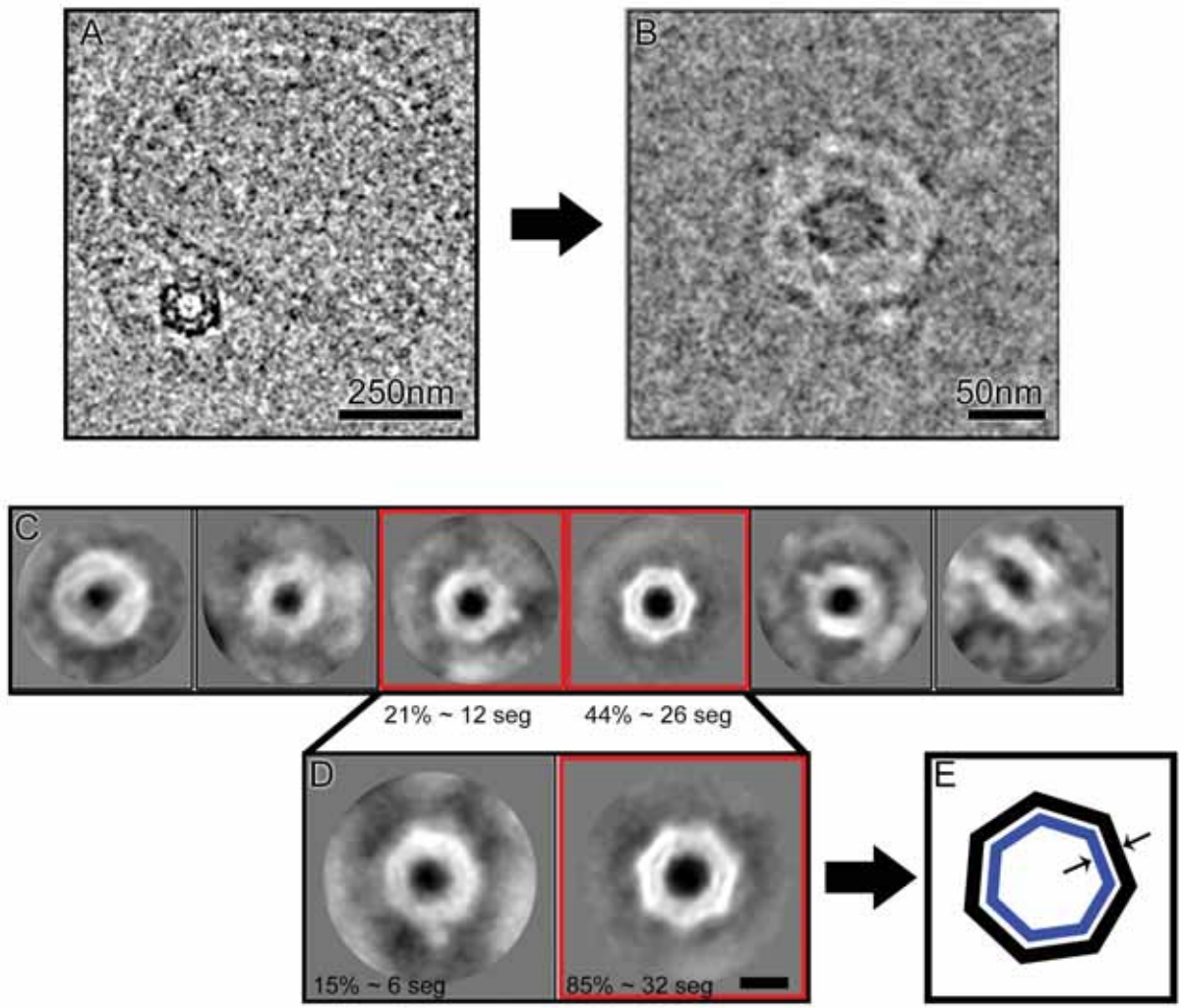

Figure 4.8: Selection of top views, send to classification. (A) From individual micrographs, we identified tubes that appeared to be close to perpendicular to our view. (B) Boxes of 300 × 300 pixels were extracted from these micrographs. (C) 10 class 2D classification of a total of 59 extracted "views" filled 6 classes, and the two most populated (red boxes; 21% (left) and 44% (right)- 38 views in total) were re-classified (D) where the majority class (red box; 85% - 32 top views) was selected for further analysis (Scale bar: 50 Å). The double layered nature of the tube is visible, with the distance between the two layers estimated, based on brightness profile, at ~25 Å. (E) Schematic of the 2D top view average showing the outer and inner layer as seen in (D).

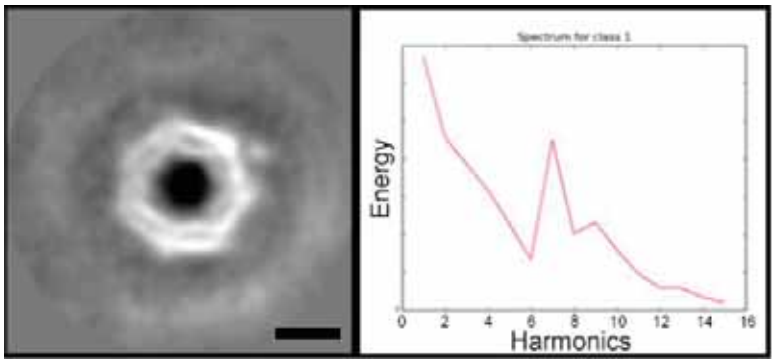

Figure 4.9: Top views rotational analysis (scale bar: 5 nm). Analysis of the harmonic energy revealed a strong peak at 7-fold symmetry, confirming both visually and experimentally our hypothesis.

4.3.1.3. Side-view analysis

The 2D classification results of the longitudinal views shed further light on the "fine" structure of the DNA ejection tube. As shown in Figure 4.10, a double-layer is also visible. Measuring from the outer, denser, and less defined layer, the diameter of the tube is ~110 Å, while the tube diameter from the inner well-structured layer is ~85 Å. This might correspond to a 25-30 Å thick lipid membrane, fenestrated by the tube-forming protein.

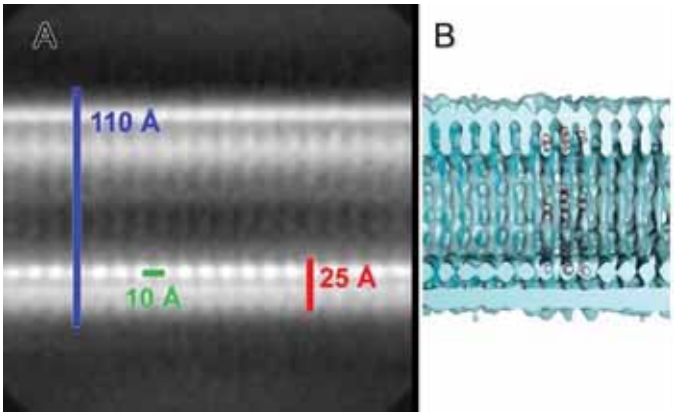

Figure 4.10: (A) Distances based on the 2D class average. The overall diameter of the tube is 110 Å, with the suspected lipid membrane roughly at 25 Å, and the repetative unit at approximately 10 Å. Due to a 7-fold symmetry, the bottom layer most probably corresponds to the perpendicular to the view double-layer, while the top layer appears wider and less defined due to the orientation of the layer in 2D. (B) 3D density of the tube (derived from a 3D classification) cut in half and oriented in a similar manner for visual comparison. The outer leaflet is not as well defined as the inner leaflet, where helices could be fitted.

4.3.1.4. Fourier transform analysis reveals that the tube is not helical

Due to the lack of any previous information regarding the possible symmetry (either a simple rotational and/or helical) of the PRD1 tube – or any related system, we had to determine from scratch its 3D structure. The longitudinal view of the tube suggests the presence of a repeating pattern every ~10 Å, while analysis of the orthogonal views of the tubes indicated a 7-fold symmetry. Fourier transform analysis of 2D class averages of the longitudinal views suggested that the tube might not possess a helical symmetry due to the lack of the distinctive X pattern shape resulting from the convolution of a repetitive-unit with a helical shape (Figure 4.11D) (Note that the moiré effect in the same image is a resulting artefact due to resolution limits and fine noise leading to the observed pattern). Instead, we observed distinct repeating "diffraction" spots at only one detected layer line, equidistant from the equator at a distance of 9.68 Å corresponding to the repeating unit.

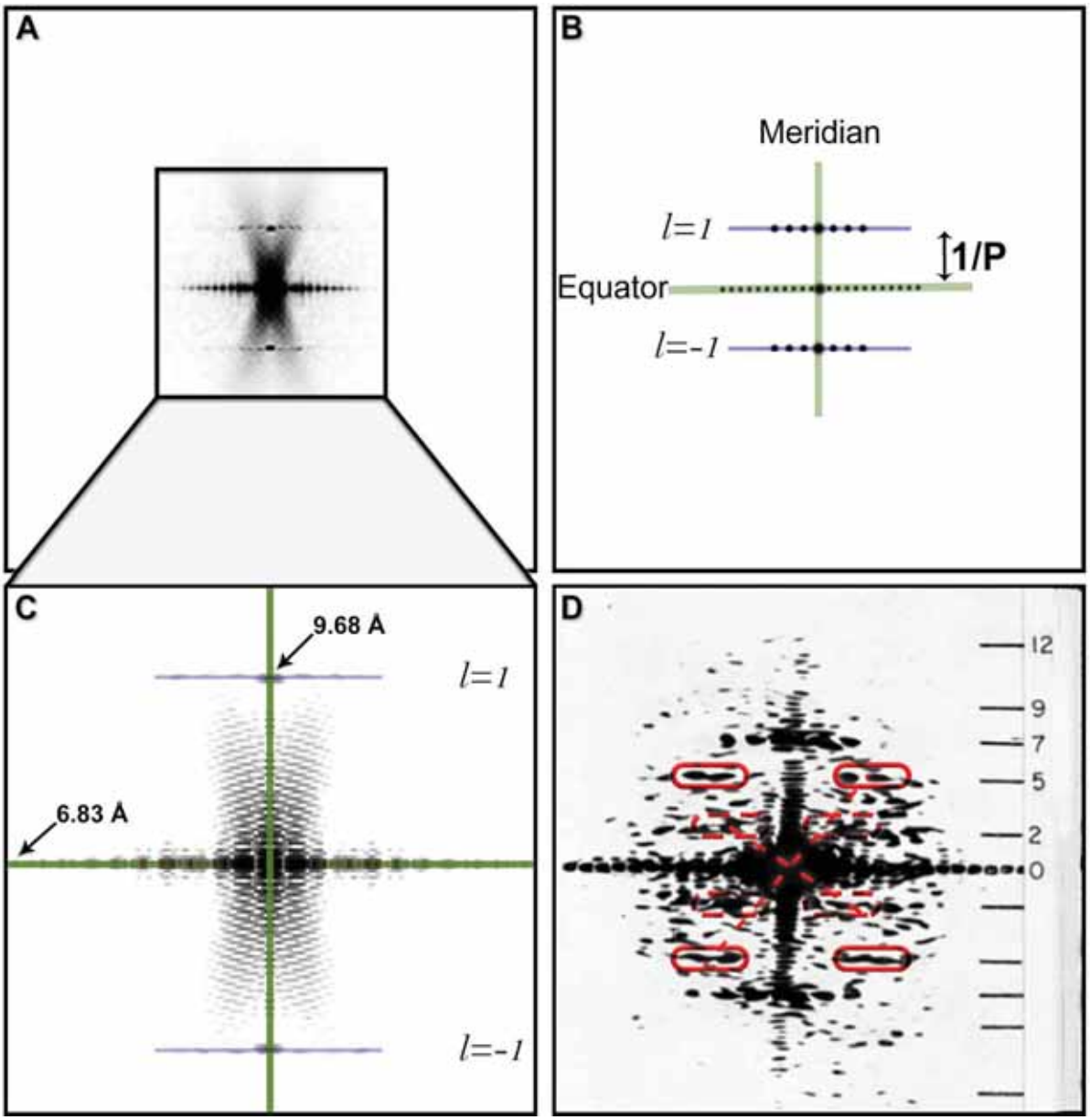

Figure 4.11: (A) Fourier transform pattern of the most populated 2D class average (from Figure 4.7B) and schematic diagram (B) of the observed pattern. (C) Shows a zoom into the central section, revealing the major layer lines, as well the lack of any interspace pattern. The distance from the equator to the first layer line marks the inverse rise of the repeating unit, while spots deviating from the centre correspond to features regarding the width of the tube. Maximum meridian resolution is at 9.68 Å corresponding to the spacing distance of the repeatitive unit along the tube axis, while equator is at 6.83 Å corresponding to maximum resolved resolution. (D) Optical diffraction patterns obtained from electron microscope images of T4 bacteriophage tube structures from the historic paper of (Amos and Klug, 1975). The X-shaped diffraction pattern can be observed (red circles), as well the extensive layer lines, which are characteristic for helical symmetry and clearly distinct from the pattern for the PRD1 tube.

4.3.1.5. Preliminary 3D structure of the PRD1's tube

The resulting structures from both parallel runs (see Methods and Figure 4.5) of 3D refinement (Figure 4.12A), and 3D classification (Figure 4.12B) converged to very similar structures, both

confirming that the internal structure of the tube is well organised. The particular tubular form of the density denoting the inside wall of the tail tube (~7 Å) would correspond with the presence of a protein with prominent alpha-helices (Figure 4.12 and Figure 4.13). We can see that each repeating layer has conserved features, and no helical twist is visible. The outer leaflet, coinciding with the 2D class data, is also visible. Viewing the structure from the top (Figure 4.13B) we can see similarity with the 2D top view classification results (*Figure 4.8*).

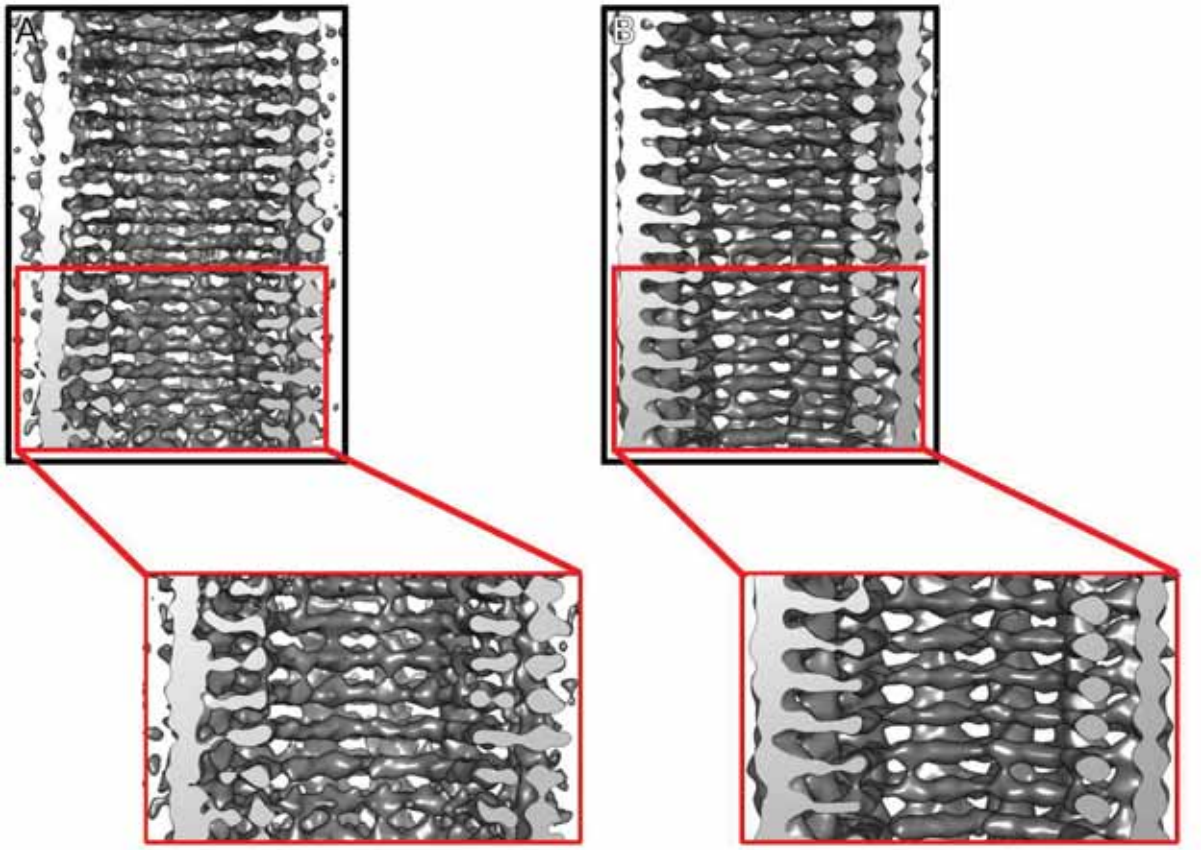

Figure 4.12: Resulting structures from (A) post-processing of a 3D refinement map and (B) the map from 3D classification. The insets show the central part of the tube. The "sausage-like" features orderly lining the inside of the tube are attributed to alpha helices. The outer layer appears less ordered, and is attributed to a lipid layer. Both structures are viewed at same σ-value of 3.5.

We used the 3D refined structure to qualitatelively fit some alpha-helices generated in silico, and built a possible model of a protein that could form the heptameric repeating unit, based on the density map (Figure 4.13).

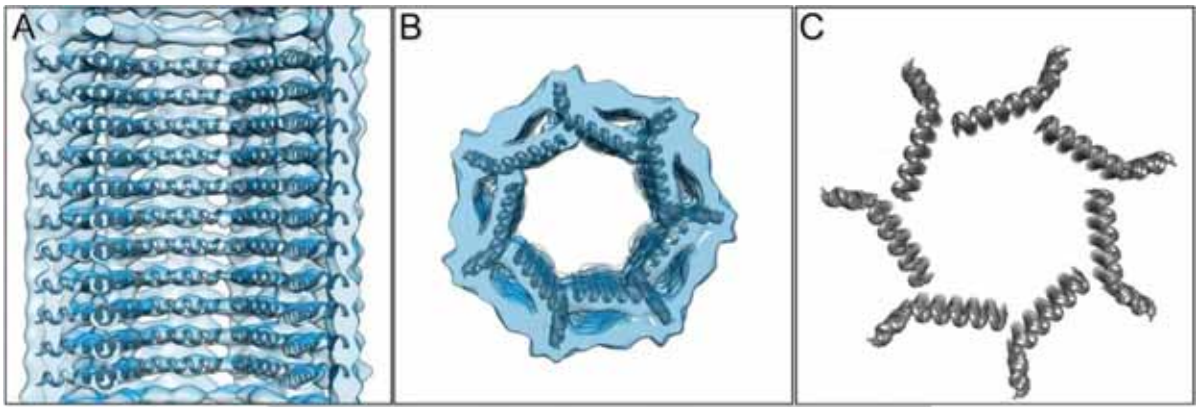

Figure 4.13: Density map of Figure 4.12B, showing manually-fitted alpha-helices within the density. (A) Central side-view section, where we observe that the diameter of these alpha-helices corresponds with the backbone width of the observed densities. (B) Top view of the same map, while (C) shows the possible protein conformation that was fitted based on the density and using generated alpha helices in CHIMERA.

The resolution of the currently post-processed map of the refined structure was estimated using the Fourier shell correlation (FSC) method, at a threshold of 0.143 (Figure 4.14). This revealed a resolution of 7.2 Å, which is close to the experimental value of 6.8 Å obtained from the optical diffraction of the 2D class (Figure 4.10C).

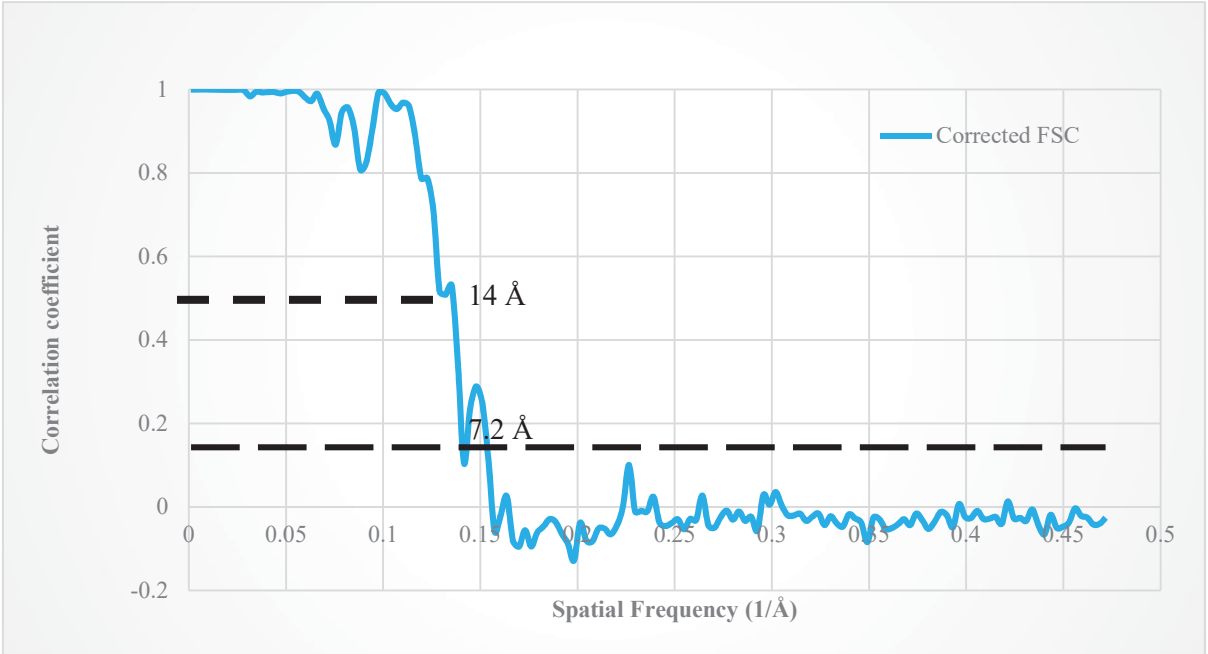

Figure 4.14: Corrected Fourier shell correlation (FSC) calculated between fully independent half data sets (gold standard), of the final cryoEM map. The FSC thresholds of 0.143 for the cryoEM data estimate the global resolution at 7.2 Å., while for FSC threshold of 0.5, the resolution is estimated at 14 Å.

4.3.1.6. Comparison of experimentally observed and model-derived fourier transform

To assess whether the solved 3D structure is accurate, we compared the Fourier transforms of the best 2D class-average of experimental 2D cryo-images (Figure 4.7C) and that obtained by the sum of all frames of our 3D average of the solved structure. The comparison between the two power spectra shows that there are strong similarities between the "real" data and our reconstructed model (Figure 4.15). The layer lines are equidistant from the equator and the data spots are appearing also to have the same distances. Furthermore, the highest visible Fourier transform spot, corresponding to the resolution limit of our map, closely agrees with the 2D class average Fourier transform, which means there is no overfitting of high-frequency noise or extrapolation of data resulting to an overestimated resolution.

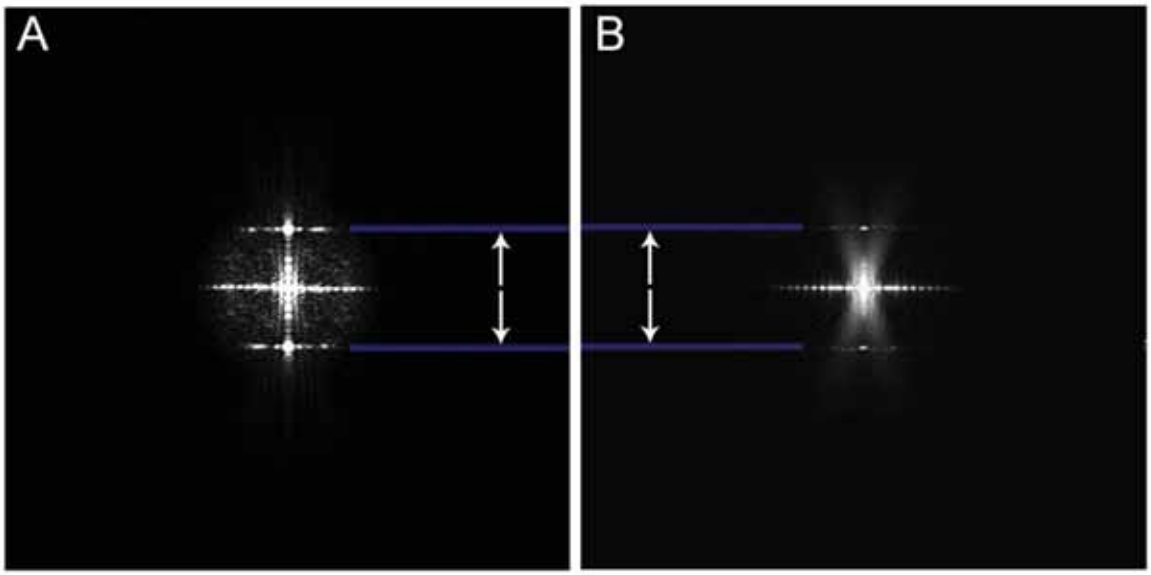

Figure 4.15: Fourier transforms of (A) the final structure of the PRD1 tube and (B) the 2D class average. The layer lines (blue) have the same distance from the equator, just as the distance between the distinct spots along the equator is conserved.

4.3.2. AFM characterization of PRD1's DNA-ejection tubes

4.3.2.1. Structure of PRD1's tubes as imaged by AFM

Tubes protruding from both intact and damaged particles were observed in the sample (Figure 4.16). Isolated tubes lying flat on the surface were also observed (Figure 4.17), in some cases

along with a planar patch of about 4 nm height which is likely a membrane patch results from the rupture of a vesicle. The diameter of the tube was found via AFM to be ~12 nm, while in some cases a characteristic ring of ~7 nm in diameter was observed (Figure 4.17), as previously seen via cryo-EM by (Peralta et al., 2013), and possibly corresponding to a portal or a conjunction of packaging proteins. On already degraded particles, consecutive imaging (following a nanoindentation of the protruding tube) lead to gradual further deterioration (Figure 4.18), and a few particles were also found to be displaced or detach from the surface (Figure 4.18), similar to observations in Chapter 2.

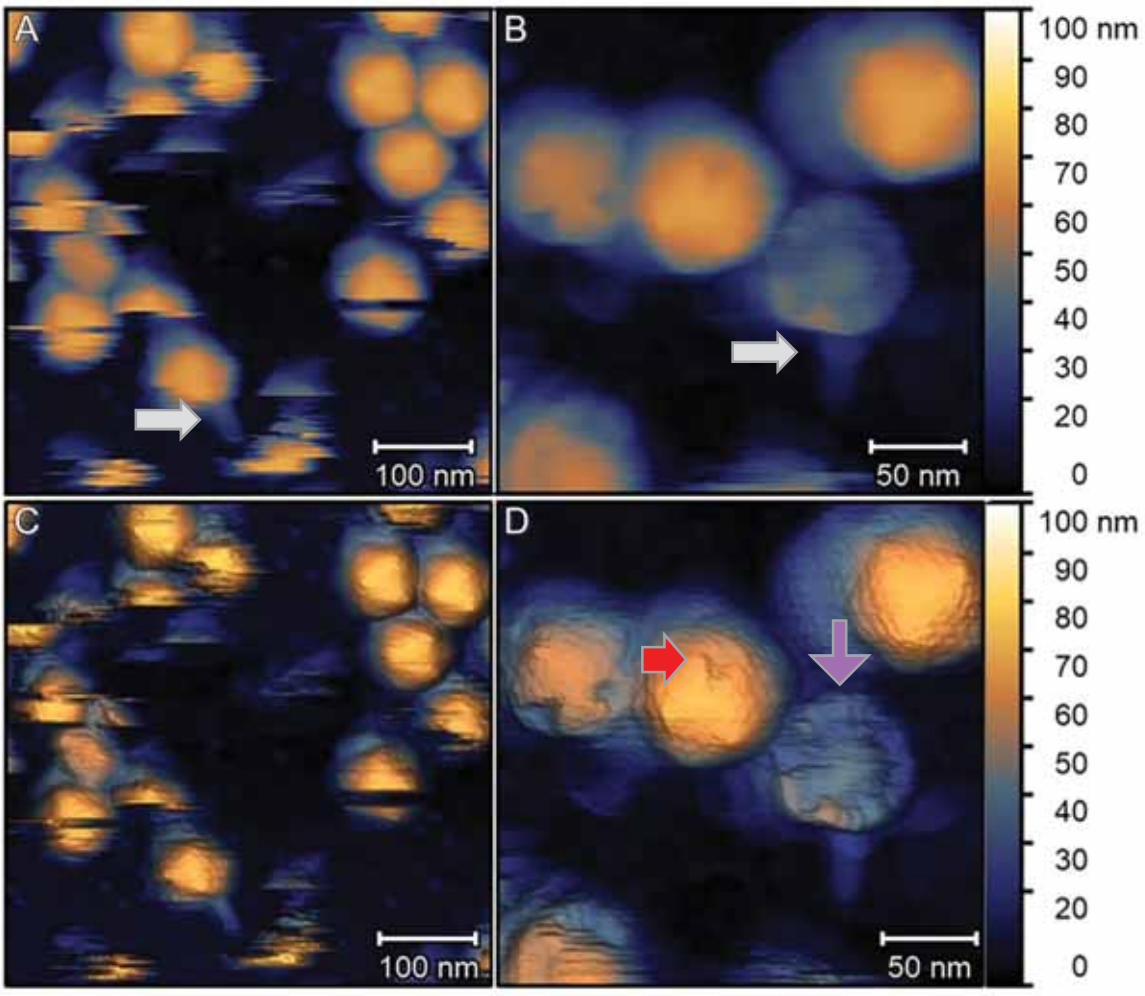

Figure 4.16: AFM images of wt PRD1 tubes. A-B show the topographic information, while C-D are the same images in 3D relief, allowing for appreciation of sub-features of the particles and tubes. White arrows indicate extended tubes that protrude from PRD1 particles. The red arrow shows a missing peripentonal vertex, while the purple arrow shows a particle with a big part of the protein capsid missing and the inner proteo-lipidic membrane visible. Note that the membrane is still present even though the tube has formed and is protruding from the particle.

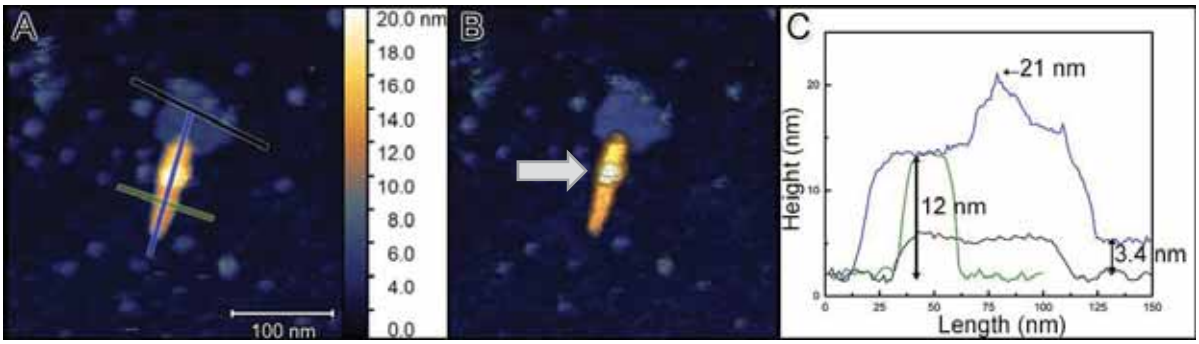

Figure 4.17: (A) Topographic AFM image of an individual tube. A possible membrane patch resulting from the rupture of a vesicle (3.4 nm in height, black line in C) appears to be still in contact with the tube, suggesting that the structure of the tube is more resilient to deformation than the lipid vesicle itself. (B) 3D relief of the same area. The tube (~12 nm in height; blue line profile in C) appeared to be intact throughout its length, consistent with previous observations, and hinting towards its stability. A ring-like structure of roughly 18.5 nm height (grey arrow) was also observed attached to some of the tubes, as it was previously seen via EM in (Peralta et al., 2013). (C) shows topographic line profiles across the length of the tube (blue), a cross section (green), and the lipid vesicle (black), as indicated by lines in matching colours in A. Notable heights are also marked on the graph.

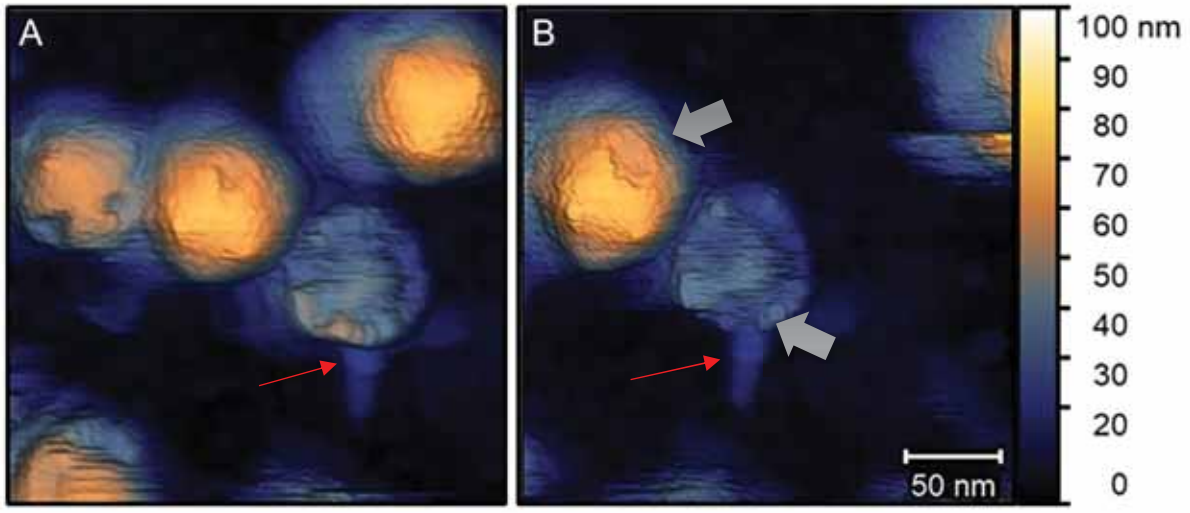

Figure 4.18: Set of two sequentially acquired 3D-relief images (t=3-4 min) corresponding to a zoomed-in area from Figure 4.16B with an individual protruding tube of PRD1 visible. Tubes similar to this allowed for nano-indentation experiments. The area adjacent to the tube was indented to establish hard-wall contact before and after indentation of the tube. We observed some particles can be displaced between imaging (top right particle) and that already damaged particles exhibited some further amount of deterioration as some capsomers are removed (grey arrows). The ring structure around the tube is also visible and indicated by the red arrows.

4.3.2.2. Mechanical properties of PRD1's tubes

The combination of lipids and protein in the case of the PRD1 tube, resulted in a stiffness of k = 0.06 ± 0.03 N/m (mean ± s.d.; n = 10) and a yield force F_y = 0.24 ± 0.12 (mean ± s.d.) (Table 2).

Table 2: Slope values (stiffness) for the selected tubes, along with the start of forces. The mean stiffness value is 0.06 ± 0.01 N/m (S.E.M), while the mean yield force is 0.24 ± 0.04 nN (S.E.M.).

k (N/m)	h_s (nm)	F_y (nN)
0.1	17.32	0.39
0.06	16.1	0.4
0.08	12.12	0.3588
0.07	10.91	0.336
0.03	14.49	0.12
0.03	17.337	0.14
0.03	14.75	0.17
0.08	17.22	0.18
0.03	15.21	0.13
0.05	13.6	0.11

We observe that the proteo-lipidic PRD1 tube is stiffer than the PRD1-derived lipid vesicles (0.02 N/m, Figure 3.6) or even thick lipid tubules (0.03 N/m, (Zhao et al., 2009)). However, it is orders of magnitude less stiff when compared to wt PRD1's stiffness (0.6 N/m, Figure 3.6) or the similarly sized and shaped TMV's stiffness (0.34 N/m, (Zhao et al., 2008)). In the 2008 study, Zhao *et al* have estimated the stiffness for TMV at approximately 0.8 N/m, a virus with a diameter of 18 nm and inner diameter of 4 nm, resulting from a "thick" tubular proteinic structure. On the contrary, investigating lipid tubules of varying thickness and diameters, (Zhao et al., 2009) have calculated the values as high as 0.06 N/m for lipid tubules, with multiple-bilayer walls, of ~600 nm in diameter and a wall-thickness of 66 nm. In the case of the PRD1 tube, the stiffness value is 0.06 ± 0.01 N/m (mean ± S.E.M.), with an initial yield step of 0.24 ± 0.04 nN (mean ± S.E.M.).

Imaging on tubes after their nanoindentation did not reveal a major structural modification of the surface of the tube in the majority of the cases (90%; n = 10) which suggest that the discrete yield steps could correspond to protein reorganization, and that the tube "heals" quickly

following compression and yield response. However, when a tube was indented multiple times in the same area (Figure 4.19), some damage to the tube could be revealed, indicating that strong mechanical perturbation and possible the extraction of proteins by the AFM probe, can induce irreversible damage.

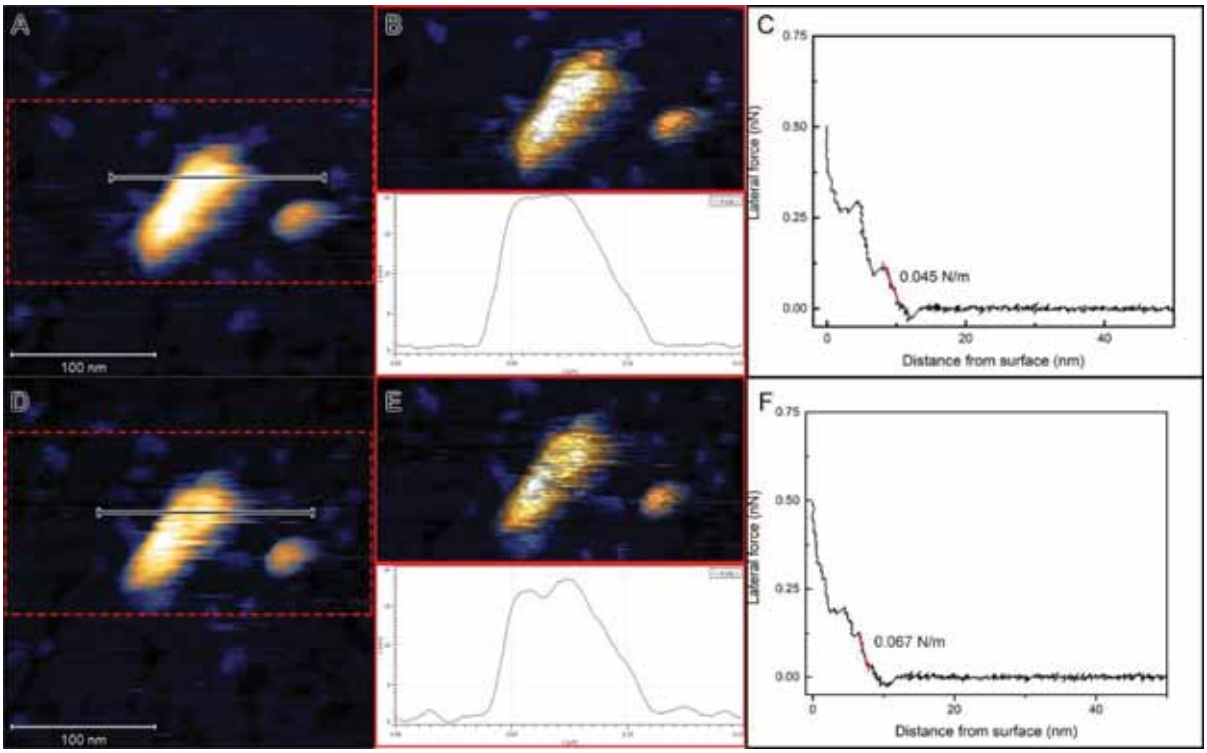

Figure 4.19: Two sequentially acquired topographic images (A and D) showing tube "damage" after multiple nanoindentations on the same site prior to the second image (z-height: 20 nm). (B and E) show a 3D relief of the marked area in A and D respectively (top panels), as well as a height profile (average over 5 scan lines) of the marked area. A drop of ~20% percent in height is visible in the area. (C and F) corresponding nanoindentation force curves revealing local stiffness values, as well as discrete yield points. A minor attractive force (~10 pN) prior to compression was also visible.

Performing consecutive linear nanoindentations in our system (Figure 4.20), we observed no visible damage to the tube, as well as the middle nanoindentations (Figure 4.20E), exhibiting characteristics corresponding to nanoindentation of the tube. These both show that the system drifts were within few nanometers of range between image and nanoindentation, since the FCs that exhibited the expected profiles were the 4-6th ones corresponding to nanoindentations on top of the tube. Due to the nominal tip radius (15 nm, Bruker), and the nanoindentation

periodicity of 10 nm, we can roughly estimate drifts of 2-4 nm, giving confidence in the acquired individual nanoindentations.

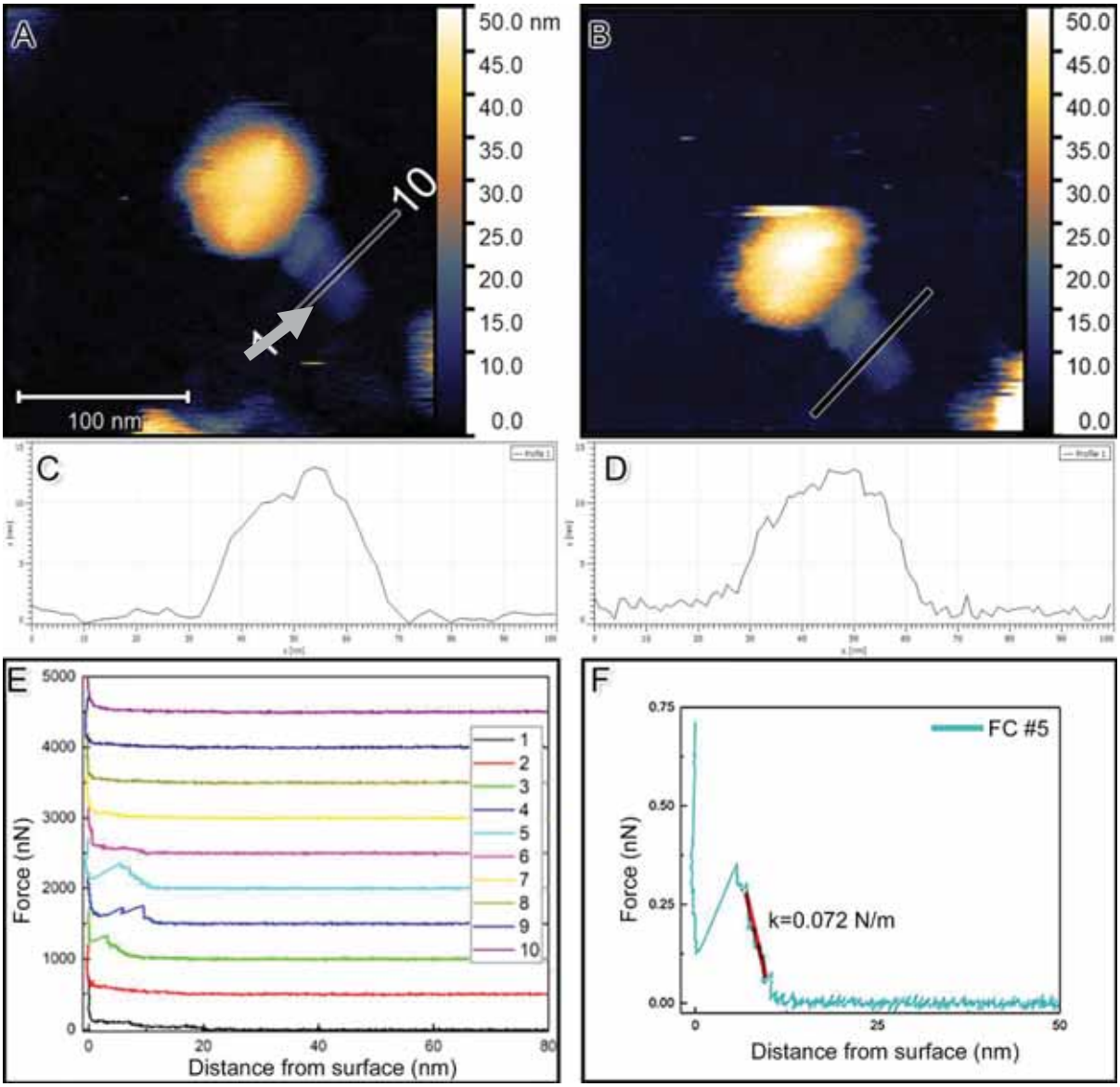

Figure 4.20: Hard-wall contact and drift test. (A) AFM topographic image showing a PRD1 particle with a protruding tube. The arrow marks the characteristic ring-like structure. Ten nanoindentations across the tube were performed, starting from point 1 to point 10 in equidistant steps of 10 nm (along the line). (B) AFM topographic image of the same particle after the consecutive nanoindentations. No visible damage along the tube structure was observed. (C), (D) Height profiles for the corresponding lines on (A) and (B). (E) The ten consecutive nanoindentations corresponding at points across line marked in (A). Since the middle FC showed the expected profile, as indicated on (F), this allowed us to estimate that the drift between image acquisition and nanoindentation must be in the range of few nanometers.

4.4. DISCUSSION

Tailed phages are considered the most common type of viruses in the biosphere and have a well-defined structure. A tailed phage has an isometric head (usually of an icosahedral symmetry) of tightly fitted protein capsomers with a wide variety of diameters (with a large population sized at 60 nm), and a highly organized tube of fixed length and width. The tail generally has a helical *six-fold* symmetry, and is held together by the connector; a small disk located inside the head or near the site of tube attachment. The connector, a universal component of tailed phages, is known to correct the mismatch between the vertex five-fold symmetry of the head and the six-fold symmetry of the tube. It is frequently seen associated with tubes in disrupted phages.

Our study shows that PRD1 is distinct in this matter, where a *seven-fold* symmetry is seen in its self-assembled tube. This self-assembled nanotube protrudes from the unique vertex which has been recently elucidated in great detail by cryo-EM (Hong et al., 2014).

In PRD1 studies of the $P32^{-}$ mutant, the formation of an extended tube is inhibited, while disruption of protein capsid produces vesicles without any tube at all compared to the wt PRD1 (Grahn et al., 2002b). This lets us to postulate that membrane protein P32 (54 residues, with residues 4-24 predicted as a transmembrane helix) might be involved in the polymerization and formation of the PRD1 tube. As previous studies have shown that the remodelling of the internal membrane is associated with the formation of the tube (Peralta et al., 2013), we propose that the unique vertex acts as a funnel, bringing ("zipping") in contact the polymerizing membrane-associated protein(s) (possibly P32) as the internal membrane vesicle leaves the empty and fragile protein capsid behind. This assembly mechanism would originate a stiffer tube necessary for the injection of the genomic material inside the bacteria (Figure 4.22A).

Mechanically, we were able to see that the tube is stiffer than a pure lipid vesicle, but at the same time not as stiff as compact and thick protein rich tubes and viruses (Zhao et al., 2009, Zhao et al., 2008). Our results are comparable with the nanoindentation results on protein

microtubules, which are known to be resistant to bending (de Pablo et al., 2003). This is important for the virion itself, as the tube has to resist a certain amount of forces during ejection of the genome. The thickness of the proteo-lipidic layer in our case is roughly 25 Å, with a layer thickness-to-radius ratio of 0.45, similar to the ratio of protein microtubules.

Based on our findings regarding the role of the lipid vesicle in Chapter 3, we postulate that, in the PRD1 ejection tube, the role of the external thin lipid layer in combination with the well-structured inner protein layer could allow for the tube to penetrate and infect effectively. From one side, this combination would allow for better protection of the DNA delivery during ejection, and from the other side, the presence of a protein in the inside facilitates the passing of the genome, in particular if negatively charged residues are exposed (Zidovetzki R, rzlab.ucr.edu; Figure 4.21).

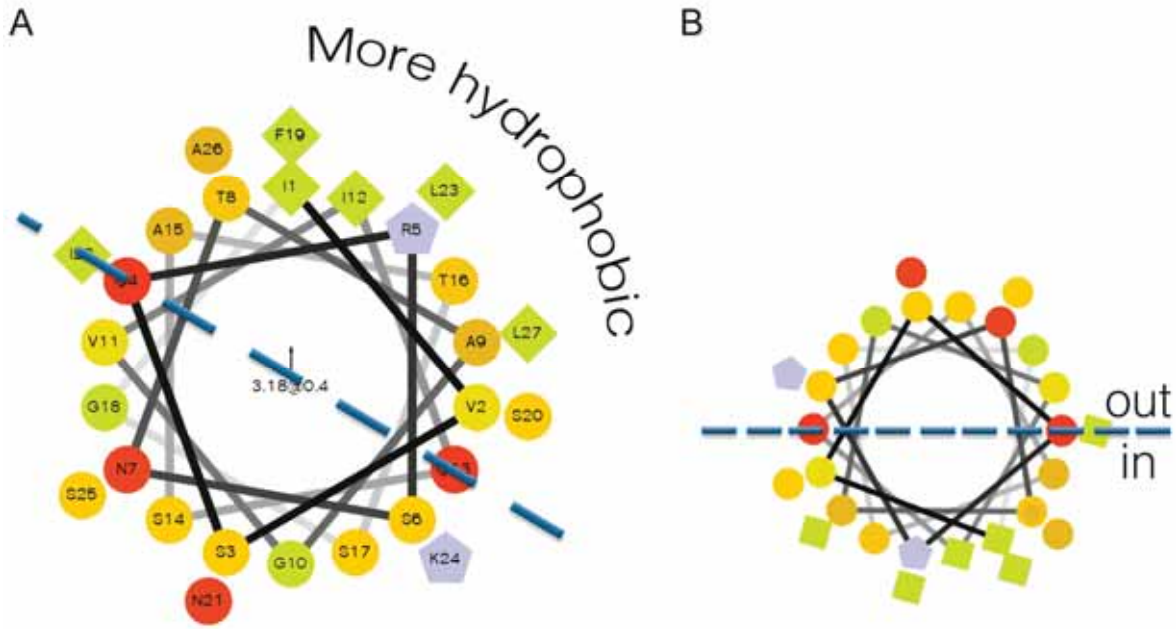

Figure 4.21: Helix wheel prediction of hydrophobicity of residues 25-54 of protein P32. (A) The hydrophilic residues as circles, hydrophobic residues as diamonds, potentially negatively charged as triangles, and potentially positively charged as pentagons. Hydrophobicity is color coded as well: the most hydrophobic residue is green, and the amount of green is decreasing proportionally to the hydrophobicity, with zero hydrophobicity coded as yellow. Hydrophilic residues are coded red with pure red being the most hydrophilic (uncharged) residue, and the amount of red decreasing proportionally to the hydrophilicity. The potentially charged residues are light blue. There is a separation of hydrophilic and hydrophobic residues across the helix marked with a blue dashed line. (B) Rotated wheel, with predicted regions being towards the outside of the membrane or inside.

In previous cryo-ET studies [(Peralta et al., 2013); Figure 4.1] the tube density is seen penetrating the cell wall, and passing all the way through, indicating that: 1) the tube is not composed purely of lipids, as they would have fused with the cell membrane, and 2) the tube has to be relatively rigid in order to penetrate. Furthermore, the adoption of a particular seven-fold symmetry not previously found in other proteinaceous phage tails also suggest a different solution that evolution has provided for this type of membrane containing virus. Gathering information from (Grahn et al., 2002b), we hypothesize that transmembrane P32 protein is coming into play during tube assembly. Predicted models using I-TASSER (Roy et al., 2012, Zhang, 2009, Yang and Zhang, 2015), show that P32 is likely formed by α-helices (Figure 4.22B). We propose that the more hydrophobic N-terminal is crossing the bilayer, while the other deeply embedded through the lipid bilayer, as it might be amphiphatic (Figure 4.21 and Figure 4.22C-D).

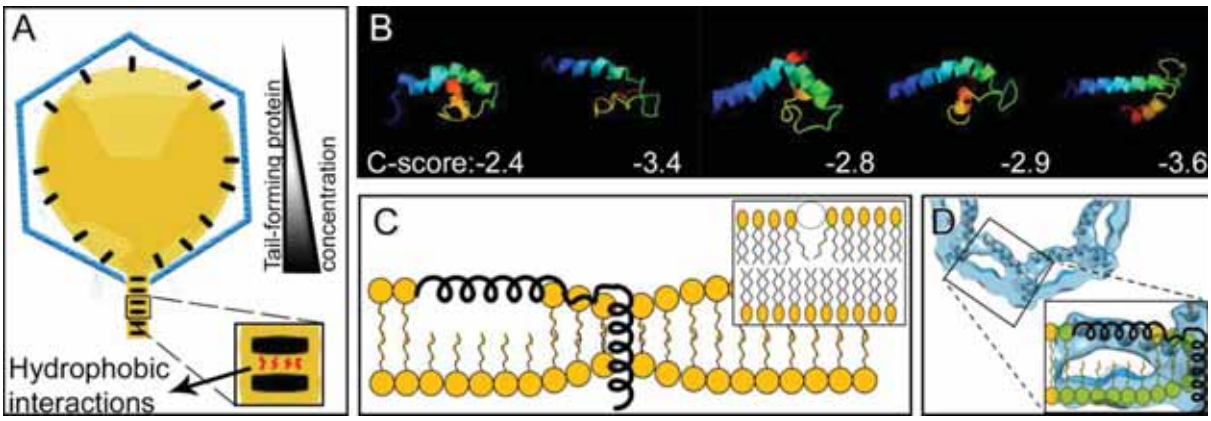

Figure 4.22: (A) Schematic representation of the suspected model of PRD1's tube formation. As the protein concentration increases when the proteo-lipid membrane is passing through the funnel-like unique vertex, polymerization occurs, and the tube is formed. Each 7-unit disk is thought to interact with each other through hydrophobic interactions. (B) Candidate tube-forming protein P32 predicted structures through I-TASSER. Under each structure, the calculated C-score [-5, 2] with larger numbers implying higher confidence (best score -2.4). (C) Schematic representation of a lipid bilayer, with one embedded transmembrane protein that with one helix embedded in the outer layer of the bilayer, and a transmembrane helix causing bilayer thinning. Inset adapted from (Lee, 2004), showing a side-view of an embedded in bilayer helix. (D) Fitted density from Figure 4.13 showing one "disk" density layer of PRD1's tube, while inset overlays how the lipids could be present on one lobe of the tube.

The combined structural and mechanical study of the PRD1 tube provides new insight and raises questions regarding the formation of such a system in non-tailed phages. While a similar system of a thin, curved lipid layer was recently seen on a filamentous virus that infects

archaea (Kasson et al., 2017), it is interesting that a similar structure was adopted by PRD1 in order to translocate its genome. At the same time, the lipid vesicle perhaps continues to offer a protective and reinforcing role during translocation, just as it does for the wt PRD1 particle (previous chapter).

4.5. CONCLUSIONS

In summary, we have performed a preliminary 3D reconstruction of the structure of the ejection tube of PRD1. Interestingly, we observe a seven-fold symmetry, and furthermore, a double layer with a less defined outer lipid layer, and a well-structured inner layer. The tube is likely formed by a stack of repeating disks composed of seven subunits, which we hypothesise are copies of transmembrane protein P32. This provides insight into the assembly of the tube, as when the proteo-lipidic membrane is passing through a funnel-like unique vertex, causes the polymerization of these proteins. Furthermore, the nano-mechanical investigation of the tube via AFM, shows a material that is stiffer than the lipid vesicle alone, but also hints the possibility that the tube has healing properties. The formation of these tubes could benefit nanoengineers in creating new antibacterials, as the combined lipid-protein architecture could allow further biochemical manipulation for nanodrilling bacterial cell walls.

While extensive studies have been performed to investigate the function of this archetypal member of the *Tectiviridae* family, its evolution and conservative use of its constituents suggests an engineering marvel that is worth understanding in depth.

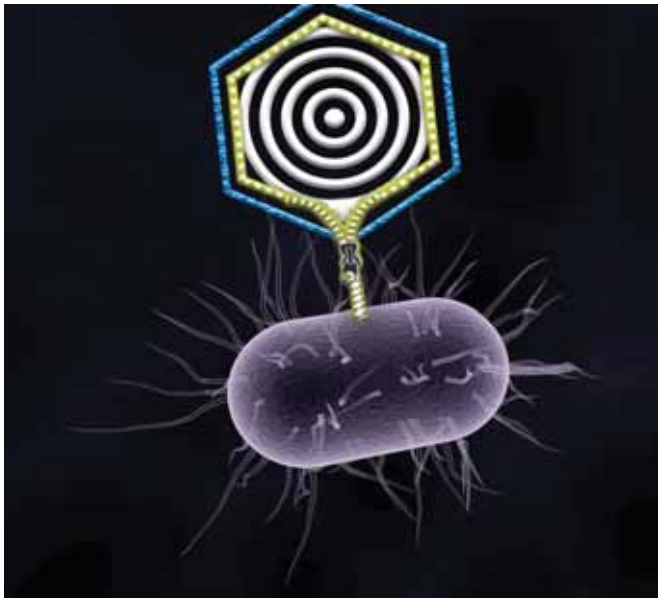

Figure 4.23: Artistic impression of a PRD1 particle infecting a bacterium (not to scale), where the distinct layers of the virion are visible. The internal protein-rich lipid membrane (yellow) starts to remodel and, with the help of a zipper-like connector, the polymerizing proteins form a stiff tube allowing the injection of the dsDNA inside the cell.

Insights into the Structure and mechanics of the PRD1 DNA ejection tail tube

Chapter 5: Conclusions and perspectives

5. CONCLUSIONS AND PERSPECTIVES

5.1. CONCLUSIONS

- Viruses can be seen as composite biological entities where nucleic acids, proteins and lipids assemble to produce functional particles for infection. This thesis has provided first insight into the nanomechanical properties of viruses with an internal membrane. It can be expected that it will become a reference for future work with this class of viruses.

- PRD1 nanomechanical properties show that the pressurised genome provides stiffness, but does not enhance stability, as genome-free particles yield under the same force, even if they are less stiff.

- Particles containing the lipid vesicle yield 3 times later than the penton-less protein capsid particles.

- Proteo-lipidic vesicle is orders of magnitude less stiff than any PRD1 particle investigated, but behaves similarly to other lipid vesicles.

- We propose that, as in a composite sandwich material, an interfacial protein/polypeptide matrix in PRD1 generates a tight connection that mechanically couples capsid and membrane. It will be interesting to see, if the design principle of enhancing mechanical stability by forming of a composite membrane-capsid double shell is unique to PRD1 or generally employed for this class of viruses.

- The DNA ejection tube of PRD1 is composed of proteo-lipidic material. The polymerization of the tube-forming protein leads to a series of stacked disks, each composed of seven subunits, and having a seven-fold symmetry, but not a helical one.

- Previous PRD1 phage mutation studies, along with our current results, suggest that transmembrane protein P32 is the polymerizing protein.

- This protein enrichment during membrane remodelling leads to a thinner, collapsed lipid bilayer during the polymerization of the tube.

- The nanomechanical characteristics of the tube, in addition to the presence of a defined structure, hint on the presence of protein material, as it exhibits a stiffer character compared to the lipid vesicle alone.

5.2. PERSPECTIVES

As we answered some questions regarding the mechanical structure and assembly of the PRD1 capsid and tube, further questions also arise.

1. Concluding work on the tube structure needs to be performed.
2. It remains to validate whether other membrane-containing viruses display a similar behaviour as shown by PRD1. This could generalize our proposed model that the multi-layered architecture provides greater particle stability.
3. Investigating P32 mutants, which produce shorter tubes would provide further insight in the assembly of the nanotube.

In a broad perspective, our results can help nanoengineers in their quest for more stable nanoparticles, as the composite nature of PRD1 can be an inspiration for nanoparticle design. Furthermore, the quest for new antimicrobials, could be assisted by the use of nanodrilling machines, such as bacteriophage PRD1's ejection tube.

Chapter 6: Bibliography

6. BIBLIOGRAPHY

ABRESCIA, N. G., BAMFORD, D. H., GRIMES, J. M. & STUART, D. I. 2012. Structure unifies the viral universe. *Annu Rev Biochem,* 81**,** 795-822.

ABRESCIA, N. G., COCKBURN, J. J., GRIMES, J. M., SUTTON, G. C., DIPROSE, J. M., BUTCHER, S. J., FULLER, S. D., SAN MARTIN, C., BURNETT, R. M., STUART, D. I., BAMFORD, D. H. & BAMFORD, J. K. 2004. Insights into assembly from structural analysis of bacteriophage PRD1. *Nature,* 432**,** 68-74.

ACKERMANN, H. W. & KROPINSKI, A. M. 2007. Curated list of prokaryote viruses with fully sequenced genomes. *Res Microbiol,* 158**,** 555-66.

ADRIAN, M., DUBOCHET, J., LEPAULT, J. & MCDOWALL, A. W. 1984. Cryo-electron microscopy of viruses. *Nature,* 308**,** 32-6.

AMOS, L. A. & KLUG, A. 1975. Three-dimensional image reconstructions of the contractile tail of T4 bacteriophage. *J Mol Biol,* 99**,** 51-64.

ASHKIN, A. & DZIEDZIC, J. M. 1987. Optical trapping and manipulation of viruses and bacteria. *Science,* 235**,** 1517-20.

BAMFORD, D. & MINDICH, L. 1982. Structure of the lipid-containing bacteriophage PRD1: disruption of wild-type and nonsense mutant phage particles with guanidine hydrochloride. *J Virol,* 44**,** 1031-8.

BAMFORD, J. K. & BAMFORD, D. H. 1990. Capsomer proteins of bacteriophage PRD1, a bacterial virus with a membrane. *Virology,* 177**,** 445-51.

BAMFORD, J. K. & BAMFORD, D. H. 1991. Large-scale purification of membrane-containing bacteriophage PRD1 and its subviral particles. *Virology,* 181**,** 348-52.

BINNIG, G., QUATE, C. F. & GERBER, C. 1986. Atomic force microscope. *Phys Rev Lett,* 56**,** 930-933.

BINNIG, G. & ROHRER, H. 1999. In touch with atoms. *Reviews of Modern Physics,* 71**,** S324.

BLOW, D. 2002. *Outline of crystallography for biologists*, Oxford University Press on Demand.

BRADFORD, M. M. 1976. A rapid and sensitive method for the quantitation of microgram quantities of protein utilizing the principle of protein-dye binding. *Anal Biochem,* 72**,** 248-54.

BUTCHER, S. J., MANOLE, V. & KARHU, N. J. 2012. Lipid-containing viruses: bacteriophage PRD1 assembly. *Adv Exp Med Biol,* 726**,** 365-77.

BUTT, H.-J. & JASCHKE, M. 1995. Calculation of thermal noise in atomic force microscopy. *Nanotechnology,* 6**,** 1.

CALLAWAY, E. 2015. The revolution will not be crystallized: a new method sweeps through structural biology. *Nature,* 525**,** 172-4.

CARRASCO, C., CARREIRA, A., SCHAAP, I. A., SERENA, P. A., GOMEZ-HERRERO, J., MATEU, M. G. & DE PABLO, P. J. 2006. DNA-mediated anisotropic mechanical reinforcement of a virus. *Proc Natl Acad Sci U S A,* 103**,** 13706-11.

CARRASCO, C., LUQUE, A., HERNANDO-PEREZ, M., MIRANDA, R., CARRASCOSA, J. L., SERENA, P. A., DE RIDDER, M., RAMAN, A., GOMEZ-HERRERO, J., SCHAAP, I. A., REGUERA, D. & DE PABLO, P. J. 2011. Built-in mechanical stress in viral shells. *Biophys J,* 100**,** 1100-8.

COCKBURN, J. J., ABRESCIA, N. G., GRIMES, J. M., SUTTON, G. C., DIPROSE, J. M., BENEVIDES, J. M., THOMAS, G. J., JR., BAMFORD, J. K., BAMFORD, D. H. & STUART, D. I. 2004. Membrane structure and interactions with protein and DNA in bacteriophage PRD1. *Nature,* 432**,** 122-5.

CRAIG, L., VOLKMANN, N., ARVAI, A. S., PIQUE, M. E., YEAGER, M., EGELMAN, E. H. & TAINER, J. A. 2006. Type IV pilus structure by cryo-electron microscopy and crystallography: implications for pilus assembly and functions. *Mol Cell,* 23**,** 651-62.

CRAMPTON, N., BONASS, W. A., KIRKHAM, J. & THOMSON, N. H. 2005. Formation of aminosilane-functionalized mica for atomic force microscopy imaging of DNA. *Langmuir,* 21**,** 7884-91.

CRESSEY, D. & CALLAWAY, E. 2017. Cryo-electron microscopy wins chemistry Nobel. *Nature,* 550**,** 167.

CROWTHER, R. A., AMOS, L. A., FINCH, J. T., DE ROSIER, D. J. & KLUG, A. 1970. Three Dimensional Reconstructions of Spherical Viruses by Fourier Synthesis from Electron Micrographs. *Nature,* 226**,** 421.

CUELLAR, J. L., MEINHOEVEL, F., HOEHNE, M. & DONATH, E. 2010. Size and mechanical stability of norovirus capsids depend on pH: a nanoindentation study. *J Gen Virol,* 91**,** 2449-56.

DE LA ROSA-TREVIN, J. M., QUINTANA, A., DEL CANO, L., ZALDIVAR, A., FOCHE, I., GUTIERREZ, J., GOMEZ-BLANCO, J., BURGUET-CASTELL, J., CUENCA-ALBA, J., ABRISHAMI, V., VARGAS, J., OTON, J., SHAROV, G., VILAS, J. L., NAVAS, J., CONESA, P., KAZEMI, M., MARABINI, R., SORZANO, C. O. & CARAZO, J. M. 2016. Scipion: A software framework toward integration, reproducibility and validation in 3D electron microscopy. *J Struct Biol,* 195**,** 93-9.

DE PABLO, P., COLCHERO, J., GOMEZ-HERRERO, J. & BARO, A. 1998. Jumping mode scanning force microscopy. *Applied Physics Letters,* 73**,** 3300-3302.

DE PABLO, P. J., SCHAAP, I. A., MACKINTOSH, F. C. & SCHMIDT, C. F. 2003. Deformation and collapse of microtubules on the nanometer scale. *Phys Rev Lett,* 91**,** 098101.

DIMAIO, F., ECHOLS, N., HEADD, J. J., TERWILLIGER, T. C., ADAMS, P. D. & BAKER, D. 2013. Improved low-resolution crystallographic refinement with Phenix and Rosetta. *Nat Methods,* 10**,** 1102-4.

DIMITRIADIS, E. K., HORKAY, F., MARESCA, J., KACHAR, B. & CHADWICK, R. S. 2002. Determination of elastic moduli of thin layers of soft material using the atomic force microscope. *Biophys J,* 82**,** 2798-810.

DOERR, A. 2016. Single-particle cryo-electron microscopy. *Nat Methods,* 13**,** 23.

DUDA, R. L., HENDRIX, R. W., HUANG, W. M. & CONWAY, J. F. 2006. Shared architecture of bacteriophage SPO1 and herpesvirus capsids. *Curr Biol,* 16**,** R11-3.

DUFRÊNE, Y.F., ANDO, T., GARCIA, R., ALSTEENS, D., MARTINEZ-MARTIN, D., ENGEL, A., GERBER, C. AND MÜLLER, D.J., 2017. Imaging modes of atomic force microscopy for application in molecular and cell biology. *Nature nanotechnology*, 12(4), p.295.

EGELMAN, E. H. 2000. A robust algorithm for the reconstruction of helical filaments using single-particle methods. *Ultramicroscopy,* 85**,** 225-34.

EGHIAIAN, F., SCHAAP, I. A., DES GEORGES, A., SKEHEL, J. J. & VEIGEL, C. 2009. The influenza virus mechanical properties are dominated by its lipid envelope. *Biophysical journal,* 96**,** 15a.

EMSLEY, P., LOHKAMP, B., SCOTT, W. G. & COWTAN, K. 2010. Features and development of Coot. *Acta Crystallogr D Biol Crystallogr,* 66**,** 486-501.

EVILEVITCH, A., LAVELLE, L., KNOBLER, C. M., RASPAUD, E. & GELBART, W. M. 2003. Osmotic pressure inhibition of DNA ejection from phage. *Proc Natl Acad Sci U S A,* 100**,** 9292-5.

FALVO, M. R., WASHBURN, S., SUPERFINE, R., FINCH, M., BROOKS, F. P., JR., CHI, V. & TAYLOR, R. M., 2ND 1997. Manipulation of individual viruses: friction and mechanical properties. *Biophys J,* 72**,** 1396-403.

FOKINE, A., LEIMAN, P. G., SHNEIDER, M. M., AHVAZI, B., BOESHANS, K. M., STEVEN, A. C., BLACK, L. W., MESYANZHINOV, V. V. & ROSSMANN, M. G. 2005. Structural and functional similarities between the capsid proteins of bacteriophages T4 and HK97 point to a common ancestry. *Proc Natl Acad Sci U S A,* 102**,** 7163-8.

GELBART, W. M. & KNOBLER, C. M. 2009. Virology. Pressurized viruses. *Science,* 323**,** 1682-3.

GHOSAL, S. 2012. Capstan friction model for DNA ejection from bacteriophages. *Phys Rev Lett,* 109**,** 248105.

GITTES, F. & SCHMIDT, C. F. 1998. Interference model for back-focal-plane displacement detection in optical tweezers. *Opt Lett,* 23**,** 7-9.

GOWEN, B., BAMFORD, J. K., BAMFORD, D. H. & FULLER, S. D. 2003. The tailless icosahedral membrane virus PRD1 localizes the proteins involved in genome packaging and injection at a unique vertex. *J Virol,* 77**,** 7863-71.

GRAHN, A. M., DAUGELAVICIUS, R. & BAMFORD, D. H. 2002a. Sequential model of phage PRD1 DNA delivery: active involvement of the viral membrane. *Mol Microbiol,* 46**,** 1199-209.

GRAHN, A. M., DAUGELAVICIUS, R. & BAMFORD, D. H. 2002b. The small viral membrane-associated protein P32 is involved in bacteriophage PRD1 DNA entry. *J Virol,* 76**,** 4866-72.

GRIGORIEFF, N. & HARRISON, S. C. 2011. Near-atomic resolution reconstructions of icosahedral viruses from electron cryo-microscopy. *Curr Opin Struct Biol,* 21**,** 265-73.

HAMMERUM, A. M., LESTER, C. H. & HEUER, O. E. 2010. Antimicrobial-resistant enterococci in animals and meat: a human health hazard? *Foodborne Pathog Dis,* 7**,** 1137-46.

HE, S. & SCHERES, S. H. W. 2017. Helical reconstruction in RELION. *J Struct Biol,* 198**,** 163-176.

HELLER, I., HOEKSTRA, T. P., KING, G. A., PETERMAN, E. J. & WUITE, G. J. 2014. Optical tweezers analysis of DNA-protein complexes. *Chem Rev,* 114**,** 3087-119.

HENDERSON, R. 2015. Overview and future of single particle electron cryomicroscopy. *Arch Biochem Biophys,* 581**,** 19-24.

HERNANDO-PEREZ, M., LAMBERT, S., NAKATANI-WEBSTER, E., CATALANO, C. E. & DE PABLO, P. J. 2014. Cementing proteins provide extra mechanical stabilization to viral cages. *Nat Commun,* 5**,** 4520.

HONG, C., OKSANEN, H. M., LIU, X., JAKANA, J., BAMFORD, D. H. & CHIU, W. 2014. A structural model of the genome packaging process in a membrane-containing double stranded DNA virus. *PLoS Biol,* 12**,** e1002024.

HUISKONEN, J. T., MANOLE, V. & BUTCHER, S. J. 2007. Tale of two spikes in bacteriophage PRD1. *Proc Natl Acad Sci U S A,* 104**,** 6666-71.

IDO, S., KIMIYA, H., KOBAYASHI, K., KOMINAMI, H., MATSUSHIGE, K. & YAMADA, H. 2014. Immunoactive two-dimensional self-assembly of monoclonal antibodies in aqueous solution revealed by atomic force microscopy. *Nat Mater,* 13**,** 264-70.

INAMDAR, M. M., GELBART, W. M. & PHILLIPS, R. 2006. Dynamics of DNA ejection from bacteriophage. *Biophys J,* 91**,** 411-20.

IVANOVSKA, I., WUITE, G., JONSSON, B. & EVILEVITCH, A. 2007. Internal DNA pressure modifies stability of WT phage. *Proc Natl Acad Sci U S A,* 104**,** 9603-8.

IVANOVSKA, I. L., DE PABLO, P. J., IBARRA, B., SGALARI, G., MACKINTOSH, F. C., CARRASCOSA, J. L., SCHMIDT, C. F. & WUITE, G. J. 2004. Bacteriophage capsids: tough nanoshells with complex elastic properties. *Proc Natl Acad Sci U S A,* 101**,** 7600-5.

JAATINEN, S. T., VIITANEN, S. J., BAMFORD, D. H. & BAMFORD, J. K. 2004. Integral membrane protein P16 of bacteriophage PRD1 stabilizes the adsorption vertex structure. *J Virol,* 78**,** 9790-7.

JEEMBAEVA, M., JONSSON, B., CASTELNOVO, M. & EVILEVITCH, A. 2010. DNA heats up: energetics of genome ejection from phage revealed by isothermal titration calorimetry. *J Mol Biol,* 395**,** 1079-87.

JIANG, W., BAKER, M. L., JAKANA, J., WEIGELE, P. R., KING, J. & CHIU, W. 2008. Backbone structure of the infectious epsilon15 virus capsid revealed by electron cryomicroscopy. *Nature,* 451**,** 1130-4.

KAEMMER, S. B. 2011. Introduction to bruker's scanasyst and peakforce tapping afm technology. *Bruker application note. Bruker Nano Inc., Santa Barbara, CA*.

KAHN, M. L., ZIERMANN, R., DEHO, G., OW, D. W., SUNSHINE, M. G. & CALENDAR, R. 1991. Bacteriophage P2 and P4. *Methods Enzymol,* 204**,** 264-80.

KASSON, P., DIMAIO, F., YU, X., LUCAS-STAAT, S., KRUPOVIC, M., SCHOUTEN, S., PRANGISHVILI, D. & EGELMAN, E. H. 2017. Model for a novel membrane envelope in a filamentous hyperthermophilic virus. *Elife,* 6.

KINDT, J., TZLIL, S., BEN-SHAUL, A. & GELBART, W. M. 2001. DNA packaging and ejection forces in bacteriophage. *Proc Natl Acad Sci U S A,* 98**,** 13671-4.

KOL, N., SHI, Y., TSVITOV, M., BARLAM, D., SHNECK, R. Z., KAY, M. S. & ROUSSO, I. 2007. A stiffness switch in human immunodeficiency virus. *Biophys J,* 92**,** 1777-83.

KONONOVA, O., MAKSUDOV, F., MARX, K. A. & BARSEGOV, V. 2018. TensorCalculator: exploring the evolution of mechanical stress in the CCMV capsid. *J Phys Condens Matter,* 30**,** 044006.

KONONOVA, O., SNIJDER, J., KHOLODOV, Y., MARX, K. A., WUITE, G. J., ROOS, W. H. & BARSEGOV, V. 2016. Fluctuating Nonlinear Spring Model of Mechanical Deformation of Biological Particles. *PLoS Comput Biol,* 12**,** e1004729.

KUZNETSOV, Y. G., XIAO, C., SUN, S., RAOULT, D., ROSSMANN, M. & MCPHERSON, A. 2010. Atomic force microscopy investigation of the giant mimivirus. *Virology,* 404**,** 127-37.

LEE, A. G. 2004. How lipids affect the activities of integral membrane proteins. *Biochim Biophys Acta,* 1666**,** 62-87.

LEIMAN, P. G., ARISAKA, F., VAN RAAIJ, M. J., KOSTYUCHENKO, V. A., AKSYUK, A. A., KANAMARU, S. & ROSSMANN, M. G. 2010. Morphogenesis of the T4 tail and tail fibers. *Virol J,* 7**,** 355.

LEIMAN, P. G., CHIPMAN, P. R., KOSTYUCHENKO, V. A., MESYANZHINOV, V. V. & ROSSMANN, M. G. 2004. Three-dimensional rearrangement of proteins in the tail of bacteriophage T4 on infection of its host. *Cell,* 118**,** 419-29.

LI, X., MOONEY, P., ZHENG, S., BOOTH, C. R., BRAUNFELD, M. B., GUBBENS, S., AGARD, D. A. & CHENG, Y. 2013. Electron counting and beam-induced motion correction enable near-atomic-resolution single-particle cryo-EM. *Nat Methods,* 10**,** 584-90.

LIASHKOVICH, I., HAFEZI, W., KÜHN, J. E., OBERLEITHNER, H., KRAMER, A. & SHAHIN, V. 2008. Exceptional mechanical and structural stability of HSV-1 unveiled with fluid atomic force microscopy. *Journal of Cell Science,* 121**,** 2287.

LIU, H., JIN, L., KOH, S. B., ATANASOV, I., SCHEIN, S., WU, L. & ZHOU, Z. H. 2010. Atomic structure of human adenovirus by cryo-EM reveals interactions among protein networks. *Science,* 329**,** 1038-43.

LLAURO, A., SCHWARZ, B., KOLIYATT, R., DE PABLO, P. J. & DOUGLAS, T. 2016. Tuning Viral Capsid Nanoparticle Stability with Symmetrical Morphogenesis. *ACS Nano,* 10**,** 8465-73.

LUCAS, R. W., KUZNETSOV, Y. G., LARSON, S. B. & MCPHERSON, A. 2001. Crystallization of Brome mosaic virus and T = 1 Brome mosaic virus particles following a structural transition. *Virology,* 286**,** 290-303.

LUDTKE, S. J., BALDWIN, P. R. & CHIU, W. 1999. EMAN: semiautomated software for high-resolution single-particle reconstructions. *J Struct Biol,* 128**,** 82-97.

LUO, C., BUTCHER, S. & BAMFORD, D. H. 1993. Isolation of a phospholipid-free protein shell of bacteriophage PRD1, an Escherichia coli virus with an internal membrane. *Virology,* 194**,** 564-9.

MARTIN, C. S., BURNETT, R. M., DE HAAS, F., HEINKEL, R., RUTTEN, T., FULLER, S. D., BUTCHER, S. J. & BAMFORD, D. H. 2001. Combined EM/X-ray imaging yields a quasi-atomic model of the adenovirus-related bacteriophage PRD1 and shows key capsid and membrane interactions. *Structure,* 9**,** 917-30.

MATEU, M. G. 2012. Mechanical properties of viruses analyzed by atomic force microscopy: a virological perspective. *Virus Res,* 168**,** 1-22.

MICHEL, J. P., IVANOVSKA, I. L., GIBBONS, M. M., KLUG, W. S., KNOBLER, C. M., WUITE, G. J. & SCHMIDT, C. F. 2006. Nanoindentation studies of full and empty viral capsids and the effects of capsid protein mutations on elasticity and strength. *Proc Natl Acad Sci U S A,* 103**,** 6184-9.

MILNE, J. L., BORGNIA, M. J., BARTESAGHI, A., TRAN, E. E., EARL, L. A., SCHAUDER, D. M., LENGYEL, J., PIERSON, J., PATWARDHAN, A. & SUBRAMANIAM, S. 2013. Cryo-electron microscopy--a primer for the non-microscopist. *FEBS J,* 280**,** 28-45.

MINDELL, J. A. & GRIGORIEFF, N. 2003. Accurate determination of local defocus and specimen tilt in electron microscopy. *J Struct Biol,* 142**,** 334-47.

MINDICH, L., BAMFORD, D., MCGRAW, T. & MACKENZIE, G. 1982. Assembly of bacteriophage PRD1: particle formation with wild-type and mutant viruses. *J Virol,* 44**,** 1021-30.

MINDICH, L., COHEN, J. & WEISBURD, M. 1976. Isolation of nonsense suppressor mutants in Pseudomonas. *J Bacteriol,* 126**,** 177-82.

MOFFITT, J. R., CHEMLA, Y. R., AATHAVAN, K., GRIMES, S., JARDINE, P. J., ANDERSON, D. L. & BUSTAMANTE, C. 2009. Intersubunit coordination in a homomeric ring ATPase. *Nature,* 457**,** 446-50.

MOFFITT, J. R., CHEMLA, Y. R., SMITH, S. B. & BUSTAMANTE, C. 2008. Recent advances in optical tweezers. *Annu Rev Biochem,* 77**,** 205-28.

MOLINEUX, I. J. 2001. No syringes please, ejection of phage T7 DNA from the virion is enzyme driven. *Mol Microbiol,* 40**,** 1-8.

MOLINEUX, I. J. & PANJA, D. 2013. Popping the cork: mechanisms of phage genome ejection. *Nat Rev Microbiol,* 11**,** 194-204.

NEUMAN, K. C. & BLOCK, S. M. 2004. Optical trapping. *Rev Sci Instrum,* 75**,** 2787-809.

NILSSON, A. S. 2014. Phage therapy--constraints and possibilities. *Ups J Med Sci,* 119**,** 192-8.

OLKKONEN, V. M. & BAMFORD, D. H. 1989. Quantitation of the adsorption and penetration stages of bacteriophage phi 6 infection. *Virology,* 171**,** 229-38.

OLSEN, R. H., SIAK, J. S. & GRAY, R. H. 1974. Characteristics of PRD1, a plasmid-dependent broad host range DNA bacteriophage. *J Virol,* 14**,** 689-99.

ORLOVA, E. V. & SAIBIL, H. R. 2011. Structural analysis of macromolecular assemblies by electron microscopy. *Chem Rev,* 111**,** 7710-48.

ORTEGA-ESTEBAN, A., PEREZ-BERNA, A. J., MENENDEZ-CONEJERO, R., FLINT, S. J., SAN MARTIN, C. & DE PABLO, P. J. 2013. Monitoring dynamics of human adenovirus disassembly induced by mechanical fatigue. *Sci Rep,* 3**,** 1434.

PANJA, D. & MOLINEUX, I. J. 2010. Dynamics of bacteriophage genome ejection in vitro and in vivo. *Phys Biol,* 7**,** 045006.

PARISIEN, A., ALLAIN, B., ZHANG, J., MANDEVILLE, R. & LAN, C. Q. 2008. Novel alternatives to antibiotics: bacteriophages, bacterial cell wall hydrolases, and antimicrobial peptides. *J Appl Microbiol,* 104**,** 1-13.

PAUCHARD, L. & RICA, S. 1998. Contact and compression of elastic spherical shells: the physics of a 'ping-pong'ball. *Philosophical Magazine B,* 78**,** 225-233.

PERALTA, B., GIL-CARTON, D., CASTANO-DIEZ, D., BERTIN, A., BOULOGNE, C., OKSANEN, H. M., BAMFORD, D. H. & ABRESCIA, N. G. 2013. Mechanism of membranous tunnelling nanotube formation in viral genome delivery. *PLoS Biol,* 11**,** e1001667.

PUROHIT, P. K., INAMDAR, M. M., GRAYSON, P. D., SQUIRES, T. M., KONDEV, J. & PHILLIPS, R. 2005. Forces during bacteriophage DNA packaging and ejection. *Biophys J,* 88**,** 851-66.

PYNE, A., THOMPSON, R., LEUNG, C., ROY, D. & HOOGENBOOM, B. W. 2014. Single-molecule reconstruction of oligonucleotide secondary structure by atomic force microscopy. *Small,* 10**,** 3257-61.

QADIR, M. I. 2015. Review: phage therapy: a modern tool to control bacterial infections. *Pak J Pharm Sci,* 28**,** 265-70.

REDDY, V. S., NATCHIAR, S. K., STEWART, P. L. & NEMEROW, G. R. 2010. Crystal structure of human adenovirus at 3.5 Å resolution. *Science,* 329**,** 1071-1075.

REDDY, V. S. & NEMEROW, G. R. 2014. Structures and organization of adenovirus cement proteins provide insights into the role of capsid maturation in virus entry and infection. *Proc Natl Acad Sci U S A,* 111**,** 11715-20.

RHO, J. Y., ASHMAN, R. B. & TURNER, C. H. 1993. Young's modulus of trabecular and cortical bone material: ultrasonic and microtensile measurements. *J Biomech,* 26**,** 111-9.

ROOS, W. H., BRUINSMA, R. & WUITE, G. J. L. 2010. Physical virology. *Nature Physics,* 6**,** 733.

ROOS, W. H., GERTSMAN, I., MAY, E. R., BROOKS, C. L., 3RD, JOHNSON, J. E. & WUITE, G. J. 2012. Mechanics of bacteriophage maturation. *Proc Natl Acad Sci U S A,* 109**,** 2342-7.

ROOS, W. H., IVANOVSKA, I. L., EVILEVITCH, A. & WUITE, G. J. 2007. Viral capsids: mechanical characteristics, genome packaging and delivery mechanisms. *Cell Mol Life Sci,* 64**,** 1484-97.

ROOS, W. H., RADTKE, K., KNIESMEIJER, E., GEERTSEMA, H., SODEIK, B. & WUITE, G. J. 2009. Scaffold expulsion and genome packaging trigger stabilization of herpes simplex virus capsids. *Proc Natl Acad Sci U S A,* 106**,** 9673-8.

ROSSMANN, M. G. 2013. Structure of viruses: a short history. *Q Rev Biophys,* 46**,** 133-80.

ROY, A., YANG, J. & ZHANG, Y. 2012. COFACTOR: an accurate comparative algorithm for structure-based protein function annotation. *Nucleic Acids Res,* 40**,** W471-7.

SAE-UENG, U., LIU, T., CATALANO, C. E., HUFFMAN, J. B., HOMA, F. L. & EVILEVITCH, A. 2014. Major capsid reinforcement by a minor protein in herpesviruses and phage. *Nucleic Acids Res,* 42**,** 9096-107.

SAN MARTIN, C., HUISKONEN, J. T., BAMFORD, J. K., BUTCHER, S. J., FULLER, S. D., BAMFORD, D. H. & BURNETT, R. M. 2002. Minor proteins, mobile arms and membrane-capsid interactions in the bacteriophage PRD1 capsid. *Nat Struct Biol,* 9**,** 756-63.

SANTOS-PEREZ, I., OKSANEN, H. M., BAMFORD, D. H., GONI, F. M., REGUERA, D. & ABRESCIA, N. G. A. 2017. Membrane-assisted viral DNA ejection. *Biochim Biophys Acta,* 1861**,** 664-672.

SCHAAP, I. A., EGHIAIAN, F., DES GEORGES, A. & VEIGEL, C. 2012. Effect of envelope proteins on the mechanical properties of influenza virus. *J Biol Chem,* 287**,** 41078-88.

SCHERES, S. H. 2016. Processing of Structurally Heterogeneous Cryo-EM Data in RELION. *Methods Enzymol,* 579**,** 125-57.

SCHOLL, D. 2017. Phage Tail-Like Bacteriocins. *Annu Rev Virol,* 4**,** 453-467.

SHAIKH, T. R., GAO, H., BAXTER, W. T., ASTURIAS, F. J., BOISSET, N., LEITH, A. & FRANK, J. 2008. SPIDER image processing for single-particle reconstruction of biological macromolecules from electron micrographs. *Nat Protoc,* 3**,** 1941-74.

SINGH, P., GONZALEZ, M. J. & MANCHESTER, M. 2006. Viruses and their uses in nanotechnology. *Drug Development Research,* 67**,** 23-41.

SMITH, D. E., TANS, S. J., SMITH, S. B., GRIMES, S., ANDERSON, D. L. & BUSTAMANTE, C. 2001. The bacteriophage straight phi29 portal motor can package DNA against a large internal force. *Nature,* 413**,** 748-52.

STROMSTEN, N. J., BAMFORD, D. H. & BAMFORD, J. K. 2003. The unique vertex of bacterial virus PRD1 is connected to the viral internal membrane. *J Virol,* 77**,** 6314-21.

TANG, G., PENG, L., BALDWIN, P. R., MANN, D. S., JIANG, W., REES, I. & LUDTKE, S. J. 2007. EMAN2: an extensible image processing suite for electron microscopy. *J Struct Biol,* 157**,** 38-46.

TRACHTENBERG, S., GALKIN, V. E. & EGELMAN, E. H. 2005. Refining the structure of the Halobacterium salinarum flagellar filament using the iterative helical real space reconstruction method: insights into polymorphism. *J Mol Biol,* 346**,** 665-76.

WATERS, E. M., NEILL, D. R., KAMAN, B., SAHOTA, J. S., CLOKIE, M. R. J., WINSTANLEY, C. & KADIOGLU, A. 2017. Phage therapy is highly effective against chronic lung infections with Pseudomonas aeruginosa. *Thorax,* 72**,** 666-667.

WATSON, J. D. & CRICK, F. H. 1953. The structure of DNA. *Cold Spring Harb Symp Quant Biol,* 18**,** 123-31.

WEN, A. M., RAMBHIA, P. H., FRENCH, R. H. & STEINMETZ, N. F. 2013. Design rules for nanomedical engineering: from physical virology to the applications of virus-based materials in medicine. *Journal of Biological Physics,* 39**,** 301-325.

WINSTON, F., BOTSTEIN, D. & MILLER, J. H. 1979. Characterization of amber and ochre suppressors in Salmonella typhimurium. *J Bacteriol,* 137**,** 433-9.

WUITE, G. J., SMITH, S. B., YOUNG, M., KELLER, D. & BUSTAMANTE, C. 2000. Single-molecule studies of the effect of template tension on T7 DNA polymerase activity. *Nature,* 404**,** 103-6.

XU, L., BENSON, S. D., BUTCHER, S. J., BAMFORD, D. H. & BURNETT, R. M. 2003. The receptor binding protein P2 of PRD1, a virus targeting antibiotic-resistant bacteria, has a novel fold suggesting multiple functions. *Structure,* 11**,** 309-22.

YANG, J. & ZHANG, Y. 2015. I-TASSER server: new development for protein structure and function predictions. *Nucleic Acids Res,* 43**,** W174-81.

ZANDI, R., REGUERA, D., RUDNICK, J. & GELBART, W. M. 2003. What drives the translocation of stiff chains? *Proc Natl Acad Sci U S A,* 100**,** 8649-53.

ZHANG, Y. 2009. I-TASSER: fully automated protein structure prediction in CASP8. *Proteins,* 77 Suppl 9**,** 100-13.

ZHAO, Y., AN, L. & FANG, J. 2009. Buckling instability of lipid tubules with multibilayer walls under local radial indentation. *Phys Rev E Stat Nonlin Soft Matter Phys,* 80**,** 021911.

ZHAO, Y., GE, Z. & FANG, J. 2008. Elastic modulus of viral nanotubes. *Phys Rev E Stat Nonlin Soft Matter Phys,* 78**,** 031914.

Appendix

7. APPENDIX

7.1. ABBREVIATIONS

(ds) DNA: Double-stranded desoxyribonucleic acid, 2
ACN: Acetonitrile, 39
AFM: Atomic force microscopy, 2, 5, 7, 9, 15, 18, 20, 21, 22, 23, 24, 34, 37, 40, 41, 42, 45, 46, 53, 62, 64, 72, 73, 84, 85, 86, 89, 91, 96
AMP: Antimicrobial peptides, 64
APTES: 3-(2,2-aminoethylamino)-ethylaminopropyltrimethoxysilane, 40, 72, 74
BCWH: bacterial cell wall hydrolases, 64
CCMV: Cowpea chlorotic mottle virus, 24
cryo-EM: cryo-electron microscopy, 2, 7, 15, 18, 26, 27, 30, 31, 35, 62, 64, 65, 74, 84, 103
CTF: Contrast transfer function , 28, 70
DM-AFM: Dynamic mode AFM, 22
DNA: desoxyribonucleic acid, 2, 5, 7, 12, 13, 15, 17, 19, 23, 25, 34, 35, 42, 46, 48, 53, 56, 58, 61, 62, 63, 74, 94, 100, 101, 102, 103, 104, 105, 106
FD-AFM: Force-distance AFM, 22
GON: Group of nine, 34, 35, 55
HIV: Human immunodeficiency virus, 24, 25
HR: High resolution, 15
HS-AFM: High-speed AFM, 22
HSV: Herpes simplex virus, 24, 57, 58, 103
LB: Luria broth, 37
LC-MS/MS: Liquid chromatography coupled to mass spectrometry, 39
MCP: Major capsid protein, 17, 57
MF-AFM: Multifrequency AFM, 22
MP-AFM: Multiparametric AFM, 22
MR-AFM: Molecular recognition AFM, 22
MVM: Minute virus of mice, 23
Opto-AFM: Advance optical imaging AFM, 23
RNA: Ribonucleic acid, 34, 58
SDS: Sodium dodecyl sulfate, 37, 38
TFA: trifluoroacetic acid, 39
TMV: Tomato mosaic virus, 3, 23, 89

7.2. ARTICLES PUBLISHED IN THE DURATION OF THIS THESIS

7.2.1. Articles which are directly related with this thesis work

AZINAS, S., BANO, F., TORCA, I. BAMFORD, D.H., SCHWARTZ, G.A., ESNAOLA, J.A., OKSANEN, H.M., RICHTER, R.P. & ABRESCIA, N.G.A. 2018. PRD1 virion exhibits mechanics of a composite material for genome protection. *Nanoscale 10,* 7769-7779

7.2.2. Other articles

POLITAKOS, N., AZINAS, S. & MOYA, S.E., 2016. Responsive copolymer brushes of Poly [(2-(Methacryloyloxy) Ethyl) Trimethylammonium Chloride](PMETAC) and Poly (1H, 1H, 2H, 2H-Perfluorodecyl acrylate)(PPFDA) to modulate surface wetting properties. *Macromolecular Rapid Communications*, *37*(7), pp.662-667.

FLEDDERMANN, J., DIAMANTI, E., AZINAS, S., KOSUTIC, M., DAHNE, L., ESTRELA-LOPIS, I., AMACKER, M., DONATH, E. & MOYA, S.E., 2016. Virosome engineering of colloidal particles and surfaces: bioinspired fusion to supported lipid layers. Nanoscale, 8(15), pp.7933-7941.

SPRINGALL, L., HUGHES, C.D., SIMONS, M., AZINAS, S., VAN HOUTEN, B. & KAD, N.M., 2017. Recruitment of UvrBC complexes to UV-induced damage in the absence of UvrA increases cell survival. Nucleic acids research.